Homogeneous Nucleation Theory

Thesis by

Richard B. McClurg

In Partial Fulfillment of the Requirements

for the Degree of

Doctor of Philosophy

California Institute of Technology

Pasadena, California

1997

(Submitted December 17, 1996)

Acknowledgements

My advisors, Professor Richard C. Flagan and Professor William A. Goddard, have provided both helpful advise when asked for their input and adequate freedom to pursue promising leads without interference. I am deeply appreciative of that management style, particularly since it does not lend itself to the typical three-year grant cycle. Undoubtedly, partial funding through an NSF fellowship helped make this arrangement possible. I also wish to thank Michael Vicic, Philip Watts, and Ruben Krasnopolsky who have served as sounding boards for various parts of this work. Finally, I am thankful for the support of my friends, parents, fiancée, and future in-laws who have aided me in more ways than they know.

S.D.G.

Richard McClurg

Pasadena, California

Abstract

This thesis is composed of a brief preface followed by six chapters addressing various aspects of homogeneous nucleation theory. In the preface, I motivate the need for improved theoretical approaches to resolve the discrepancies between current theory and experiment. The remaining chapters are collected research papers which are in print, in press, or to be submitted as of the writing of the thesis. They were written in collaboration with one or both of my advisors. In Chapter 2, we review current nucleation theories in a statistical mechanical framework. This framework allows us to identify the errors of the various models and to point out internal inconsistencies in some of them. In Chapters 3 and 4, we develop methods to calculate the partition function and thermodynamic properties for noble gas clusters. The methods allow us to describe the asymptotic approach of cluster properties toward the bulk limit with increasing cluster size and to calculate the nucleation rate for supersaturated noble gas vapors. We then apply the methods to the homogeneous nucleation of condensed mercury from a supersaturated vapor in Chapter 5. Chapters 6 and 7 contain portions of the theoretical groundwork needed to extend atomistic nucleation theories to molecular systems. Chapter 6 is a development of a one-dimensional hindered rotor partition function. It sets the stage for the two and three-dimensional hindered rotor partition functions needed to model molecular solids. In Chapter 7 we construct a model for the charge distribution of C_{60}. We chose this icosahedral molecule as an ideal plastic crystalline substances. The plastic crystals are solids with translational symmetry, but having weak orientational symmetry due largely to their highly symmetric molecular charge distributions. Thus, plastic crystals are ideal hindered rotors in multiple dimensions. I conclude the thesis with some brief comments on my assertion that molecules which form plastic crystals will provide a fruitful common ground for theoretical and experimental investigations of homogeneous nucleation phenomena.

Contents

List of Figures

Chapter 5

Chapter 6

Chapter 7

Appendix A

Appendix B

List of Tables

Appendix A

Appendix B

Chapter 1 Preface

1.1 Definitions

Homogenous nucleation refers to the spontaneous creation of a new phase from a metastable phase. The phase change can be from the vapor to a condensed phase (condensation), from a condensed phase to the vapor (cavitation), or from a solution phase to a solid phase (crystallization), for example. The main restrictions are:

1. The parent phase should be metastable. This requires that fluctuations of the order of several kT are required to nucleate the new phase. If this requirement is not met, then the theory of spinodal decomposition may be more appropriate.[1]

2. The creation of the new phase should be unassisted. Phase changes which occur due to impurities and/or surfaces are called heterogeneous nucleation events.[2]

The nucleation rate is the number of events in which a new phase is formed per unit volume and time. It is denoted J.

1.2 Context

The first theory of homogeneous nucleation is attributed to Gibbs and dates back to 1877.[3] His theory, which is discussed in the Introduction, explains qualitatively the nucleation process. It correctly predicts that the rate of nucleation vanishes at the equilibrium conditions and increases rapidly with increasing supersaturation for condensation or with increasing superheating for vaporization. This explanation was commonly accepted until the the first half of this century when a formalism was developed to calculate nucleation rates.[4–6] It was not until the 1950's however, when experimental measurements of nucleation rates showed that the theory and experiment often differ by many orders of magnitude.[7] The discrepancy between predicted and measured nucleation rates motivated quite a bit of theoretical effort aimed at predicting the properties of clusters of a few to a few tens of atoms or molecules.

Today, the situation is not significantly different. The major stumbling block to progress is that the systems chosen by experimentalists and theorists are quite different. For ease of handling and construction of experimental apparatus, experiments

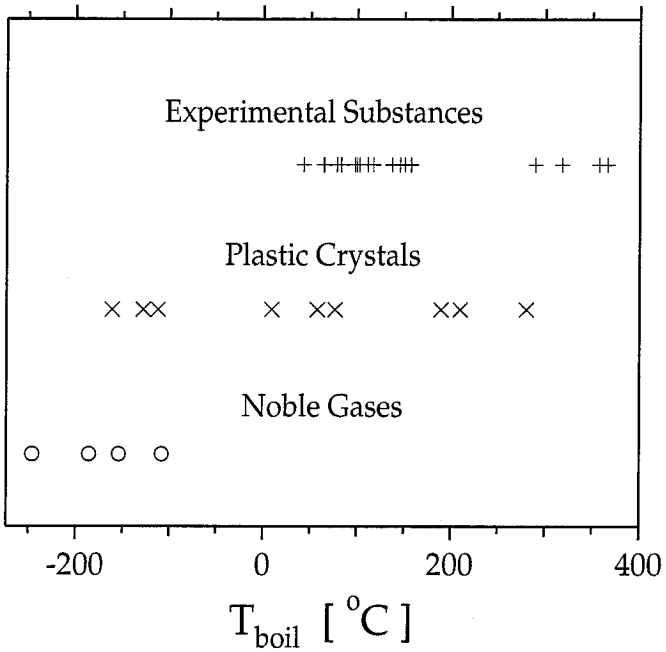

FIGURE 1 Normal boiling point of substances whose homogeneous nucleation rates have been studied by experimentalists and theorists. The two sets do not overlap because the criteria used by each group to select systems are very different. Also shown are normal boiling points for several plastic crystalline substances which may bridge this gap.

are generally performed on liquid substances with boiling points between room temperature and a few hundred degrees Celcius. This is illustrated in Fig. 1 where the normal boiling point of the substances listed in a recent review of nucleation experiments are plotted.[8,9] Also shown are the normal boiling points of several noble gases, which have been the systems of choice for theorists. Each of the various atomistic or molecular approaches to nucleation calculations are ultimately offshoots of the statistical-mechanical theory of polyatomic gases. The methods, which are discussed briefly in the Introduction, are essentially integrations over $3n$ positions and $3n$ momenta to produce a partition function. Here, n is the number of atoms in the nucleus (cluster, bubble, etc.) as it grows. Obviously, this is easiest when the nucleus is made up of hard atoms which interact only weakly and most difficult when the nucleus is made up of irregularly shaped, soft molecules. This is why the noble gases have been the system of choice for theorists.

1.3 Scope

If progress is to be made in resolving the discrepancies between theory and experiment in homogeneous nucleation, then some substances that are accessible to the experimentalists and tractable for the theorists need to be explored. In this thesis, I lay part of the groundwork for the predictions of nucleation rates for condensation of molecules from the vapor. My hypothesis is that the plastic crystals will be the common ground. Plastic crystals are molecular solids with translational order, but with no orientational order.[10] There is a range of temperatures, below the melting temperature but above a lower limit, in which the molecules pack as if they were spinning and/or tumbling rapidly but the center of mass librates about an equilibrium position within the crystal. By considering rapidly tumbling molecules, the theorist can maintain much of the advantage of working with spheres. Even if perturbations to the sphere are necessary, this is to be preferred over irregularly shaped or flexible molecules. By working with molecules rather than noble gases, it is also possible to find systems with reasonable properties. See Fig. 1. Plastic crystals are admittedly very special molecules and much of the practical interest in this field involves "messier" systems, but they hold the promise of shedding light on the process.

1.4 Outline

Each of the chapters of this thesis is designed to stand alone. Indeed, several have already been published and/or submitted for publication. It is my hope that the small amount of duplication that this requires will be warranted by the improved ease of reading.

Chapter 2 reviews nucleation theory and the various models of growing clusters.

Chapter 3 develops methods to extrapolate the various contributions to the free energy of a cluster toward the bulk limit. For simplicity, this chapter is limited to atomic (as opposed to molecular) clusters at temperatures below the surface melting temperature. This is the first of several chapters which makes reference to icosahe-

drons and/or icosahedral symmetry. Appendix A gathers together information about the icosahedron and its relationship to a cube which serves as background to these chapters. The FORTRAN code used to construct the structures used in this chapter is reproduced in Appendix C. This chapter has appeared in print as J. Chem. Phys. **102**, 3322 (1995).

Chapter 4 extends Chapter 3 to temperatures above the surface melting temperature. This chapter makes use of the information in Appendices A, B, and C. It has appeared in print as J. Chem. Phys. **105**, 7648 (1996). The FORTRAN code used in this work is too lengthy to include in an Appendix to this thesis. Instead, both Professor Richard C. Flagan and I maintain copies on CD ROM disks.

Chapter 5 is an application of Chapters 3 and 4 to the calculation of nucleation rates for supersaturated mercury vapor. As of the writing of this thesis, it is currently in press in NanoStructured Materials.

Chapter 6 develops a method for computing the partition function and thermodynamic functions for hindered rotors in one dimension. This is useful in its own right as a tool for computing the properties of molecules with hindered torsions, such as ethane. It is included in this thesis because it is the starting point for discussing hindered rotors in two and three dimensions. Plastic crystals in their orientationally disordered phase are multidimensional hindered rotors. This chapter has been submitted to J. Chem. Phys.

Chapter 7 develops a model for calculating the multipole moments for C_{60}. This molecule is a plastic crystal. Its icosahedral symmetry makes it particularly attractive for theorists. The multipole moments of C_{60} are largely responsible for the hindering potential for three-dimensional rotation. Estimating this potential is, in turn, the first step in calculating the librational partition function and thermodynamic functions. This chapter makes extensive use of Appendix A. It is to be submitted for publication.

1.5 References

[1]J. W. Cahn, Trans. Metall. Soc. AIME **242**, 166 (1968).

[2]J. H. Seinfeld, *Air Pollution* (Wiley, New York, 1986), p 343.

[3]*The Scientific Papers of J. Willard Gibbs* (Dover, New York, 1961), p 105.

[4]M. Volmer and A. Weber, Z. Phys. Chem. (Leipzig) **199**, 277 (1926).

[5]R. Becker and W. Doring, Ann. Phys. **24**, 719 (1935).

[6]J. Zeldovich, J. Exp. Theor. Phys. **12**, 525 (1942).

[7]G. M. Pound, J. Phys. Chem. Ref. Data **1**, 119 (1972).

[8]R. H. Heist and H. He, J. Phys. Chem. Ref. Data **23**, 781 (1994).

[9]R. H. Perry and D. W. Green (eds.) *Perry's Chemical Engineer's Handbook, 6th ed.* (McGraw-Hill, New York, 1984), Chpt. 3, pp 6-44.

[10]J. N. Sherwood, (ed.) *The Plastically Crystalline State* (Wiley-Interscience, New York, 1979).

Chapter 2 Introduction

Comment on Droplet Models in Homogeneous Nucleation Theory

Richard B. McClurg and Richard C. Flagan

Spalding Laboratory (210-41)
Division of Chemistry and Chemical Engineering
California Institute of Technology, Pasadena, California 91125

Abstract

We review the droplet models commonly used in calculations of the rate of homogeneous nucleation from the vapor. A statistical mechanical framework is used to form a common basis for comparison of the models. The asymptotic models (Capillarity, Tolman, and higher order models) and the semiphenomenological models introduced by Dillman and Meier are shown to be consistent with the statistical mechanical approach. The Lothe/Pound formalism over counts the degrees of freedom for a cluster and is therefore inconsistent. The Self Consistency Correction is shown to be an arbitrary method to handle a truncation error.

To be submitted for publication.

2.1 Introduction

There are currently a wide variety of droplet models used to calculate homogeneous nucleation rates.[1–5] This paper compares these models in the framework of the statistical mechanics of an ideal gas mixture of polyatomic gases. The common comparison reveals the assumptions behind each model and suggests that some have a more solid physical basis than others.

The outline of the balance of this paper is as follows. In Sec. 2.2, we briefly review classical nucleation theory to motivate Sec. 2.3 in which we compute the partition function of a cluster as an asymptotic series in the cluster size, n. This series is the common framework for comparing the various classes of cluster models in Secs. 2.4, 2.5, and 2.6. Finally, we draw several conclusions in Sec. 2.7.

2.2 Classical Nucleation Theory

According to classical theory,[6,7] homogeneous nucleation is a Markov process. Clusters grow by addition of single monomers or evaporate by elimination of single monomers. Under this assumption, the flux (J_n) of clusters through a size (n) is

$$J_n = \alpha_n \beta A_n C_n - E_{n+1} C_{n+1} \tag{1}$$

where α_n is the accommodation coefficient (commonly assumed to be unity), β is the flux of monomers through a unit area, A_n is the surface area of the cluster, C_n is the number concentration, and E_n is the frequency of monomer evaporation from an n-mer. To determine E_n, we follow the approach of Katz.[7] Applying detailed balancing at full thermodynamic equilibrium yields

$$J_n^{eq} = 0 = \alpha_n \beta^{eq} A_n C_n^{eq} - E_{n+1}^{eq} C_{n+1}^{eq}. \tag{2}$$

Assuming that the evaporation rate is independent of the saturation ratio, i.e. $E_{n+1} = E_{n+1}^{eq}$, leads to the following estimate for E_{n+1}:

$$E_{n+1} = \alpha_n \beta^{eq} A_n C_n^{eq} / C_{n+1}^{eq}. \tag{3}$$

Substituting Eq. (3) into Eq. (1),

$$J_n = \alpha_n \beta A_n C_n^{eq} \left[\frac{C_n}{C_n^{eq}} - \frac{\beta^{eq} C_{n+1}}{\beta C_{n+1}^{eq}} \right] \tag{4}$$

multiplying and dividing by $(\beta^{eq}/\beta)^n$, and rearranging gives

$$\frac{J_n}{\alpha_n \beta A_n C_n^{eq} (\beta/\beta^{eq})^n} = \frac{C_n}{C_n^{eq}} \left(\frac{\beta^{eq}}{\beta} \right)^n - \frac{C_{n+1}}{C_{n+1}^{eq}} \left(\frac{\beta^{eq}}{\beta} \right)^{n+1}. \tag{5}$$

For steady state nucleation, $J_1 = J_2 = ... = J_b = J$. Summing Eq. (5) over n yields

$$J \sum_{n=1}^{b} \frac{1}{\alpha_n \beta A_n C_n^{eq} (\beta/\beta^{eq})^n} = \frac{C_1}{C_1^{eq}} \left(\frac{\beta^{eq}}{\beta} \right) - \frac{C_{b+1}}{C_{b+1}^{eq}} \left(\frac{\beta^{eq}}{\beta} \right)^{b+1}. \tag{6}$$

From the kinetic theory of gases,

$$\beta = P/(2\pi m k T)^{1/2} \tag{7}$$

$$\beta/\beta^{eq} = P/P^{vap} = C_1/C_1^{eq} = S \tag{8}$$

where P is the monomer pressure and S is the saturation ratio. Finally, using Eqs. (8) and allowing b to become large gives the desired form for the nucleation rate,

$$J = \beta / \sum_{n=1}^{\infty} [\alpha_n A_n C_n^{eq} S^n]^{-1}. \tag{9}$$

Equation (9) differs by a factor of $1/S$ from the original expression developed by Volmer and Weber,[8] Becker and Doring,[9] and Zeldovich.[10] The $1/S$ factor was originally proposed by Courtney.[11] It is now commonly accepted that Eq. (9) is the correct form.[7] The various formalisms for calculating the homogeneous nucleation rate (J)

share Eq. (9) but differ in their methods for estimating the equilibrium cluster distribution (C_n^{eq}).

2.3 Statistical Mechanics

One rigorous way to determine the equilibrium cluster distribution (C_n^{eq}) is through statistical mechanics. We begin with the partition function for an ideal gas mixture. The canonical partition function for an ideal gas mixture of clusters is[12]

$$Q_{mix} = \prod_{n=1}^{\infty} q_n^{i_n}/(i_n)! \tag{10}$$

where q_n is the partition function for an n-mer and i_n is the number of n-mers in the mixture. This leads directly to the chemical potential for each component.

$$\mu_n = -kT\left(\frac{\partial \ln(Q_{mix})}{\partial i_n}\right)_{T,V,i_{\alpha\neq n}} = -kT\ln(q_n/i_n) \tag{11}$$

Thus, at full thermodynamic equilibrium ($n\mu = \mu_n$), the ratio of equilibrium cluster concentrations can be written as

$$\frac{C_n^{eq}}{C_1^{eq}} = \frac{i_n}{i_1} = \frac{(q_n/i_1)}{(q_1/i_1)^n}. \tag{12}$$

This is the law of mass-action. In its more familiar form, the cluster concentrations are related through a free energy of formation (ΔG).

$$\frac{C_n^{eq}}{C_1^{eq}} = \exp(-\Delta G/kT) \tag{13}$$

$$\Delta G = nkT\ln\left(\frac{q_1}{i_1}\right) - kT\ln\left(\frac{q_n}{i_1}\right) = -n\mu + G_n \tag{14}$$

Note that the free energy of formation of a cluster of size one from one monomer is precisely zero. This is the self-consistency requirement as defined by Girshick and Chiu.[5]

Molecular Dynamics (MD) and Monte Carlo (MC) simulations can be used to calculate the free energy of clusters (G_n).[6] The computational cost of creating a table of free energy versus n and T makes this approach impractical for routine use, however. Density functional methods have also been used.[6] Although these methods are less computationally intensive, it is not clear if the assumed monotonic density profile is appropriate for clusters of a few atoms or molecules, particularly below the melting temperature. The balance of this report is dedicated to another approach, droplet models, in which one uses properties of the vapor and/or bulk liquid to estimate cluster free energies (G_n). We motivate the functional form for those models using the statistical mechanics of an ideal polyatomic gas.

The partition function for a cluster of n monomers (q_n) can be separated into terms for translation (q_{tr}), rotation (q_{rot}), libration of monomers about their equilibrium positions (q_{lib}), vibration within the monomers (q_{vib}), degeneracy (d_j), and the Boltzmann factor.

$$q_n = \sum_j d_j q_{tr} q_{rot} q_{lib} q_{vib} \exp\left(-E_j/RT\right) \tag{15}$$

The degeneracy and Boltzmann factor account for the contributions from multiple isomers[13,14] that are important above the melting temperature of the cluster. In writing Eq. (15), we have assumed that the cluster rotation, monomer libration, and internal vibrations are decoupled. This is justified since the characteristic frequencies for these modes are very different. (The frequencies are roughly 0.1 cm^{-1}, 10 cm^{-1}, and 10^3 cm^{-1}, respectively.) For an ideal polyatomic gas, the translational degrees of freedom (q_{tr}) factor out exactly. This is a direct consequence of conservation of momentum. Some methods (i.e. MC simulation) are easier to perform if the center of mass is allowed to fluctuate,[15] but such fluctuations can lead to modifications to the nucleation rate expression,[16] Eq. (9). These issues are due to unphysical fluctuations in the simulation method and are not fundamental to nucleation theory, however.

Assuming that the cluster rotates rigidly and vibrates harmonically, the partition

function becomes

$$q_n = \sum_j d_j \left\{ V \left(\frac{2\pi nmkT}{h^2} \right)^{3/2} \right\} \left\{ \left(\frac{\pi^{1/2}}{\sigma_j} \right) \left(\frac{8\pi^2 kT}{h^2} \right)^{3/2} (I_A I_B I_C)^{1/2} \right\} \times \left\{ \prod_{i=1}^{i_{max}} \frac{\exp\left(\frac{-h\nu_i}{2kT}\right)}{1 - \exp\left(\frac{-h\nu_i}{kT}\right)} \right\} \exp\left(-E_j/RT\right) \tag{16}$$

where m is the mass of each particle, σ is the rotation symmetry number, $\{I_A, I_B, I_C\}$ are the principal moments of inertia, V is the volume per cluster, k is the Boltzmann constant, R is the gas constant, and h is Planck's constant. We assume that various isomers differ mainly in their degeneracies, binding energies, and symmetry numbers. This is reasonable since the cluster mass (nm) for each isomer is conserved and the product of the principal moments of inertia ($I_A I_B I_C$) is nearly constant for these roughly spherical isomers. This assumption will be bourn out by what follows. We further assume that the vibrational frequency distribution $\{\nu_i\}$ is barely changed by the small number of defects defining the differences between isomers.[17] In particular, we have assumed that the internal vibrations (q_{vib}) are unchanged by the condensation process and they will be ignored hereafter. This is equivalent to treating the molecules as rigid bodies. The limits on i are 1 to $3n - 6$ for atomic condensation and 1 to $6n - 6$ for molecular condensation. Also, Eq. (16) assumes fixed volume, restricting these results to the low pressure limit.

To simplify Eq. (16), we introduce the Einstein temperature (Θ_E)

$$\Theta_E = \left(\prod_{i=1}^{i_{max}} h\nu_i/k \right)^{1/i_{max}} \tag{17}$$

and the average zero-point energy per mode

$$E^{zp} = \sum_{i=1}^{i_{max}} \frac{h\nu_i}{2} / i_{max}. \tag{18}$$

TABLE I Material Property Scalings

Property		p	Expansion
Mass	M	1	mn
Moments of Inertia	$I_A I_B I_C$	5/3	$\sum_i \alpha_i n^{(5-i)/3}$
Minimum Potential Energy	E^{min}	1	$\sum_i \alpha_i n^{(3-i)/3}$
Zero Point Energy	E^{zp}	1	$\sum_i \alpha_i n^{(3-i)/3}$
Einstein Temperature	Θ_E	1	$\sum_i \alpha_i n^{-i/3}$

Then, from Eqs. (14) and (16), the free energy can be written as

$$\begin{aligned} G_n = E^{min} + i_{max}E^{zp} &- RT \ln\left\{V\left(\frac{2\pi nmkT}{h^2}\right)^{3/2}\right\} \\ &- RT \ln\left\{\pi^{1/2}\left(\frac{8\pi^2 kT}{h^2}\right)^{3/2}(I_A I_B I_C)^{1/2}\right\} \\ &- RT i_{max} \ln\left\{\frac{1}{1-\exp\left(\frac{-h\nu_i}{kT}\right)}\right\} \\ &- RT \ln\left\{\sum_j \left(\frac{d_j}{\sigma_j}\right)\exp\left(-\frac{E_j - E^{min}}{RT}\right)\right\} \end{aligned} \tag{19}$$

where E^{min} denotes the global minimum potential energy of the cluster. Thus, Eq. (19) shows that the free energy is a sum of contributions from the binding energy, zero-point energy, translation, rotation, vibration, and multiple configurations.

In order to express the free energy as a function of cluster size (n), we first express the material properties in Eq. (19) as a Taylor series in $n^{1/3}$

$$Y/n^p = \sum_{i=0}^{\infty} \alpha_i / n^{i/3}. \tag{20}$$

Here, Y stands for any of the material properties in Eq. (19) and α_i is an expansion coefficient. The 1/3 power is expected for three-dimensional clusters. The highest powers (p) for each property (Y) are determined by scaling analysis.[18] See Table I.

Gathering terms of the same order in n yields

$$G_n = \alpha_1 n + \alpha_2 n^{2/3} + \alpha_3 n^{1/3} + \alpha_4 \ln(n) + \sum_{i=5}^{\infty} \alpha_i n^{(5-i)/3}. \quad (21)$$

It has previously been recognized that many droplet models are of the form of the first five terms in Eq. (21),[19] but we believe this is the first derivation of the infinite expansion. The α_1 term has contributions from $3n$ vibrational degrees of freedom for atoms or $6n$ degrees of freedom for molecules. The proper values ($i_{max} = 3n - 6$ for atoms or $6n - 6$ for molecules) is recovered by the α_5 term. Translations and rotations of the cluster as a whole lead to contributions to the α_4 and α_5 terms. These assignments of the parentage of the various α's are important for understanding several of the cluster models discussed below.

2.4 Asymptotic Models

Capillarity Approximation

The oldest cluster model uses the capillarity approximation and is attributed to Gibbs.[1] He proposed that the free energy of a droplet is characterized by volume and surface terms,

$$G_n^{cap} = \mu n + \sigma A_n. \quad (22)$$

In Eq. (22), μ is the bulk chemical potential, σ is the surface free energy, and A_n is the surface area of an n-mer. Since the surface area scales as $n^{2/3}$, Eq. (22) is equivalent to using the first two terms of Eq. (21). For use in nucleation calculations, it is useful to introduce nomenclature that makes this scaling more transparent.[20] Using the following definition,

$$\Theta = A_1 \sigma / kT, \quad (23)$$

Eq. (22) becomes

$$G_n^{cap} = \mu n + kT\Theta n^{2/3}. \quad (24)$$

TABLE II Cluster Models

Model	$\alpha_1 n$	+	$\alpha_2 n^{2/3}$	+	$\alpha_3 n^{1/3}$	+	$\alpha_4 \ln(n)$	+	α_5
Capillarity	μn	+	$kT\Theta n^{2/3}$						
Tolman	μn	+	$kT\Theta n^{2/3}$	-	$kT\Theta B n^{1/3}$				
Lothe/Pound	μn	+	$kT\Theta n^{2/3}$	+	0	-	$4kT\ln(n)$		
SCC	μn	+	$kT\Theta n^{2/3}$	+	0	+	0	-	$kT\Theta$
Fisher	$f_\infty n$	+	$\sigma_\infty s_1 n^{2/3}$	+	$\alpha_1\sigma_\infty s_1 n^{1/3}$	+	$\tau kT\ln(n)$	+	$\alpha_2\sigma_\infty s_1$ $-kT\ln(\tilde{q}_o)$

Here, Θ is a non-dimensional surface tension which is not to be confused with the Einstein temperature (Θ_E), and A_1 is the apparent surface area of a monomer which is generally approximated using the bulk molar volume (v)

$$A_1 = (36\pi)^{1/3} v^{2/3}. \tag{25}$$

Tolman Correction

A paper by Tolman[2] was published posthumously in 1949 that extended Eq. (22) to include the first size corrections to the surface tension. He introduced what is now called the Tolman length (δ) which is the radial distance between the Gibbs surface of tension and the equimolar dividing surface. It leads to the following cluster model:

$$G_n^\delta = \mu n + \sigma A_n \left(1 - \frac{2\delta}{r} + \mathrm{O}(r^{-2})\right). \tag{26}$$

Once again, it is useful to introduce notation that makes the scaling more transparent.[21] Using Eq. (23) and the following definition,

$$B = \delta / r_1 = \left(\frac{4\pi}{3v}\right)^{1/3} \tag{27}$$

Eq. (26) becomes

$$G_n^{\delta} = \mu n + kT\Theta n^{2/3} - kT\Theta B n^{1/3}. \tag{28}$$

Therefore, Eq. (26) is equivalent to using the first three terms of Eq. (21). Several methods have been developed to estimate δ.[14,22–24] Equation (26) has been applied to homogeneous nucleation rate calculations.[21,25]

2.5 Semiphenomenological Droplet Models

Using an approach similar to Sec. 2.3, but different notation, Fisher[4] derived the following droplet model:

$$F_i^{Fisher} = if_{\infty} + \gamma s_1 i^{2/3} + \tau kT \ln i - kT \ln(\tilde{q}_o). \tag{29}$$

Except for obvious differences in notation, this is the same as the first, second, forth, and fifth terms in Eq. (21). The microscopic surface tension (γ) is an unspecified quantity in this model.

Dillmann and Meier[26] later extended the Fisher model by specifying a functional form for γ.

$$\gamma = \gamma_{\infty}\kappa_i \tag{30}$$

$$\kappa_i = 1 + \alpha_1 i^{-1/3} + \alpha_2 i^{-2/3} \tag{31}$$

Using this assumed functional form [Eq. (30)] in Fisher's model [Eq. (29)] yields a functional form equivalent to the first five terms in Eq. (21).

$$F_i^{DM} = if_{\infty} + \gamma_{\infty} s_1 i^{2/3} + \alpha_1 \sigma_{\infty} s_1 i^{1/3} + \tau kT \ln(i) + \alpha_2 \sigma_{\infty} s_1 - kT \ln(\tilde{q}_o) \tag{32}$$

DM determined α_1 and α_2 by comparing the power series for the vapor density as a function of vapor pressure implied by Eq. (32) with the virial equation of state. The predicted rates were in good agreement with experimental values for several

substances. Later, it was noted that the DM theory has an inconsistency in its treatment of the chemical potential.[27–29] The corrected version of the DM theory does not agree as well with experimental results. There is continued effort at finding new ways to determine the parameters in Eq. (32) which lead to better rate predictions.[30,31]

2.6 Other Models

Lothe and Pound Correction

Lothe and Pound[3] noted that the capillarity approximation [Eq. (22)] does not contain any explicit contributions from translation or rotation of the cluster. They noted that the highest order terms contributed by these degrees of freedom are $O(\ln n)$ and they simply added this term to the capillarity model.

$$G_n = \mu n + kT\Theta n^{2/3} - 4kT\ln(n) \tag{33}$$

This is equivalent to setting the third term of Eq. (21) equal to zero. Unfortunately, this term is needed to have the proper number of vibrational degrees of freedom ($3n-6$ for atoms or $6n-6$ for molecules). Neglecting it is equivalent to double counting six degrees of freedom and is, therefore, inconsistent.

Self-Consistent Cluster (SCC) Correction

Girshick and Chiu[5] noted that the capillarity approximation [Eq. (22)] leads to a non-zero free energy of formation for a cluster of one monomer. They proposed subtracting a constant to recover self-consistency.

$$G_n^{SCC} = G_n^{cap} - G_1^{cap} = \mu n + \sigma A_n - \sigma A_1 \tag{34}$$

Their model is equivalent to setting the coefficients of the $n^{1/3}$, the $\ln(n)$, and all of the $n^{-i/3}$ $(i > 0)$ terms to zero. We have already noted in discussing the Lothe and Pound Correction that the first of these is needed to ensure that the model contains

the proper number of degrees of freedom. The second neglected term contains the temperature dependent contributions of the translations and rotations. Setting this term to zero is equivalent to assuming that the mass and moment of inertia of the cluster are zero. Finally, this solution is not in keeping with the asymptotic nature of the capillarity approximation. As noted above, the capillarity approximation is simply the first two terms in an infinite series of terms for the cluster free energy. The self-consistency problem is simply a truncation error. Subtracting a constant from an asymptotic series to make the shifted series give a correct result at a particular size does not have any theoretical basis. If this *ad hoc* adjustment leads to improved predictions for nucleation rates for some systems, then this should be regarded as fortuitous.[6]

2.7 Conclusions

All of the cluster models reviewed in this paper can be viewed as special cases of the general expansion, Eq. (21). The capillarity model, Eq. (22); the Tolman model, Eq. (26); and the Dillman and Meier extension of the Fisher model, Eq. (32) are consistent with Eq. (21) in that they include lower order terms only after including all higher order terms. Therefore, these models can be expected to be asymptotically correct for large cluster size, n. The Lothe and Pound model, Eq. (33); and the SCC model, Eq. (34), include less significant terms before more significant terms and are therefore not asymptotically correct except for the infinite cluster ($n = \infty$). The empirical success of these two models should be regarded as fortuitous, especially since both overcount the number of vibrational degrees of freedom.

2.8 References

[1] *The Scientific Papers of J. Willard Gibbs* (Dover, New York, 1961), p 105.

[2] R. C. Tolman, J. Chem. Phys. **17**, 333 (1949).

[3]J. Lothe and G. M. Pound, J. Chem. Phys. **36**, 2080 (1962).

[4]M. E. Fisher, Physics **3**, 255 (1967).

[5]S. Girshick and C-P. Chiu, J. Chem. Phys. **93**, 1273 (1990).

[6]D. W. Oxtoby, J. Phys. Condens. Matter. **4**, 7627 (1992).

[7]J. L. Katz, Pure Appl. Chem. **64**, 1661 (1992).

[8]M. Volmer and A. Weber, Z. Phys. Chem. (Leipzig) **199**, 277 (1926).

[9]R. Becker and W. Doring, Ann. Phys. **24**, 719 (1935).

[10]J. Zeldovich, J. Exp. Theor. Phys. **12**, 525 (1942).

[11]W. G. Courtney, J. Chem. Phys. **35**, 2249 (1961).

[12]T. L. Hill, *Statistical Thermodynamics* (Dover, New York, 1986), pp104, 161-167.

[13]M. R. Hoare, Adv. Chem. Phys. **40**, 49 (1979), and references therein.

[14]R. B. McClurg, R. C. Flagan, and W. A. Goddard, J. Chem. Phys. **105**, 7648 (1996).

[15]H. Reiss, J. L. Katz, and E. R. Cohen, J. Chem. Phys. **48**, 5553 (1968).

[16]C. L. Weakliem and H. Reiss, J. Phys. Chem. **98**, 6408 (1994).

[17]F. H. Stillinger and T. A. Weber, J. Chem. Phys. **81**, 5095 (1984).

[18]R. B. McClurg, R. C. Flagan, and W. A. Goddard, J. Chem. Phys. **102**, 3322 (1995).

[19]C. S. Kiang, D. Stauffer, G. H. Walker, O. P. Puri, J. D. Wise, Jr., and E. M. Patterson, J. Atmos. Sci. **28**, 1222 (1971).

[20]D. R. Warren and J. H. Seinfeld, Aero. Sci. and Tech. **3**, 135 (1984).

[21]N. P. Rao and P. H. McMurry, Aero. Sci. and Tech. **13**,183 (1990).

[22]J. G. Kirkwood and F. P. Buff, J. Chem. Phys. **17**, 338 (1949).

[23]E. M. Blokhuis and D. Bedequx, J. Chem. Phys. **97**, 3576 (1992).

[24]W. K. Kegel, J. Chem. Phys. **102**, 1094 (1995).

[25]D. W. Heerman, J. Stat. Phys. **29**, 631 (1982).

[26]A. Dillmann and G. E. A. Meier, J. Chem. Phys. **94**, 3872 (1991).

[27]C. F. Delale and G. E. A. Meier, J. Chem. Phys. **98**, 9850 (1993).

[28]I. J. Ford, A. Laaksonen, and M. Kumala, J. Chem. Phys. **99**, 764 (1993).

[29]A. Laaksonen, I. J. Ford, and M. Kumala, Phys. Rev. E **49**, 5517 (1994).

[30]V. I. Kalikmanov and M. E. H. van Dongen, Phys. Rev. E **47**, 3532 (1993).

[31]V. I. Kalikmanov and M. E. H. van Dongen, J. Chem. Phys. **103**, 4250 (1995).

Chapter 3 Mackay Icosahedral Clusters

Free Energy and Surface Tension of Arbitrarily Large Mackay Icosahedral Clusters

Richard B. McClurg and Richard C. Flagan
Division of Chemistry and Chemical Engineering (CN 8723),
California Institute of Technology, Pasadena, California 91125

W. A. Goddard III[a)]
Division of Chemistry and Chemical Engineering (CN 8723), and
Materials and Molecular Simulation Center, Beckman Institute (139-74),
California Institute of Technology, Pasadena, California 91125

[a)]To whom correspondence should be addressed.

Abstract

We present a model for predicting the free energy of arbitrarily large Mackay icosahedral clusters. van der Waals clusters are experimentally observed to be particularly stable at magic numbers corresponding to these structures. Explicit calculations on the vibrational states were used to determine the spectrum of fundamental frequencies for smaller ($\leq$561) icosahedral clusters. The scaled cumulative frequency distribution function rapidly approaches a limiting function for large clusters. This function was used to predict zero-point energies and vibrational free energies for larger clusters (>561 atoms). Combining these predictions with correlations for the moment of inertia and for the minimum potential energy of large clusters leads to free energies of arbitrary large clusters. The free energies are used to predict the chemical potential and surface tension as a function of size and temperature. This connects macroscopic properties to the microscopic atomic parameters.

Reprinted with permission from Journal of Chemical Physics **102**, 3322 (1995).

3.1 Introduction

Mass spectroscopic studies on clusters of atoms (Ar, Kr, Xe) and molecules (CO, CH_4) have shown special stability at magic numbers 13, 55, 147, and 309 corresponding to Mackay icosahedral structures.[1] Extensive progress has been made in determining the minimum potential energy configuration of such clusters[2] and it has been shown[3] that Mackay clusters are the minimum potential energy structures for up to about 1600 atoms where decahedral structures become most stable. The bulk (fcc) structure becomes most stable for still larger clusters[3] ($n \approx 10^5$).

Herein we build on such results to predict the free energy of arbitrarily large Mackay icosahedra. This allows us to predict chemical potential $\mu(n)$ for arbitrarily large clusters. Since the slope of μ with respect to $x = n^{-1/3}$ gives the surface tension and the curvature of μ with respect to $x = n^{-1/3}$ gives the Tolman length, this provides a connection between the microscopic parameters (two-body interaction potentials) and macroscopic properties. The predicted values seem consistent with current experimental data. Although the Mackay clusters are not strictly the lowest energy for clusters larger than 1600 atoms, we believe that the resulting surface tension and Tolman length are accurate.

In Sec. 2 we develop procedures for predicting the free energy as a function of temperature for various Mackay clusters. Free energy calculations for van der Waals clusters have been presented by other authors. The most commonly used atomistic methods fall under two broad categories. Molecular dynamics and Monte Carlo methods confound the various degrees of freedom and hide their functional dependencies which makes extrapolations to larger sizes difficult. Freeman and Doll[4] have reviewed these methods, which will not be discussed further in this paper. In the normal-mode method, several approximations (enumerated below) are used to separate the degrees of freedom into translational, rotational, and vibrational contributions which (as we will show) can each be rationally extrapolated to arbitrarily large sized clusters. Hodgson[5] has summarized much of the previous work using the normal-mode calculation method. The cluster sizes considered previously were limited by the de-

termination of the $(3n-6)$ vibrational frequencies for a cluster containing n atoms. This requires diagonalizing the $3n$ by $3n$ Hessian matrix, which is unwieldy for large clusters. Thus, previous vibrational analyses of physical clusters were limited to Einstein models[6] or to clusters having fewer than 250 atoms.[5] From explicit calculations on up to 561 atoms, we show that the scaled cumulative frequency distributions for progressively larger clusters approach an asymptotic limit. This asymptotic limit permits the rational extrapolation of the vibrational free energy without calculation of the entire set of normal frequencies. The remaining contributions to the free energy will be addressed briefly.

In Sec. 3 these results are used to predict the surface energy and Tolman length for Ne, Ar, Kr, and Xe.

3.2 The Free Energy Function

Structures

The Mackay icosahedral structures[7] are constructed by surrounding a central atom with successively larger icosahedral shells. Each shell maintains icosahedral symmetry with the same orientation of its vertices. The first shell contains 12 atoms at the vertices of the icosahedron. The second shell contains 12 atoms at the vertices plus atoms on each of the 30 edges of the icosahedron for a total of 42 atoms in the second shell and a grand total of 55 atoms. Higher-order shells have additional atoms along the edges and in the faces of the icosahedral shell. In general, the number of atoms n in a Mackay structure with N shells is

$$n = 1 + \sum_{x=1}^{N} \left(10x^2 + 2\right) = \frac{1}{3}\left(10N^3 + 15N^2 + 11N + 3\right). \tag{1}$$

Thus, the first 8 Mackay icosahedral structures contain 13, 55, 147, 309, 561, 923, 1415, and 2057 atoms, respectively. Clusters containing these numbers of atoms are called magic numbered clusters.[8]

The Free Energy

The free energy for an ideal polyatomic gas

$$F = -RT \ln\left(\frac{q}{N_a}\right) \tag{2}$$

is calculated[9] from the single-cluster partition function, q, which can be separated into terms for translation (q_{tr}), rotation (q_{rot}), vibration (q_{vib}), degeneracy (d_j), and a Boltzmann weight.

$$q = \sum_j d_j q_{tr} q_{rot} q_{vib} \exp\left(\frac{-E_j}{RT}\right). \tag{3}$$

The degeneracy and Boltzmann weights account for contributions from multiple isomers and are important above the melting temperature of the cluster. They are not needed for the present study which focuses on the solidlike limit.

The partition function is evaluated assuming that the cluster has harmonic vibrations and rotates as a spherically symmetric rigid rotor. Thus

$$\begin{aligned} q = \sum_j \; d_j \; & \left\{ V \left(\frac{2\pi n m k T}{h^2}\right)^{3/2} \right\} \left\{ \left(\frac{\pi^{1/2}}{\sigma_j}\right) \left(\frac{8\pi^2 k T I}{h^2}\right)^{3/2} \right\} \\ \times \; & \left\{ \prod_{i=1}^{3n-6} \frac{\exp\left(\frac{-h\nu_i}{2kT}\right)}{1 - \exp\left(\frac{-h\nu_i}{kT}\right)} \right\} \exp\left(\frac{-E_j}{RT}\right), \end{aligned} \tag{4}$$

where m is the mass of each particle, σ is the rotation symmetry number, I is the moment of inertia, V is the volume, k is the Boltzmann constant, R is the gas constant, and h is Planck's constant. We assume that various isomers differ mainly in their degeneracies, binding energies, and symmetry numbers. We assume fixed volume in Eq. (4), thus these results pertain to the low pressure limit.

From Eqs. (2) and (4), the free energy can be written as

$$\begin{aligned} F = E^{min} + \sum_{i=1}^{3n-6} \frac{h\nu_i}{2} \; & - \; RT \ln\left\{ V \left(\frac{2\pi n m k T}{h^2}\right)^{3/2} \right\} \\ & - \; RT \ln\left\{ \pi^{1/2} \left(\frac{8\pi^2 k T I}{h^2}\right)^{3/2} \right\} \end{aligned}$$

$$- \quad RT \sum_{i=1}^{3n-6} \ln \left\{ \frac{1}{1 - \exp\left(\frac{-h\nu_i}{kT}\right)} \right\}$$

$$- \quad RT \ln \left\{ \sum_j \left(\frac{d_j}{\sigma_j}\right) \exp\left(-\frac{E_j - E^{min}}{RT}\right) \right\}, \qquad (5)$$

where E^{min} denotes the global minimum potential energy of the cluster.

The Cumulative Frequency Function

The interactions among atoms or molecules in the clusters are assumed to involve only two-body interactions. The explicit calculations use the Lennard-Jones potential

$$\epsilon = \rho^{-12} - 2\rho^{-6}, \qquad (6)$$

$$\epsilon = \frac{E}{D_e}, \qquad (7)$$

$$\rho = \frac{r}{R_e}, \qquad (8)$$

where r is the distance between the particles. (For molecular clusters multipole electrostatic interactions would also be included.) Energies, temperatures, and vibrational frequencies are nondimensionalized in order for the analysis to be most general. In addition to D_e and R_e, the atomic mass (m) is used to nondimensionalize the data, leading to a characteristic vibrational frequency of

$$\nu_{char} = \frac{1}{2\pi R_e}\sqrt{\frac{D_e}{m}}. \qquad (9)$$

Some typical Lennard-Jones parameters (R_e, D_e) are tabulated[10] in Table I.

Calculated fundamental vibrational modes and their frequencies are shown in Figure 1 for icosahedral clusters having 13, 55, 147, 309, and 561 atoms.[11,12] Figure 2 represents this data as the Cumulative Frequency Function, $G_N(\nu)$, for each cluster. The maximum frequency for the cluster (ν_{max}) was used to scale the frequency coordinate and the total number of vibrational modes ($3n - 6$) was used to scale

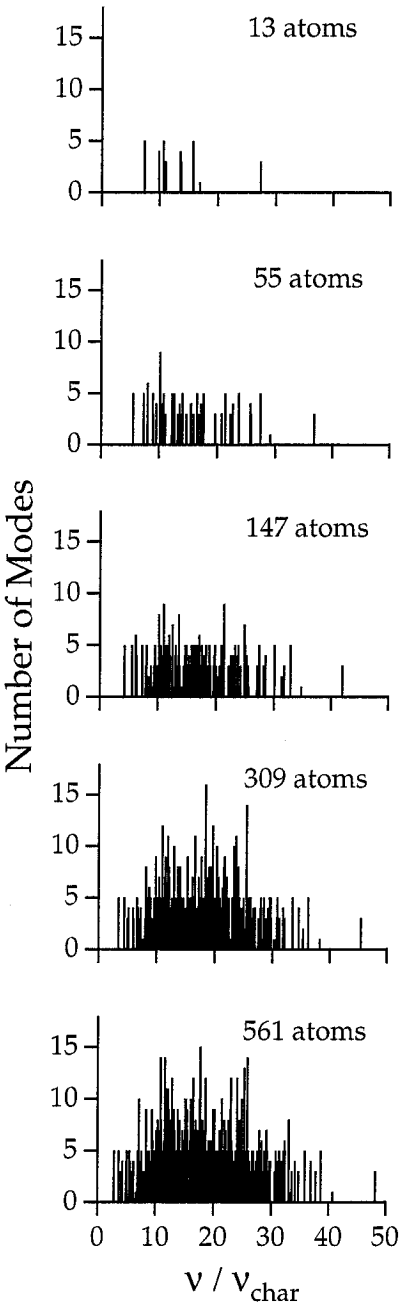

FIGURE 1 Histogram of vibrational frequencies for Mackay clusters of 13, 55, 147, 309 and 561 atoms. Frequencies are scaled by the characteristic value $\nu_{char} = \frac{1}{2\pi R_e}\sqrt{\frac{D_e}{m}}$. A boxwidth of 0.05 was used in constructing the histogram.

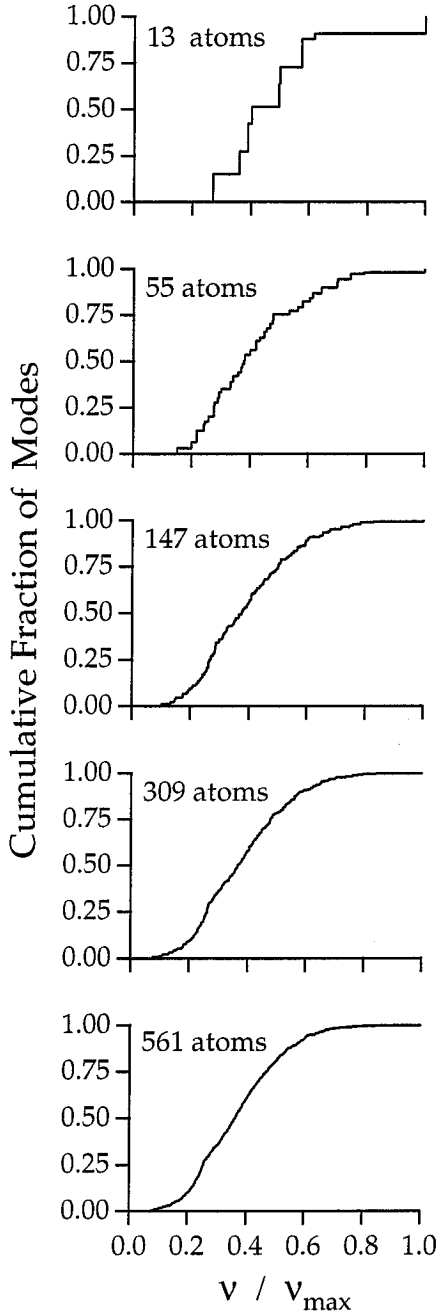

FIGURE 2 The cumulative frequency function $[G_N(\nu)]$ for Mackay icosahedral clusters of 13, 55, 147, 309, and 561 atoms. Frequencies are scaled by the largest frequency, ν_{max}, for each cluster. Comparison of $n = 147$, 309, and 561 indicates that an asymptotic limit is being reached.

TABLE I Parameters and characteristic quantities for sample systems.[10] There are two energy scales, D_e and ν_{char}. D_e determines the potential energy at the optimal structure while ν_{char} determines the zero-point energy and vibrational contributions.

Quantity	Units	Ne	Ar	Kr	Xe
m	amu	20.179	39.948	83.80	131.30
D_e	kcal/mol	0.0726	0.237	0.325	0.446
R_e	Å	3.249	3.867	4.109	4.465
$\nu_{char} = \frac{1}{2\pi R_e}\sqrt{\frac{D_e}{m}}$	GHz	60.12	64.86	49.35	42.50
	cm^{-1}	2.004	2.162	1.645	1.417
$E_{char} = h\nu_{char}$	cal/mol	5.729	6.181	4.704	4.051
$T_{char} = \frac{h\nu_{char}}{k}$	K	2.883	3.111	2.367	2.039
$I_{char} = mR_e^2$	amu $Å^2$	213.0	597.4	1415	2618

the cumulative modes coordinate. $G_N(\nu)$ appears to approach a smooth, continuous limiting function as $N \rightarrow \infty$.

This observed asymptotic approach to a limiting function for $G_N(\nu)$ is the basis for estimating properties of larger Mackay icosahedral structures. The zero-point energy and heat capacities approach limits as a direct result of $G_N(\nu)$ approaching a limit.

Rather than using $G_N(\nu)$ more typically the vibrational frequencies are expressed in terms of the frequency distribution function, $g_N(\nu)$, defined as the number of normal vibrational frequencies per unit frequency interval,

$$\int_0^\nu g_N(x)dx = G_N(\nu). \tag{10}$$

Topological considerations show that for infinite three-dimensional crystals, $g_N(\nu)$ is continuous but with discontinuous slopes (van Hove singularities) arising from long range translational symmetry (the Brillouin zone).[13] The frequency distributions for finite systems differs from the bulk and is sensitive to cluster geometry.[14]

Zero-Point Energy

The zero-point energy for a set of $3n-6$ harmonic oscillators is

$$E^{zp} = \frac{h}{2}\sum_{i=1}^{3n-6}\nu_i, \tag{11}$$

which can be written in terms of the frequency distribution function, $g(\nu)$,[9]

$$E^{zp} = \frac{h}{2}\int_o^{\nu_{max}} \nu g(\nu) d\nu, \tag{12}$$

where $g_N(\nu)$ is zero for $\nu > \nu_{max}$. We find that ν_{max} is dominated by the motion of the central atom of the cluster moving in the potential of the first (12 atom) shell. The change with N is caused by the compression of this first shell as N is increased. Scaling the frequencies by ν_{char} from (9) leads to

$$E^{zp} = \frac{h\nu_{char}}{2}\int_0^{\hat{\nu}_{max}} \hat{\nu} g_N(\hat{\nu}) d\hat{\nu}, \tag{13}$$

where

$$\hat{\nu} = \frac{\nu}{\nu_{char}}. \tag{14}$$

Further scaling $g_N(\nu)$ by the total number of frequencies leads to

$$E^{zp} = (3n-6)h\nu_{char}\int_0^{\hat{\nu}_{max}} \frac{1}{2}\hat{\nu}\hat{g}_N(\hat{\nu}) d\hat{\nu}, \tag{15}$$

where

$$\hat{g}_N = \frac{g_N}{(3n-6)}. \tag{16}$$

The integral in Eq. (15) is the dimensionless zero-point energy per mode, which we denote as

$$J_N = \frac{1}{2}\int_0^{\hat{\nu}_{max}} \hat{\nu}\hat{g}_N(\hat{\nu}) d\nu = \frac{E^{zp}}{(3n-6)h\nu_{char}}. \tag{17}$$

J_N can be calculated from Eq. (17) and the frequency information in Figure 1. Values for J_N are given in Table II.

TABLE II Calculated and extrapolated maximum frequencies (ν_{max}) and zero-point energies (E^{zp}) for Mackay icosahedral clusters. Frequencies are scaled by the characteristic value ν_{char}, Eq. (9). Zero-point energies are scaled by the characteristic value $E_{char} = h\nu_{char}$. The function J_N is defined in Eq. (17) and fitted by Eq. (18).

Shells	Atoms	Frequency		Zero Point Energy		
		$\frac{\nu_{max}}{\nu_{char}}$	$\frac{E^{zp}}{E_{char}}$	J_N	J_N	$\frac{E^{zp}}{E_{char}}$
(N)	(n)	Calc	Calc	Calc	Extrap	Extrap
1	13	27.3	217.5	6.591	6.591	217.5
2	55	36.8	1212	7.623	7.623	1212
3	147	42.0	3600	8.276	8.276	3600
4	309	45.4	7998	8.684	8.684	7998
5	561	48.1	15020	8.956	8.957	15020
6	923				9.151	25280
7	1415				9.296	39410
∞	∞				10.287	

Figure 3 shows that the dependence of J_N on the number of filled shells N is quite smooth and well described by the function

$$J_N = 10.287 - \frac{7.679}{N} + \frac{5.422}{N^2} - \frac{1.439}{N^3}. \tag{18}$$

A Laurent-type expansion is used for fitting throughout this work to avoid non-physical singularities in the extrapolations to larger clusters. In each case, the order of the fit was chosen to minimize the variance.

Vibrational Heat Capacity

The heat capacity can be written as the sum of contributions from translation, rotation, and vibration.

$$C_v = C_v^{tr} + C_v^{rot} + C_v^{vib}. \tag{19}$$

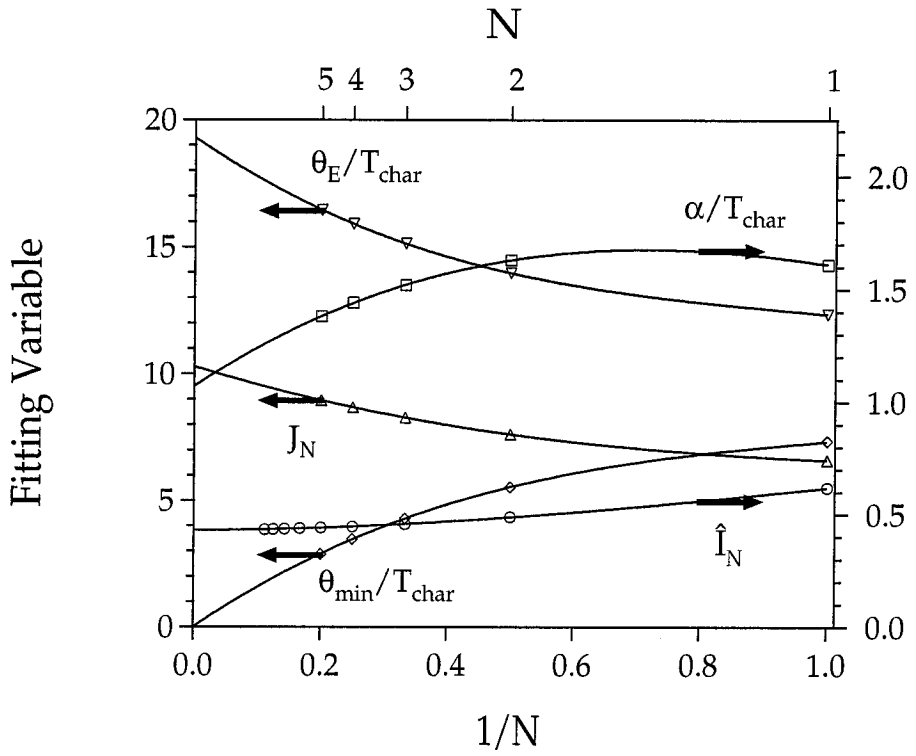

FIGURE 3 The five characteristic variables as a function of the number of shells (N) in a cluster: (a) the dimensionless zero-point energy per mode, J_N [see Eq. (17)]; (b) the softening temperature, α [see Eq. (29)]; (c) the characteristic Einstein temperature, θ_E [see Eq. (25)]; (d) the softest mode characteristic temperature, θ_{min} [see Eq. (27)]; and (e) the dimensionless incremental moment of inertia, $\hat{I}_N$ [see Eq. (35)]. All five quantities vary slowly with $1/N$, leading to accurate extrapolations. Zero-point energy is scaled by $E_{char} = \frac{h}{2\pi R_e}\sqrt{\frac{D_e}{m}}$. α, θ_E, and θ_{min} are scaled by a characteristic value $T_{char} = \frac{h\nu_{char}}{k}$. The moments are scaled by $I_{char} = mR_e^2$.

Except for very light clusters at very low temperatures, the translational and rotational contributions are fully classical, leading to

$$C_v = 3R + C_v^{vib} \tag{20}$$

(R is the ideal gas constant). We now focus on C_v^{vib}.

The vibrational contribution can be written in terms of a summation over the normal modes as follows:[9]

$$C_v^{vib} = R \sum_{i=1}^{3n-6} \frac{\left(\frac{h\nu_i}{kT}\right)^2 \exp\left(\frac{h\nu_i}{kT}\right)}{\left[\exp\left(\frac{h\nu_i}{kT}\right) - 1\right]^2}. \tag{21}$$

This leads to a temperature-dependent contribution to the free energy.[9]

$$F^{vib} = RT \sum_{i=1}^{3n-6} \ln\left[1 - \exp\left(-\frac{h\nu_i}{kT}\right)\right]. \tag{22}$$

We want to obtain a simple form for F^{vib} containing a small number of independent variables so that the free energy can be estimated without calculating all $(3n-6)$ frequencies.

In the high temperature limit, Eq. (22) can be written as:

$$\lim_{T\to\infty} F^{vib} = RT(3n-6)\ln\left[\prod_{i=1}^{3n-6}\left(\frac{h\nu_i}{kT}\right)^{\frac{1}{3n-6}}\right]. \tag{23}$$

This is the same limiting behavior as $(3n-6)$ oscillators having an Einstein frequency of

$$\nu_E = \left(\prod_{i=1}^{3n-6} \nu_i\right)^{\frac{1}{3n-6}} \tag{24}$$

or an Einstein temperature of

$$\theta_E = \frac{h}{k}\left(\prod_{i=1}^{3n-6} \nu_i\right)^{\frac{1}{3n-6}} \tag{25}$$

Consequently, we fit Eq. (22) with a function

$$F^{vib} = \xi RT(3n-6)\ln\left[1-\exp\left(-\frac{\theta_E}{T}\right)\right], \tag{26}$$

where the function $\xi(T)$ has the following characteristics:

$$\xi \sim 1 \text{ for T} \rightarrow \infty$$

$$\xi \sim \exp\left[\frac{\theta_E - \theta_{min}}{T}\right] \text{ for T} \rightarrow 0$$

$$\theta_{min} = \frac{h\nu_{min}}{k}. \tag{27}$$

This accounts for the presence of soft modes which "freeze out" at temperatures lower than θ_E. A Padé form consistent with the limiting behavior for ξ is

$$\xi = \exp\left[\left(\frac{\beta + \frac{\alpha(\theta_E-\theta_{min})}{T}}{1+\frac{\alpha}{T}}\right)\frac{1}{T}\right]. \tag{28}$$

We find that Eq. (28) with β set to zero is sufficient to accurately fit the full summation in Eq. (22),

$$\xi \approx \exp\left[\frac{\alpha\left(\theta_E - \theta_{min}\right)}{T\left(T+\alpha\right)}\right]. \tag{29}$$

The above analysis reduces the calculation of the vibrational free energy to determining three effective temperatures α, θ_E, and θ_{min}. Figure 3 shows that all three vary slowly with $1/N$, leading to accurate extrapolations

$$\frac{\alpha}{T_{char}} = 1.05 + \frac{1.97}{N} - \frac{1.88}{N^2} + \frac{0.47}{N^3}, \tag{30}$$

$$\frac{\theta_E}{T_{char}} = 19.27 - \frac{16.95}{N} + \frac{15.42}{N^2} - \frac{5.40}{N^3}, \tag{31}$$

$$\frac{\theta_{min}}{T_{char}} = 0 + \frac{17.16}{N} - \frac{14.49}{N^2} + \frac{4.67}{N^3}. \tag{32}$$

The parameters α, θ_E, and θ_{min} are listed in Table III for several values of N.

TABLE III Calculated and extrapolated parameters for fitting the vibrational partition function. Here θ_{min} corresponds to the minimum vibrational frequency, θ_E corresponds to the effective Einstein frequency, and α corresponds to the softening frequency. θ_E is defined in Eq. (25) and fitted with Eq. (31). α is defined in Eq. (29) and fitted by Eq. (30). θ_{min} is defined in Eq. (27) and fitted with Eq. (32).

Shells	Atoms	$\frac{\alpha}{T_{char}}$		$\frac{\theta_E}{T_{char}}$		$\frac{\theta_{min}}{T_{char}}$	
(N)	(n)	Fit	Extrap.	Calc.	Extrap.	Calc.	Extrap.
1	13	1.61	1.61	12.35	12.35	7.35	7.35
2	55	1.63	1.63	13.98	13.98	5.53	5.54
3	147	1.52	1.52	15.14	15.14	4.29	4.28
4	309	1.44	1.44	15.91	15.92	3.47	3.46
5	561	1.38	1.38	16.46	16.46	2.88	2.89
6	923		1.33		16.85		2.48
7	1415		1.30		17.15		2.17
∞	∞		1.05		19.27		0

Moment of Inertia

Due to the high symmetry of Mackay clusters, the moment of inertia tensor

$$I_{\alpha\beta} = \sum_{j=1}^{n} m_j \left(\delta_{\alpha\beta} R_j^2 - R_{\alpha j} R_{\beta j}\right) \tag{33}$$

is isotropic, $I_{\alpha\beta} = \delta_{\alpha\beta} I$. The scalar I can be decomposed into contributions from each shell using

$$I = \frac{2}{3} \sum_{y=1}^{N} \sum_{j=1}^{10y^2+2} m_j R_j^2. \tag{34}$$

The average distance R_j is written as $R_j = \rho_j y R_e$ where $\rho_j \approx 1$. Therefore, Eq. (34) becomes

$$\frac{I}{m R_e^2} = \frac{2}{3} \sum_{y=1}^{N} \left[y^2 \sum_{j=1}^{10y^2+2} \rho_j \right] = \sum_{y=1}^{N} y^2 \left(10y^2 + 2\right) \hat{I}_y, \tag{35}$$

where the function $\hat{I}_N$ is slowly varying and of order one.

The structures for N=1 through 9 (n = 13 to 2869 atoms) were minimized using POLYGRAF,[11] leading to the results in Table IV and Figure 3. The following fit to

TABLE IV Moments of inertia for Mackay icosahedral clusters. The moments are scaled by the characteristic value $I_{char} = mR_e^2$. $\hat{I}_N$ is the scaled incremental moment of inertia given by Eq. (35) and fitted by Eq. (36).

N	n	I/mR_e^2	$\hat{I}_N$
1	13	7.4319	0.6193
2	55	89.431	0.4881
3	147	468.76	0.4581
4	309	1626.6	0.4467
5	561	4406.2	0.4412
6	923	10115	0.4381
7	1415	20627	0.4360
8	2057	38489	0.4347
9	2869	67035	0.4340
∞	∞		0.4257

the data is used for extrapolating to larger clusters

$$\hat{I}_N = 0.4298 + \frac{0.0104}{N} + \frac{0.2457}{N^2} - \frac{0.0666}{N^3}. \tag{36}$$

Minimum Potential Energy

From explicit calculations on the optimum structures of icosahedral clusters for $N =$ 2 - 14 ($n = 55$ - 10179 atoms), Xie *et al.*[15] found that the minimum potential energies can be fitted to the function

$$-\epsilon_N^{min} = -\frac{E_N^{min}}{nD_e} = D + Cn^{-\frac{1}{3}} + Bn^{-\frac{2}{3}} + An^{-1}$$

$$(N > 1) \tag{37}$$

with an accuracy of $\pm 0.1 D_e$. The expansion coefficients are $A = 9.8248958$, $B =$ 1.5534957, $C = -14.217539$, and $D = 8.5326356$.

This data can be reexpressed by an expansion in the number of filled shells,

$$-\epsilon_N^{min} = -\frac{E_N^{min}}{nD_e} = \bar{D} + \bar{C}N^{-1} + \bar{B}N^{-2} + \bar{A}N^{-3}$$

$$(N > 1), \tag{38}$$

using $\bar{A} = -1.753665$, $\bar{B} = 6.295212$, $\bar{C} = -9.629845$, and $\bar{D} = 8.537573$. Equation (38) is more useful in the current context since it expresses the minimum potential energy as an expansion in the same independent variable as for the other functions.

For the single shell case ($n = 13$)

$$-\epsilon_1^{min} = 3.410. \tag{39}$$

Symmetry Numbers, Degeneracies, and Isomers

For icosahedral clusters, the rotational symmetry number (σ) is 60 and the degeneracy (d) is 1. Other isomers will tend to have symmetry numbers of order one, but higher degeneracies. Although these factors would tend to favor other isomers in the partition function, the Boltzmann weighting ensures that the icosahedral structure is dominant until the temperature is comparable[16] to 0.3 D_e/R. Above this temperature, the cluster surface melts and multiple inherent structures become significant. We consider this melting temperature as the upper limit for application of our model.

Summary

The correlations presented in Eqs. (18), (30)-(32), (36) and (38) can now be used to predict the free energies of arbitrarily large magic-numbered Mackay icosahedral clusters

$$\begin{aligned} F &= nD_e\epsilon_N^{min} + (3n-6)h\nu_{char}J_N \\ &- RT\ln\left\{V\left(\frac{2\pi nmkT}{h^2}\right)^{3/2}\right\} \\ &- RT\ln\left\{\pi^{1/2}\left(\frac{8\pi^2 kTmR_e{}^2}{h^2}\sum_{y=1}^{N} y^2\left(10y^2+2\right)\hat{I}_y\right)^{3/2}\right\} \end{aligned}$$

$$+ \quad RT(3n-6)\left\{\ln\left[1-\exp\left(-\frac{\theta_E}{T}\right)\right]\right\}\exp\left[\frac{\theta_E-\theta_{min}}{T\left(1+\frac{T}{\alpha}\right)}\right]$$

$$+ \quad RT\ln 60. \tag{40}$$

3.3 Discussion

The above derivation assumes that the atoms or molecules vibrate around some equilibrium position. That is, the clusters are solid-like. In addition the vibrational partition function was analyzed assuming all vibrational states are harmonic oscillators. The anharmonicity will influence the heat capacity, particularly at higher temperatures.

Above the melting temperature, multiple isomeric structures become significant. Calculations by Honeycutt and Andersen[16] on 13 and 55 atom clusters suggest that melting occurs at a temperature between $0.3D_e/R$ and $0.4D_e/R$. Thus, the vibrational contribution to the free energy in Eq. (26) is a low temperature approximation, with large deviations expected as the melting point is reached.

Our predictions for $N \to \infty$ are restricted to Mackay icosahedra. For sufficiently large N the most stable structure is the face centered cubic (fcc) crystalline form. Indeed for Lennard-Jones clusters, a decahedral structure becomes stable above 1600 atoms.[3] Even so, it is of interest to examine the properties predicted for infinite systems from these calculations because this allows a connection between macroscopic properties and microscopic parameters (R_e, D_e, m).

Bulk Properties - Classical Analysis

We will use several equations from macroscopic thermodynamics to relate cluster-free energies to bulk chemical potentials and surface tensions. The free energy of a macroscopic liquid drop (F) can be written in terms of the number of particles in the drop (n), the chemical potential of a particle in the bulk (μ), the surface area of the

drop (a), and the surface tension (σ)

$$F = n\mu + a\sigma. \tag{41}$$

Tolman showed[17] that the surface tension of a spherical drop is related to the radius of curvature (r) as in

$$\sigma(r) = \sigma_o(1 - \frac{2\delta}{r}) + 0(r^{-2}). \tag{42}$$

Although Eq. (42) is only the lowest-order correction, we will use the Tolman length (δ) as a fitting parameter down to the smallest Mackay clusters. For spherical drops, the surface area, radius of curvature, and number of particles are related through the molecular volume (v)

$$a = 4\pi r^2, \tag{43}$$

$$nv = \frac{4}{3}\pi r^3. \tag{44}$$

Using Eqs. (41) - (44), the free energy of the drop can be written as a power series in $n^{-1/3}$

$$\frac{F}{n} = \mu + \sigma_o(4\pi)^{1/3}(3v)^{2/3}n^{-1/3} - 2\sigma_o\delta(4\pi)^{2/3}(3v)^{1/3}n^{-2/3}. \tag{45}$$

Figure 4 shows a plot of the free energy per particle (F/n) for argon clusters versus $n^{-1/3}$ for three temperatures. Quadratic fits to the data yield estimates of three of the four material properties in Eq. (45). Assuming the bulk density of the solid[10] as the fourth parameter allows the bulk chemical potential, surface tension, and Tolman length to be calculated. The results of these calculations are in Table V. Figure 5 shows that the predicted surface energies at low temperature are in good qualitative agreement with published measurements for higher temperatures.[18,19] In addition, Figure 6 shows good agreement of the predicted Tolman lengths with the results of recent molecular dynamics simulations of a liquid/vapor interface for a Lennard-Jones fluid.[20] Such agreement lends support for using the extrapolations on Mackay icosahedral clusters even though they are not the lowest energy structures for clusters containing more than 1600 particles. The close relationship between Mackay

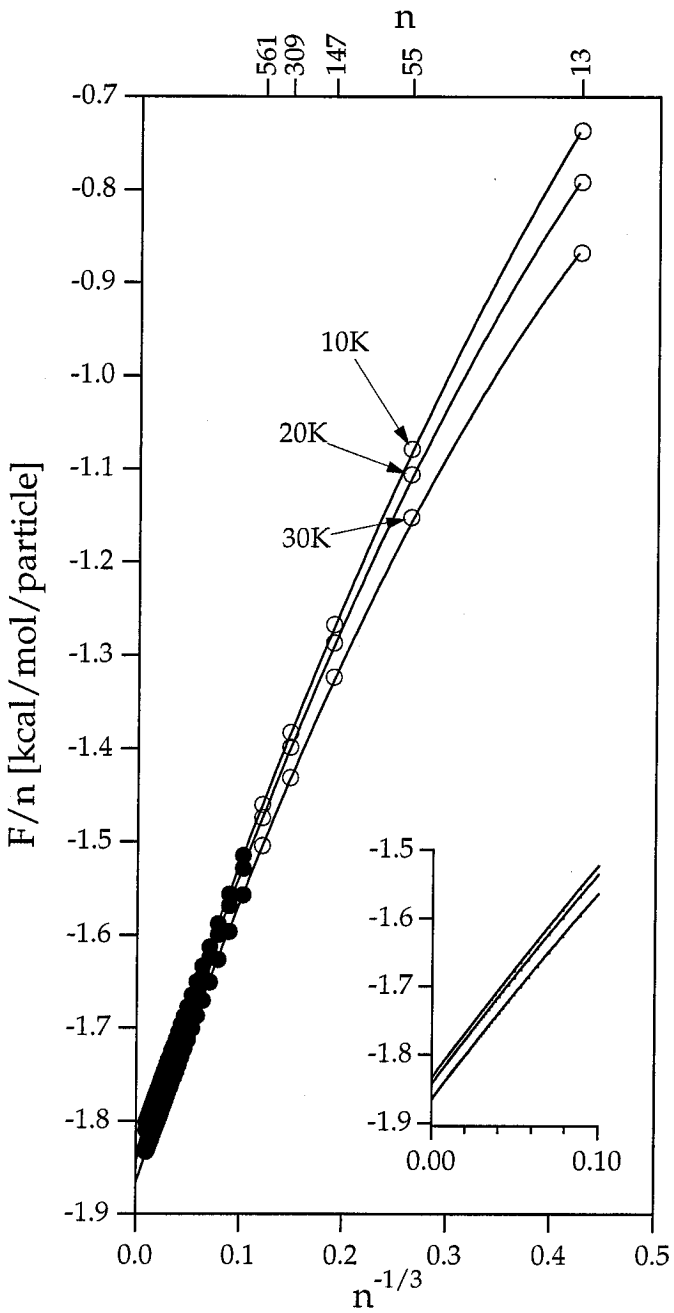

FIGURE 4 Calculated free energy per particle vs $n^{-1/3}$ for Argon as motivated by Eq. (45). The intercept is the bulk chemical potential, the slope at the origin is related to the surface tension, and the curvature is related to the Tolman length. Unfilled circles are from explicit calculations, while filled ones are from extrapolations.

TABLE V The bulk chemical potential (μ), surface tension (σ), and Tolman length (δ) for the solid form of four noble gases, estimated using Eq. (45). For the 0 K evaluations, the temperature-dependent contributions to the free energy were set to zero.

Solid	T (K)	μ $\left(\frac{kcal/mol}{particle}\right)$	σ $\left(\frac{dyne}{cm}\right)$	δ (Å)
Ne	0	-0.443	15.9	0.44
	10	-0.444	16.0	0.60
Ar	0	-1.834	42.1	0.46
	10	-1.834	42.2	0.52
	20	-1.843	42.0	0.59
	30	-1.866	41.5	0.66
Kr	0	-2.631	52.5	0.48
	10	-2.633	52.6	0.53
	20	-2.648	52.3	0.58
	30	-2.681	51.8	0.64
	40	-2.730	51.2	0.70
Xe	0	-3.684	61.8	0.51
	10	-3.687	61.9	0.55
	20	-3.707	61.6	0.60
	30	-3.746	61.2	0.65
	40	-3.803	60.7	0.69
	50	-3.873	60.1	0.74
	60	-3.954	59.5	0.78

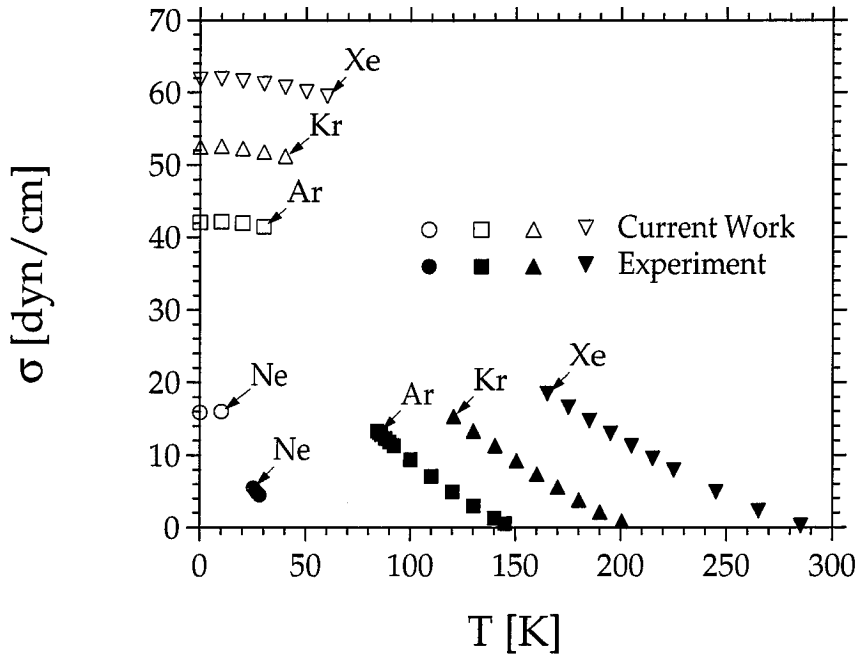

FIGURE 5 Calculated and experimental[18,19] surface tension for four noble gases. The calculated values (open symbols) are for the solid while the experimental values (filled symbols) are for the liquid.

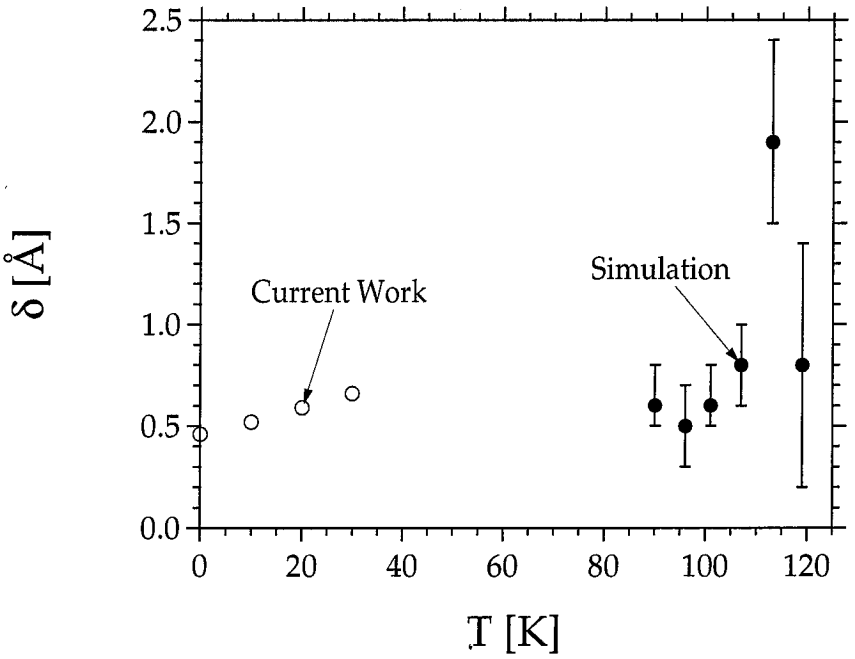

FIGURE 6 Calculated (present work) and simulated[20] (using molecular dynamics) Tolman length for Argon. The error bars on the simulation results are $\pm 1\sigma$.

icosahedral structures and fcc structures[7] may aid in the extrapolation. Nevertheless, these predictions are seen as confirmation of the extrapolation procedure presented herein.

Figure 7 shows the size dependence of the bulk chemical potential and surface tension for argon. Table VI gives expressions for the bulk chemical potential and surface tension for Ne, Ar, Kr, and Xe at several temperatures. It is inherent in the classical approach that the chemical potential is independent of size.

Bulk Properties - Differential Analysis

An alternative to the above analysis is to use a size-dependent bulk chemical potential (rather than a constant). Thus from Figure 4, the slope $[f'(x)]$ and intercept $[f(x)]$ of the tangent line at a given $x = n^{-1/3}$ are used to define the effective bulk chemical potential (μ) and surface tension (σ), respectively

$$\mu = f(x), \tag{46}$$

$$\sigma(4\pi)^{\frac{1}{3}}(3v)^{\frac{2}{3}} = f'(x), \tag{47}$$

where

$$x = n^{-\frac{1}{3}} \tag{48}$$

and

$$f = \frac{F}{n}. \tag{49}$$

Figure 7 shows the size dependence of the effective bulk chemical potential and surface tension using the differential analysis for argon. Table VII gives expressions for the bulk chemical potential and surface tension for Ne, Ar, Kr, and Xe at several temperatures.

Since the classical and differential methods use the same quadratic fits to the free energy data, they contain the same information. The classical approach has the advantage of being simpler, but the differential approach provides additional

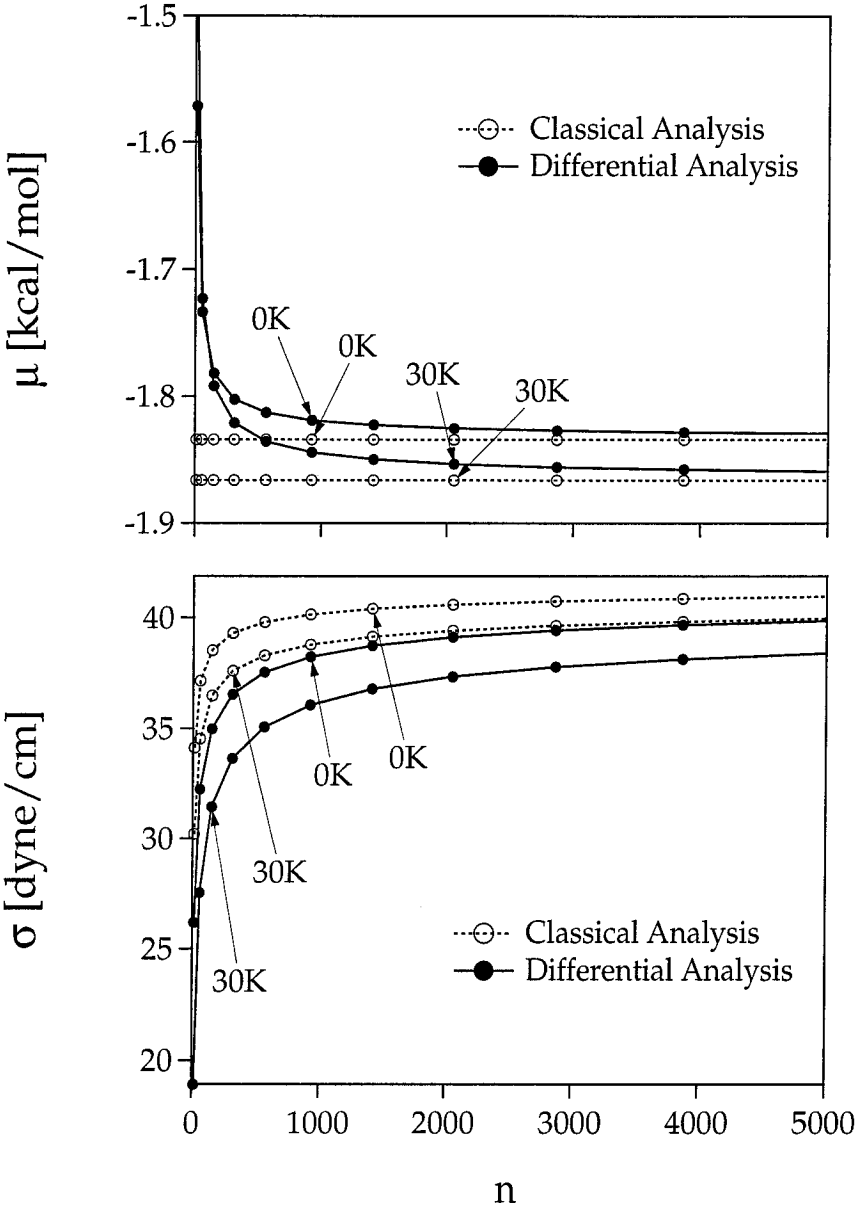

FIGURE 7 a. The bulk chemical potential for solid argon using the classical analysis (dashed lines) and the differential analysis (solid lines). The classical approach assumes that the bulk chemical potential is size independent. b. The surface tension for solid argon using the classical analysis (dashed lines) and the differential analysis (solid lines).

TABLE VI Calculated chemical potential (μ), surface tension (σ), and free energy (F/n) as functions of the number of atoms (n) in a cluster using the classical analysis.

Solid	T (K)	v $\left(\frac{\mathring{A}^3}{particle}\right)$	μ $\left(\frac{kcal}{mol}\right)$	σ $\left(\frac{dyne}{cm}\right)$	F/n $\left(\frac{kcal/mol}{particle}\right)$
Ne	0	22.184	-0.443	$15.9\text{-}7.984n^{-1/3}$	$-0.443+0.874n^{-1/3}-0.439n^{-2/3}$
	10	22.184	-0.444	$16.0\text{-}10.945n^{-1/3}$	$-0.444+0.879n^{-1/3}-0.602n^{-2/3}$
Ar	0	37.465	-1.834	$42.1\text{-}18.643n^{-1/3}$	$-1.834+3.277n^{-1/3}-1.453n^{-2/3}$
	10	37.465	-1.834	$42.2\text{-}21.124n^{-1/3}$	$-1.834+3.287n^{-1/3}-1.647n^{-2/3}$
	20	37.465	-1.843	$42.0\text{-}23.911n^{-1/3}$	$-1.843+3.272n^{-1/3}-1.864n^{-2/3}$
	30	37.465	-1.866	$41.5\text{-}26.554n^{-1/3}$	$-1.866+3.235n^{-1/3}-2.070n^{-2/3}$
Kr	0	45.019	-2.631	$52.5\text{-}22.691n^{-1/3}$	$-2.631+4.622n^{-1/3}-1.999n^{-2/3}$
	10	45.019	-2.633	$52.6\text{-}25.126n^{-1/3}$	$-2.633+4.630n^{-1/3}-2.214n^{-2/3}$
	20	45.019	-2.648	$52.3\text{-}27.703n^{-1/3}$	$-2.648+4.605n^{-1/3}-2.441n^{-2/3}$
	30	45.019	-2.681	$51.8\text{-}30.124n^{-1/3}$	$-2.681+4.560n^{-1/3}-2.654n^{-2/3}$
	40	45.019	-2.730	$51.2\text{-}32.430n^{-1/3}$	$-2.730+4.508n^{-1/3}-2.858n^{-2/3}$
Xe	0	57.661	-3.684	$61.8\text{-}26.439n^{-1/3}$	$-3.684+6.424n^{-1/3}-2.748n^{-2/3}$
	10	57.661	-3.687	$61.9\text{-}28.641n^{-1/3}$	$-3.687+6.431n^{-1/3}-2.976n^{-2/3}$
	20	57.661	-3.707	$61.6\text{-}30.899n^{-1/3}$	$-3.707+6.401n^{-1/3}-3.211n^{-2/3}$
	30	57.661	-3.746	$61.2\text{-}33.020n^{-1/3}$	$-3.746+6.354n^{-1/3}-3.432n^{-2/3}$
	40	57.661	-3.803	$60.7\text{-}35.042n^{-1/3}$	$-3.803+6.300n^{-1/3}-3.642n^{-2/3}$
	50	57.661	-3.873	$60.1\text{-}36.994n^{-1/3}$	$-3.873+6.242n^{-1/3}-3.844n^{-2/3}$
	60	57.661	-3.954	$59.5\text{-}38.894n^{-1/3}$	$-3.954+6.181n^{-1/3}-4.042n^{-2/3}$

TABLE VII Calculated chemical potential (μ), surface tension (σ), and free energy (F/n) as functions of the number of atoms (n) in a cluster using the differential analysis.

Solid	T (K)	v $\left(\frac{\mathring{A}^3}{particle}\right)$	μ $\left(\frac{kcal}{mol}\right)$	σ $\left(\frac{dyne}{cm}\right)$	F/n $\left(\frac{kcal/mol}{particle}\right)$
Ne	0	22.184	-0.443+0.439n$^{-2/3}$	15.9-2*7.984n$^{-1/3}$	-0.443+0.874n$^{-1/3}$-0.439n$^{-2/3}$
	10	22.184	-0.444+0.602n$^{-2/3}$	16.0-2*10.945n$^{-1/3}$	-0.444+0.879n$^{-1/3}$-0.602n$^{-2/3}$
Ar	0	37.465	-1.834+1.453n$^{-2/3}$	42.1-2*18.643n$^{-1/3}$	-1.834+3.277n$^{-1/3}$-1.453n$^{-2/3}$
	10	37.465	-1.834+1.647n$^{-2/3}$	42.2-2*21.124n$^{-1/3}$	-1.834+3.287n$^{-1/3}$-1.647n$^{-2/3}$
	20	37.465	-1.843+1.864n$^{-2/3}$	42.0-2*23.911n$^{-1/3}$	-1.843+3.272n$^{-1/3}$-1.864n$^{-2/3}$
	30	37.465	-1.866+2.070n$^{-2/3}$	41.5-2*26.554n$^{-1/3}$	-1.866+3.235n$^{-1/3}$-2.070n$^{-2/3}$
Kr	0	45.019	-2.631+1.999n$^{-2/3}$	52.5-2*22.691n$^{-1/3}$	-2.631+4.622n$^{-1/3}$-1.999n$^{-2/3}$
	10	45.019	-2.633+2.214n$^{-2/3}$	52.6-2*25.126n$^{-1/3}$	-2.633+4.630n$^{-1/3}$-2.214n$^{-2/3}$
	20	45.019	-2.648+2.441n$^{-2/3}$	52.3-2*27.703n$^{-1/3}$	-2.648+4.605n$^{-1/3}$-2.441n$^{-2/3}$
	30	45.019	-2.681+2.654n$^{-2/3}$	51.8-2*30.124n$^{-1/3}$	-2.681+4.560n$^{-1/3}$-2.654n$^{-2/3}$
	40	45.019	-2.730+2.858n$^{-2/3}$	51.2-2*32.430n$^{-1/3}$	-2.730+4.508n$^{-1/3}$-2.858n$^{-2/3}$
Xe	0	57.661	-3.684+2.748n$^{-2/3}$	61.8-2*26.439n$^{-1/3}$	-3.684+6.424n$^{-1/3}$-2.748n$^{-2/3}$
	10	57.661	-3.687+2.976n$^{-2/3}$	61.9-2*28.641n$^{-1/3}$	-3.687+6.431n$^{-1/3}$-2.976n$^{-2/3}$
	20	57.661	-3.707+3.211n$^{-2/3}$	61.6-2*30.899n$^{-1/3}$	-3.707+6.401n$^{-1/3}$-3.211n$^{-2/3}$
	30	57.661	-3.746+3.432n$^{-2/3}$	61.2-2*33.020n$^{-1/3}$	-3.746+6.354n$^{-1/3}$-3.432n$^{-2/3}$
	40	57.661	-3.803+3.642n$^{-2/3}$	60.7-2*35.042n$^{-1/3}$	-3.803+6.300n$^{-1/3}$-3.642n$^{-2/3}$
	50	57.661	-3.873+3.844n$^{-2/3}$	60.1-2*36.994n$^{-1/3}$	-3.873+6.242n$^{-1/3}$-3.844n$^{-2/3}$
	60	57.661	-3.954+4.042n$^{-2/3}$	59.5-2*38.894n$^{-1/3}$	-3.954+6.181n$^{-1/3}$-4.042n$^{-2/3}$

physical insight. Due to the proximity of the surface, none of the atoms in nanoscale clusters are in a bulk environment. In the classical analysis, these surface effects are "lumped" in with the size dependence of the surface tension while the bulk chemical potential is fixed. In the differential analysis, the chemical potential of the interior atoms approaches the bulk value as the surface becomes sufficiently distant. Future analyses may benefit from explicitly handling the size dependence of the bulk chemical potential in this manner.

3.4 Acknowledgements

We thank Dr. Guanhua Chen for helpful discussions, Dr. Terry Coley for assistance with the vibrational calculations on large systems, and Dr. Siddharth Dasgupta for modifications to POLYGRAF. RBM acknowledges a National Science Foundation Graduate Research Fellowship. Partial support of the work was provided by grants from the NSF (CHE 91-100289, CTS 91-13191, and ASC 92-17368). The computer facilities of the MSC used in this work are also supported by grants from DOE-AICD, Allied-Signal Corp., Asahi Chemical, Asahi Glass, BP America, Chevron, BF Goodrich, Teijin Ltd., Vestar, Hughes Research Laboratories, Xerox, and Beckman Institute.

3.5 References

[1]O. Echt, O. Kandler, T Leisner, W. Miehle, and E. Recknagel, J. Chem. Soc. Faraday Trans. **86**, 2411 (1990); and references therein.

[2]J. A. Northby, J. Chem. Phys. **87**, 6166 (1987), and references therein.

[3]B. Raoult, J. Farges, M. F. DeFeraudy, and G. Torschet, Phil. Mag. B. **60**, 881 (1989), and references therein.

[4]D. L. Freeman and J. D. Doll, Adv. Chem. Phys. **70B**, 139 (1988).

[5]A. W. Hodgson, Adv. Colloid Interface Sci. **21**, 303 (1984), and references therein.

[6]F. F. Abraham, and J. V. Dave, J. Chem. Phys. **55**, 4817 (1971).

[7]A. L. Mackay, Acta Cryst. **15**, 916 (1962).

[8]R. F. K. Herzog, W. P. Poschenrieder, and F. G. Satkiewicz, Radiat. Effects **18**, 199 (1973).

[9]T. L. Hill, *Statistical Thermodynamics* (Dover, New York, 1986), pp. 98-100, 161-167.

[10]The Lennard-Jones parameters used in this study were chosen to agree with the bulk lattice spacing [J. Donohue, *Structures of the Elements* (R. E. Krieger, Malabar, FL, 1982)] and the heat of vaporization at 0K after correcting for zero point energy [R. Hultgren *et al.*, *Selected Values of the Thermodynamic Properties of the Elements* (American Soc for Metals, Metals Park, OH, 1973)]. The method used to calculate Lennard-Jones parameters from this information is detailed elsewhere [N. Karasawa and W. A. Goddard, J. Phys. Chem. **93**, 7320 (1989)].

[11]The coordinates of the atoms in the minimized structures and the vibrational frequencies were determined using POLYGRAF[12] from Molecular Simulations Inc (Burlington, Mass).

[12]A fast routine written by Dr. Terry Coley was used to determine the frequencies for the 561-atom cluster.

[13]L. V. Hove, Phys. Rev. **89**, 1189 (1953).

[14]J. M. Dickey and A. Paskin, Phys. Rev. B **1**, 851 (1970).

[15]J. Xie, J. A. Northby, L. Freeman, and J. D. Doll, J. Chem. Phys. **91**, 612 (1989).

[16]J. D. Honeycutt and H. C. Andersen, J. Phys. Chem. **91**, 4950 (1987).

[17]R. C. Tolman, J. Chem. Phys. **17**, 333 (1949).

[18]J. L. Jasper, J. Phys. Chem. Ref. Data **1**, 841 (1972).

[19]G. A. Cook, *Argon, Helium, and the Rare Gases* (Interscience, New York, 1961).

[20]M. J. Haye and C. Bruin, J. Chem. Phys. **100**, 556 (1994).

Chapter 4 Surface-Melted Clusters

Thermodynamic Properties and Homogeneous Nucleation Rates for Surface-Melted Physical Clusters

Richard B. McClurg and Richard C. Flagan

Spalding Laboratory (210-41),

Division of Chemistry and Chemical Engineering (CN 9141),

California Institute of Technology, Pasadena, California 91125

William A. Goddard III[a)]

Materials and Process Simulation Center, Beckman Institute (139-74),

Division of Chemistry and Chemical Engineering (CN 9141),

California Institute of Technology, Pasadena, California 91125

[a)]To whom correspondence should be addressed.

Abstract

We predict the free energy of van der Waals clusters (F_n) in the surface-melted temperature regime. These free energies are used to predict the bulk chemical potential, surface tension, Tolman length, and vapor pressure of noble gas crystals. Together, these estimates allow us to make definitive tests of the capillarity approximation in classical homogeneous nucleation theory. We find that the capillarity approximation underestimates the nucleation rate by thirty orders of magnitude for argon. The best available experiments are consistent with our calculation of nucleation rate as a function of temperature and pressure. We suggest experimental conditions appropriate for determining quantitative nucleation rates which would be invaluable in guiding further development of the theory. To make the predictions of F_n, we develop the Shellwise Lattice Search (SLS) algorithm to identify isomer fragments and the Linear Group Contribution (LGC) method to estimate the energy of isomers composed of those fragments. Together, SLS/LGC approximates the distribution of isomers which contribute to the configurational partition function (for up to 147-atom clusters). Es-

timates of the remaining free energy contributions come from a previous paper in this series.

4.1 Introduction

The structure and dynamics of neutral, physically bound clusters containing 10 to a few hundred particles are critical to understanding homogeneous nucleation. To date, the only direct experimental probe of homogeneous nucleation is the so-called nucleation theorem.[1] It can be used to determine the size and composition of the critical nucleus, but does not provide information on cluster properties. Since experimental study of clusters in this size range has proved difficult, it is useful to develop theoretical methods.

Noble gas clusters with a broad size distribution can be readily produced using an adiabatic expansion jet.[2] Electron diffraction experiments[3–5] show that small argon clusters formed in a jet adopt 5-fold symmetry. This contrasts with the bulk (fcc) structure that is observed for clusters larger than $N_{fcc}(T)$. At 32 K this limit is, $N_{fcc}(T) \approx 750$ atoms[3] and at 10 K, $1500 \leq N_{fcc}(T) \leq 3500$ atoms.[4,5] Calculations suggest that $N_{fcc}(0K) = 10^5$ atoms.[6] Experiments are somewhat restricted by the distribution of cluster sizes produced in jets. In addition, it is difficult to obtain size-selected neutral clusters since few experimental methods successfully separate neutral clusters beams.[7] Mass spectrometry has sufficient resolution to separate cluster beams into its components, but ionization of the clusters leads to structural changes in the clusters being studied.[8] Neutralization of size-selected ionic clusters produces a narrow size distribution of clusters, but the vibrational energy of the neutralized clusters exceeds that of thermalized clusters at the temperature of the incoming cluster beam.[9] Deflection of a neutral cluster beam with an atomic beam has been used to separate a cluster beam with atomic resolution for small clusters (less than 10 rare gas atoms[10] or up to 13 molecules[11]). Many applications require knowledge of the properties of larger clusters. The deficiencies in the available experimental techniques necessitate theoretical approaches to study the energetics of neutral thermalized clusters.

Most cluster modeling and simulation studies use pairwise additive potentials to simplify the analysis. Even so, the $3n$ degrees of freedom for a cluster of n particles makes determining even the optimum structure challenging. Reviews by Hoare[12] and

Farges *et al.*[13] summarize much of the work in finding candidates for minimum energy structures. More recently, structures have been proposed for each cluster size from 13 to 147 particles,[14] and selected clusters with as many as several thousand particles have been studied.[6,15] Since none of these studies involved exhaustive searches for the global minimum energy, each provides only an upper bound on the minimum potential energy. However, the consensus is that the low energy structures are well understood, making it reasonable to consider the dynamics of clusters using the $(3n)$-dimensional surfaces based on these potentials.

Cluster thermodynamics have been studied using molecular dynamics (MD)[3,12,16–19] and Monte Carlo (MC)[12,19–24] simulations, and statistical-mechanical modeling.[12,18] All three approaches face a formidable challenge: sampling of the potential surface in sufficient detail to faithfully represent the thermodynamically accessible regions. Most approaches waste most of the effort on sampling unimportant regions. The number of local minima for a cluster of a given number of particles (n) indicates the difficulty of this task. Tsai and Jordan identified 1328 minima for the 13-particle cluster,[25] and Berry has suggested that the number of geometrically distinct minima grows exponentially with n.[26] With far too many minima for exhaustive sampling, simulations can become trapped in local potential wells. In this paper, we present an approach for simplifying this endeavor using insights gained from smaller systems to guide the modeling of larger systems.

In Sec. II we review pertinent insights (from simulations) concerning the structure of atomic clusters. In Sec. III, we lay out the statistical-mechanical basis for the Shellwise Lattice Search (SLS) algorithm described in Secs. IV and V. In Sec. VI we present the Linear Group Contribution (LGC) method used to estimate shell energies. Finally, we apply the results of SLS/LGC to the analysis of homogeneous nucleation experiments in Sec. VII.

4.2 Structures

The lowest energy minima of small atomic clusters have icosahedral structures. These structures were first studied by Mackay who characterized them as "a dense non-crystallographic packing of equal spheres."[27] The Mackay icosahedral structures are constructed by surrounding a central atom with successively larger icosahedral shells having the same orientation of their vertices. Shell number one has twelve atoms at the vertices of the icosahedron. The second shell contains twelve atoms at these vertices plus atoms on each of the 30 edges of the icosahedron for a total of 42 atoms in the second shell (a grand total of 55 atoms). Higher-order shells have additional atoms along the edges and in the faces of the icosahedral shell. In general, the number of atoms n in a Mackay structure with N shells is

$$n = 1 + \sum_{x=1}^{N} \left(10x^2 + 2\right) = \frac{1}{3}\left(10N^3 + 15N^2 + 11N + 3\right). \tag{1}$$

Thus, the first 8 Mackay icosahedral structures contain 13, 55, 147, 309, 561, 923, 1415, and 2057 atoms. These are called Magic Numbered Clusters.[28] For clusters intermediate in size between the magic numbers, the excess particles reside on the surface of a dense icosahedral cluster.

Dense icosahedral clusters are solidlike at low temperatures because the atoms vibrate about a single minimum on the potential surface. Of course, these structures are not crystalline solids since they lack translational invariance. Honeycutt and Andersen[16] and Berry *et al.*[17–19] showed that slightly above the minimum energy, there are minima having icosahedral cores with one or more atoms "promoted" onto the surface. Such clusters with incomplete outer layers are called surface melted clusters because the surface atoms diffuse much more rapidly than core atoms.[18] At still higher energies, the cluster samples liquidlike amorphous structures.

We have adopted the concept of inherent structures as proposed by Stillinger and Weber.[29] In this approach, the $(3n)$-dimensional potential surface is divided conceptually into regions corresponding to the potential wells of each of the geometrically

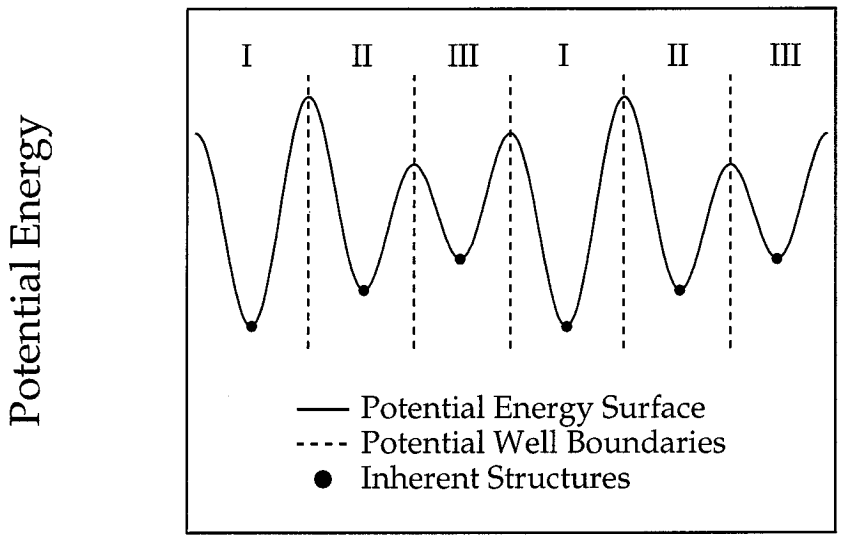

FIGURE 1 Schematic potential surface illustrating the definitions of inherent structures (also called isomers) and potential wells around each isomer. For a cluster of n particles, the 3n-dimensional potential surface can similarly be divided into potential wells, each with an inherent structure of a different structure. Structures that differ only by a permutation of the atoms are indistinguishable and therefore belong to the same isomer.

distinguishable local minima on the potential surface. Geometrically distinguishable configurations cannot be made coincident by a combination of translation and/or rotation of the cluster and permutation of the atoms in the cluster. The structure at the bottom of the well is called the inherent structure for the well. Other configurations within a well are considered as vibrationally excited states of that well's inherent structure. For brevity we refer to the inherent structures as isomers. See Figure 1 for an illustration of these definitions. This framework allows us to express the equilibrium thermodynamic functions for clusters as summations over isomers.

4.3 Configurational Partition Function

The molar free energy for an ideal polyatomic gas,

$$F = -RT \ln\left(\frac{q}{N_a}\right), \tag{2}$$

is calculated[30] from the single-cluster partition function, (q) which can be separated into terms for translation (q_{tr}), rotation (q_{rot}), vibration (q_{vib}), degeneracy (d_j), and the Boltzmann factor,

$$q = \sum_j d_j q_{tr} q_{rot} q_{vib} \exp\left(-E_j/RT\right). \tag{3}$$

The degeneracy and Boltzmann factor account for the contributions from multiple isomers[12] that are important above the melting temperature of the cluster.

Assuming that the cluster rotates rigidly and vibrates harmonically, the partition function becomes

$$\begin{aligned} q = \sum_j \; d_j \; & \left\{ V \left(\frac{2\pi nmkT}{h^2}\right)^{3/2} \right\} \left\{ \left(\frac{\pi^{1/2}}{\sigma_j}\right) \left(\frac{8\pi^2 kT}{h^2}\right)^{3/2} \left(I_A I_B I_C\right)^{1/2} \right\} \\ \times \; & \left\{ \prod_{i=1}^{3n-6} \frac{\exp\left(\frac{-h\nu_i}{2kT}\right)}{1-\exp\left(\frac{-h\nu_i}{kT}\right)} \right\} \exp\left(-E_j/RT\right), \end{aligned} \tag{4}$$

where m is the mass of each particle, σ is the rotation symmetry number, $\{I_A, I_B, I_C\}$ are the principal moments of inertia, V is the volume per cluster, k is the Boltzmann constant, R is the gas constant, and h is Planck's constant. We assume that various isomers differ mainly in their degeneracies, binding energies, and symmetry numbers. This is reasonable since the cluster mass (nm) for each isomer is conserved and the product of the principal moments of inertia $(I_A I_B I_C)$ is nearly constant for these roughly spherical isomers. This assumption will be bourne out by what follows. We further assume that the vibrational frequency distribution $\{\nu_i\}$ is barely changed by the small number of defects defining the differences between isomers.[31] Also, Eq. (4) assumes fixed volume, restricting these results to the low pressure limit. For a

Lennard-Jones gas, the low pressure limit applies for total pressures much less than the characteristic pressure (D_e/R_e^3) which is about 300 atm for argon.[24] The Lennard-Jones energy parameter (D_e) and distance parameter (R_e) are discussed further in Sec. VI.

From Eqs. (2) and (4), the free energy can be written as

$$\begin{aligned} F = E^{min} + \sum_{i=1}^{3n-6} \frac{h\nu_i}{2} &- RT \ln \left\{ V \left(\frac{2\pi nmkT}{h^2} \right)^{3/2} \right\} \\ &- RT \ln \left\{ \pi^{1/2} \left(\frac{8\pi^2 kT}{h^2} \right)^{3/2} (I_A I_B I_C)^{1/2} \right\} \\ &- RT \sum_{i=1}^{3n-6} \ln \left\{ \frac{1}{1 - \exp\left(\frac{-h\nu_i}{kT}\right)} \right\} \\ &- RT \ln \left\{ \sum_j \left(\frac{d_j}{\sigma_j} \right) \exp\left(-\frac{E_j - E^{min}}{RT} \right) \right\}, \end{aligned} \tag{5}$$

where E^{min} denotes the global minimum potential energy of the cluster.

The last term in Eq. (5), called the configurational free energy, is used to define a configurational partition function.

$$q_{config} = \sum_j \left(\frac{d_j}{\sigma_j} \right) \exp\left(-\frac{E_j - E^{min}}{RT} \right). \tag{6}$$

This definition differs from previous definitions[12] because of the inclusion of the symmetry number (σ_j). We feel that its inclusion is justified since σ_j is much more isomer-dependent than the remainder of q_{rot}. This inclusion greatly simplifies the accounting for rotationally equivalent isomers and estimating the rotational symmetry of individual isomers. The details appear in the appendix.

Cheng and Berry[18] (CB) published an analytic model for estimating the configurational partition function in which atoms of the outer layer of the cluster are "promoted" to the surface as "floaters" to form the various isomers. In CB, the floaters populate equivalent and noninteracting lattice sites on the cluster surface. The degeneracy d_j is estimated as C_i^j, the binomial coefficient for i items selected

from j, where j is the capacity of the shell.

While quite simple, the CB model has several serious deficiencies, several of which were acknowledged by CB.[18]

1. Holes are arbitrarily restricted to the outermost layer of the cluster.

2. Rotationally equivalent configurations are counted incorrectly as distinct isomers.

3. No allowance is made for the reduction in rotational states by the point symmetry of the isomers.

4. The number of accessible sites changes as the shell is populated.[14]

5. The distinct binding sites on the cluster surface do not have the same energies.[14]

6. Intrashell interactions among the promoted atoms (neglected in CB) become progressively more important as the shell becomes more densely filled.

Deficiencies 1-3 are satisfied through our method for constructing isomers and estimating degeneracies from fragments (Sec. IV and the appendix), deficiency 4 is addressed using our Shellwise Lattice Search algorithm (SLS) to identify acceptable fragments (Sec. V), and deficiencies 5-6 are handled via our Linear Group Contribution method (LGC) to estimate the binding energy of each isomer (Sec. VI). Together, SLS/LGC generates the data needed to more accurately estimate q_{config} [Eq. (6)].

4.4 The Core Plus Shell Model

Since the interaction potential is considered as pairwise additive, we will partition the cluster into a central core and an outer shell and then evaluate their degeneracies and energetics separately,

$$E_j = E^{shell} + E^{core} + E^{shell/holes}. \tag{7}$$

The core may contain holes due to promoted atoms, but we assume that it retains much of the structure of a Mackay icosahedral cluster. This assumption is supported by simulation results.[16–19] The shell contains the promoted atoms and the atoms that would be left over after constructing the largest Mackay icosahedral cluster with all of the given atoms. In Sec. VI we describe a method for calculating the energy of interactions among shell atoms and with a dense core. We use a mean-field estimate to account for the energetics of holes in the core which is also described in Sec. VI.

The degeneracy associated with Eq. (7) is written as

$$d_j^{rot} = d^{shell} \cdot d^{core}, \tag{8}$$

where the superscript "rot" is a reminder that Eq. (8) overestimates the number of distinct isomers due to rotational equivalence. Rotational equivalence is a special case of permutation of equivalent atoms. No such permutation can produce distinguishable isomers. Two tasks remain: to calculate the degeneracy and energy of the core itself, and to avoid overcounting of rotationally equivalent configurations.

The core, in turn, can be viewed as composed of an inner core and a full or nearly-filled outer shell. Thus, the method described in Eqs. (7) and (8) can also be applied to the core of the full cluster. This procedure can be applied recursively until the remaining atoms form a cluster for which the energy is known. (In practice, this is either a complete Mackay icosahedral cluster or a cluster with fewer than 13 atoms.) Mathematically, the procedure is as follows:

$$E_j - E^{min} = \Delta E^{holes} + \sum_{\alpha=1}^{N} \Delta E_{\alpha,c}^{shell}, \tag{9}$$

$$\Delta E_{\alpha,c}^{shell} = E_{\alpha,c} - E_{\alpha}^{min}, \tag{10}$$

$$\Delta E^{holes} = \sum_{\alpha=1}^{N-1} \sum_{\beta=\alpha+1}^{N} E_{\alpha,\beta}^{shell/holes}, \tag{11}$$

$$d_j^{rot} = \prod_{\alpha=1}^{N} d_{\alpha,c}^{shell}, \tag{12}$$

where N is the largest shell containing particles, α and β are shell indices, and c specifies the configuration of shell α. Specifying a set of shell configuration indices $\{c_1, c_2, \ldots, c_N\}$ implies the number of filled sites $\{f_1, f_2, \ldots, f_N\}$ and thus the number of holes $\{h_1, h_2, \ldots, h_N\}$ in each shell. Together, these sets are equivalent to specifying a unique isomer index (j) since the inter-shell interactions are estimated using a mean-field approach (through $\Delta E_{\alpha,c}^{shell}$ and ΔE^{holes}).

In the appendix we demonstrate that

$$\frac{d_j}{\sigma_j} = \frac{d_j^{rot}}{g}, \tag{13}$$

where

$$g = \begin{cases} 120, \text{ for the 19-atom PIC cluster,} \\ 60, \text{ otherwise.} \end{cases}$$

Polyicosahedral clusters (PIC) are rare special cases. See the appendix for further details. The simplicity of Eq. (13) relies on the inclusion of σ_j in the definition of q_{config} [Eq. (6)]. Thus, the 2^{nd} and 3^{rd} deficiencies listed in Section III are much easier to address simultaneously than separately.

Equations (6), (9), (12), and (13) provide a systematic form for calculating q_{config},

$$q_{config} = \frac{1}{g}\sum_h \exp\left(\frac{-\Delta E^{holes}}{RT}\right)\left\{\prod_{\alpha=1}^{N}\left[\sum_c d_{\alpha,c}^{shell}\exp\left(\frac{-\Delta E_{\alpha,c}^{shell}}{RT}\right)\right]\right\}. \tag{14}$$

In Sec. V we present methods to estimate the degeneracies ($d_{\alpha,c}$) of the various shells. In Sec. VI we present methods to estimate the energetics of the shells ($\Delta E_{\alpha,c}^{shell}$) and of the holes ($\Delta E^{holes}$).

4.5 Degeneracies

Lattices and Site Filling Rules (SFR)

Northby[14] used a lattice-based method to identify candidates for the minimum potential energy of clusters with partially filled outer shells and dense Mackay icosahedral

TABLE I Types of lattice sites for the first four shells. Z is the coordination number with atoms in the underlying shell.

Shell	Type of Sites	Z	Sublattice	Quantity	Shell Capacity (f^{max})
0	central	-	-	1	
					1
1	vertex	1	IC	12	
					12
2	faces	3	FC	20	
	edge	2	IC	30	
	vertex	1	IC/FC	12	
					42
3	centered face	3	IC	20	
	off-center face	3	FC	60	
	edge	2	IC	60	
	vertex	1	IC/FC	12	
					92
4	type 1 face	3	FC	60	
	type 2 face	3	FC	60	
	type 3 face	3	IC	60	
	edge	2	IC	90	
	vertex	1	IC/FC	12	
					162

cores. He used projections of the cluster surface similar to the ones in Figure 2. Table 1 categorizes the lattice sites for the first four shells:

1. Face sites with three underlying neighbors

2. Edge sites balanced on two underlying neighbors

3. Vertex sites perched atop one underlying neighbor

Northby also defined sublattices which can be completely filled:

IC. The icosahedral sublattice is filled in the Mackay Icosahedral structures. IC sites are shaded white in Figure 2.

FC. The face-centered sublattice contains those sites which are not part of the IC sublattice and the vertex sites (which are part of both sublattices). In Figure 2, the FC sites are either shaded black or stars.

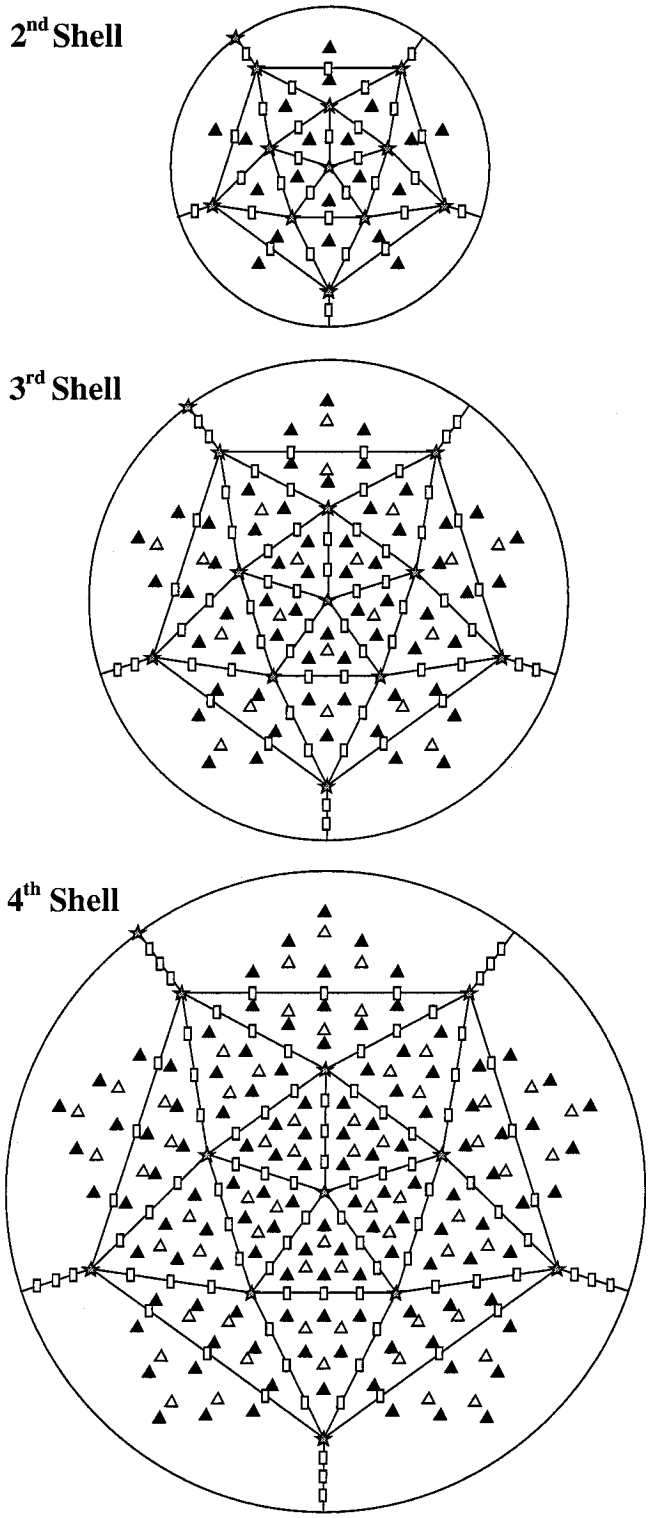

FIGURE 2 Projection of the 2^{nd}, 3^{rd}, and 4^{th} shells showing the lattice sites: face (△), edge (▯), and vertex (☆). Higher order shells have additional edge and face sites. White symbols belong to the IC sublattice, black symbols to the FC sublattice, and stars to both lattices.

From an analysis of the global minimum potential energy structures by Northby, we obtain the following generalized Site Filling Rules (SFR):

SFR 1. FC sites can be filled if the adjacent IC sites are empty.

SFR 2. Edge sites can be filled if the adjacent face sites are empty *and* at least two of the adjacent IC sites are filled.

SFR 3. Vertex sites can be filled if at least four of the five adjacent edge sites *or* all five adjacent face sites are filled.

Rule 1 is due to hard core repulsions between neighboring sites. Rules 2 and 3 arise because edge and vertex sites are not at local minima with respect to the core and must therefore be stabilized by other atoms in the shell.

We use the site filling rules (SFRs) to screen proposed isomers in a Monte Carlo sampling algorithm. First, configurations are generated by filling randomly selected lattice sites. Then the rules are applied to determine if the configuration is valid. If it is valid, the configuration is recorded so that its energy can be estimated. (See Sec. VI for the estimation procedure.) The ratio of the number of accepted configurations to the number of trial configurations estimates the proportion of valid configurations among the configurations in the sample space. Standard binomial statistics are used to place error estimates on that ratio.[32] The balance of Sec. V describes two sample spaces and corresponding sampling procedures (BSA and TBSA) which are applied to the 2^{nd} and 3^{rd} shells.

The Building Shell Algorithm (BSA)

The simplest procedure for identifying acceptable isomers is to start with the empty lattice described above and fill some of the sites. Configurations with more filled sites than the shell capacity need not be considered. Table II gives the size of the sample space for applying this method to the 2^{nd} through the 4^{th} shell. Clearly, there are too many configurations to enumerate them all.

TABLE II Shell capacity (f^{max}), number of lattice sites (L), and sample space size (S) for enumerating all lattice fillings (up to their capacity) for three shells.

Shell	2	3	4
f^{max}	42	92	162
L	62	152	282
S	$\sum_{f=1}^{42} C_f^{62}$	$\sum_{f=1}^{92} C_f^{152}$	$\sum_{f=1}^{162} C_f^{282}$
	$\approx 4.6 \times 10^{18}$	$\approx 5.7 \times 10^{45}$	$\approx 7.7 \times 10^{84}$

We use a Monte Carlo sampling procedure to estimate the total number of acceptable configurations and to identify particular configurations representative of the isomer distribution. Conceptually, we partition the sample space into sections with each section having the same number of filled sites (f) in shell α and then sample from each section separately. (In practice, all sections were done concurrently, but each section was analyzed separately.) Let x_c be the number of configurations of type c out of X randomly selected configurations. Configuration c has f filled lattice sites in a shell having L lattice sites. Then the estimated degeneracy of configuration c is the product of the fraction of acceptable configurations (P_c) and the size of the sample space (S_f).

$$d_c^{shell} = P_c \cdot S_f, \tag{15}$$

$$P_c = \frac{x_c}{X}. \tag{16}$$

The size of the sample space (S_f) is the number of combinations of L lattice sites taken f at a time.

$$S_f = C_f^L = \frac{L!}{(L-f)!f!}. \tag{17}$$

We report a 95% confidence interval for the composite acceptance ratio (P) based on the Gaussian approximation to the binomial distribution (appropriate if $\min[x, X - x] \geq 5$),[32]

$$x = \sum_c x_c|_f, \tag{18}$$

TABLE III Number of iterations (X) and computation time for implementation of two sampling algorithms applied to two shells.

Shell	Algorithm	X	Computer	Computation Time
2	BSA	10^9	IBM RISC 6000	3 wks elapsed time
2	TBSA	1.024×10^8	Intel Touchstone Delta	1.5h elapsed time 770h cpu time
3	BSA	10^9	Intel Touchstone Delta	4.5h elapsed time 2300h cpu time
3	TBSA	2.00192×10^7	Intel Touchstone Delta	12h elapsed time 6200h cpu time

$$P = \sum_c P_c|_f = \frac{x}{X} \pm 1.96\sqrt{\frac{x}{X^2}\left(1 - \frac{x}{X}\right)}. \tag{19}$$

Table III gives the number of trial configurations X and the computation time for investigations of the 2^{nd} and 3^{rd} shells using this building shell algorithm (BSA). An IBM RISC 6000 was used to investigate the 2^{nd} shell. The Intel Touchstone Delta[33] computer was used for the balance of the sampling runs.

Figure 3 gives the acceptance ratio (P) for the 2^{nd} and 3^{rd} shells as a function of the number of filled sites (f) using BSA. This figure illustrates the deficiency of BSA. The acceptance ratio is too small ($P < 10^{-6}$) to get a statistically meaningful sample for all but the most dilute ($f < 20$) sections. BSA is useful, however, as a check on the more practical (but more complicated) algorithm presented below and as a subroutine in that algorithm.

The Tearing then Building Shell Algorithm (TBSA)

Hard core repulsions between neighboring FC and IC sites (SFR 1) are the most common cause for rejecting conformations in the BSA. This suggests using a sampling algorithm which uses these repulsions to reduce the sample size (S) rather than to reject conformations. We describe this Tearing then Building Shell Algorithm (TBSA) next.

Whereas BSA began with an empty shell, each of the X iterations of the TBSA

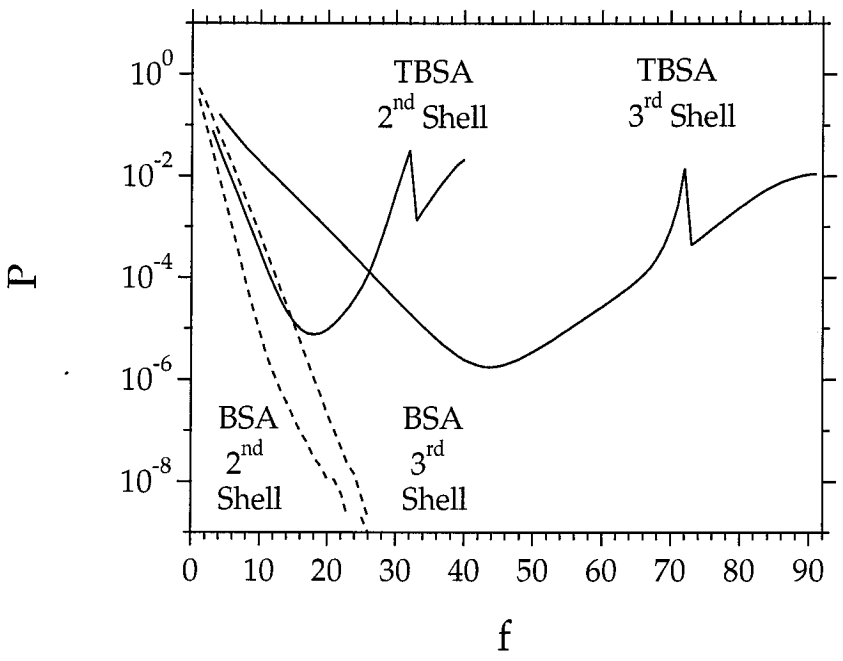

FIGURE 3 Acceptance ratio (P) as a function of the number of filled lattice sites (f) for two sampling algorithms (BSA and TBSA) applied to the 2^{nd} and 3^{rd} shells. For TBSA, filling of the FC sublattice leads to a decrease in (P) beyond f=32 for the 2^{nd} shell and f=72 for the 3^{rd} shell.

begins with a filled IC shell. First, some of the IC atoms are randomly selected for removal from the IC shell. Next, the FC sites are investigated to determine which would be free of hard-core repulsions if they were filled. Subshells with IC filled sites and FC available sites are tabulated in $x(IC, FC)$. Then, Y iterations of the BSA are used to sample the available FC sites. Finally, SFR 2 and 3 are used to screen the composite ($IC \cup FC$) shell conformations. Acceptable conformations of type c are tabulated in y_c. As with the BSA, the estimated number of configurations is the product of an acceptance ratio (P_c) and a sample space size (S_c)

$$d_c^{shell} = P_c \cdot S_c, \tag{20}$$

$$P_c = p1 \pm 1.96 \sqrt{\frac{p1(1-p1)}{Y \sum_{i=FC}^{FC^{max}} x(IC,i)}}, \tag{21}$$

$$p1 = \frac{y_c}{Y \sum_{i=FC}^{FC^{max}} x(IC,i)}. \tag{22}$$

The major improvement over the BSA is the reduced sample size; however, that advantage comes at the cost of a more complicated analysis. Since the number of available FC sites is not known *a priori*, TBSA requires that the size of the sample space (S_c) be estimated along with the acceptance ratios ($p1, p2$),

$$S_c = \frac{(IC^{max})!}{(IC^{max}-IC)!(IC)!} \left\{ \sum_{i=FC}^{FC^{max}} p2 \left(\frac{i!}{(i-FC)!(FC)!} \right) \right. \\ \left. \pm 1.96 \frac{\sqrt{\sum_{i=FC}^{FC^{max}} p2(1-p2) \left(\frac{i!}{(i-FC)!(FC)!} \right)^2 / X}}{\sum_{i=FC}^{FC^{max}} p2 \left(\frac{i!}{(i-FC)!(FC)!} \right)} \right\}, \tag{23}$$

$$p2 = x(IC,i)/X. \tag{24}$$

The factor in front of the braces in Eq. (23) is the number of ways of removing IC of the icosahedral atoms in the first stage of the TBSA. The term within the braces represents the number of ways of filling in FC of the available face-centered sites. We used the same approximation[32] to the binomial distribution as in Eq. (19) and standard rules for error propagation[34] in deriving the 95% confidence limits on P_c and S_c. Figure 4 shows that SLS identifies far fewer valid shell configurations than the CB estimate.[18] This demonstrates that properly treating the internal structure of the shells reduces the number of acceptable configurations, particularly for shells that are roughly half filled.

Table III gives the number of trial configurations X and the computation time on the Intel Touchstone Delta[33] computer for investigations of the 2^{nd} and 3^{rd} shells using TBSA.

Figure 3 gives the composite acceptance ratio,

$$P = \sum_c p1 \cdot p2|_f = \sum_c y_c / fXY|_f, \tag{25}$$

for the 2^{nd} and 3^{rd} shells as a function of the number of filled sites (f) using TBSA.

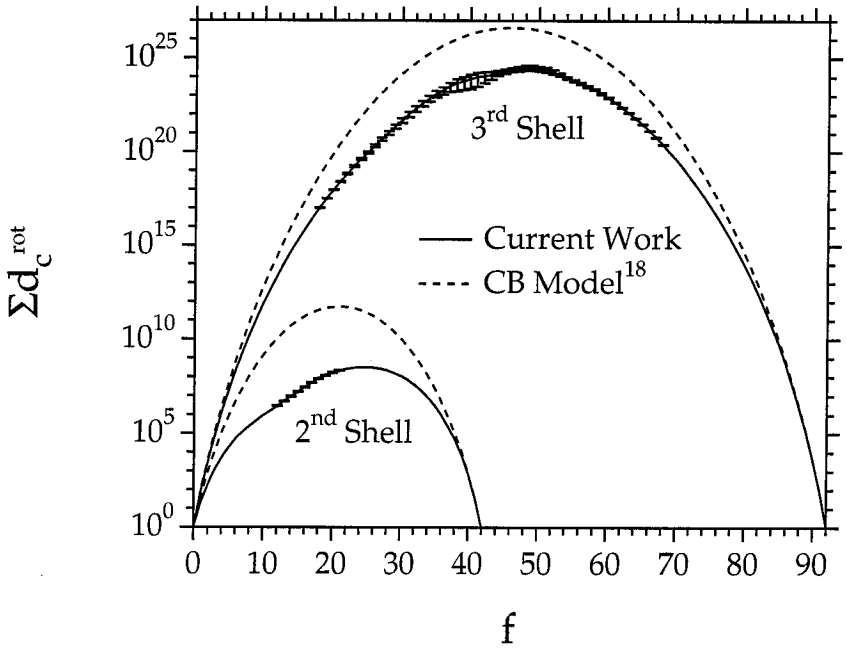

FIGURE 4 The number of geometrically distinguishable shell isomers ($\sum d_c^{rot}$) (including rotationally equivalent isomers) as a function of the number of filled lattice sites (f). Solid lines represent the results of this study. For clarity, the 95% confidence limits have been omitted for cases where the error is less than 2% of the total. Dashed lines (CB) are the estimates of Cheng and Berry[18] which do not account for the internal structure of the shells.

The worst acceptance ratios are $P = 10^{-5}$ for the 2^{nd} shell and $P = 10^{-6}$ for the 3^{rd} shell, justifying the added complexity of TBSA.

4.6 Energetics

Interaction Potential

To this point, we have not specified an interaction potential between particles. The discussion and results of Sec. V are purely geometric. We have merely assumed that the particles pack like spheres and that their interactions are pairwise additive. Therefore, any two-body radial interaction potential could be used to estimate the energetics of the isomers fragments identified using BSA or TBSA. We use the Lennard-Jones potential to take advantage of previously published minimum energy structures[14] and correlations for the temperature-dependent contributions to the free energy,[35]

$$\epsilon = \rho^{-12} - 2\rho^{-6}, \tag{26}$$

$$\epsilon = E/D_e, \tag{27}$$

$$\rho = r/R_e. \tag{28}$$

Some typical Lennard-Jones parameters (R_e, D_e) are tabulated[36] in Table IV.

Linear Group Contribution (LGC) Method for Estimating the Shell Energy

The lattice method described in Section V provides information which can be used to estimate the difference in energy between various configurations. In principle, each of the accepted configurations could be used as a starting point for an off-lattice energy minimization and the resulting energy could be recorded. However, Figure 4 shows that there are far too many configurations for that approach to be practical. Instead we use a Linear Group Contribution (LGC) method which efficiently estimates shell

TABLE IV Parameters and characteristic quantities for sample systems.[36] There are two energy scales, D_e and $h\nu_{char}$. D_e determines the potential energy at the optimal structure while $h\nu_{char}$ determines the zero-point energy and vibrational contributions. Boiling point data is from Ref. 41.

Quantity	Units	Ne	Ar	Kr	Xe
m	(amu)	20.179	39.948	83.80	131.30
D_e	(kcal/mol)	0.0726	0.237	0.325	0.446
R_e	(Å)	3.249	3.867	4.109	4.465
$\nu_{char} = \frac{1}{2\pi R_e}\sqrt{\frac{D_e}{m}}$	(GHz)	60.12	64.86	49.35	42.50
	(cm^{-1})	2.004	2.162	1.645	1.417
$E_{char} = h\nu_{char}$	(cal/mol)	5.729	6.181	4.704	4.051
$T_{char} = \frac{h\nu_{char}}{k}$	(K)	2.883	3.111	2.367	2.039
$I_{char} = mR_e^2$	(amu Å^2)	213.0	597.4	1415	2618
T_{boil}	(K)	27.1	87.3	119.8	165.0
kT_{boil}/D_e	(-)	0.742	0.732	0.732	0.735

energies by explicitly including the main interactions, but only indirectly including more distant pairs,

$$E_{LGC}^{shell} = -\sum_i N_i E_i. \tag{29}$$

In Eq. (29), N_i is the number of occurrences of the i^{th} group and E_i is the energy contribution of that group. LGC places isomers having similar energies into the same bin. Each bin is defined to contain isomers with the same set $\{N_i\}$. This is efficient since a small number of bins suffice to represent a huge number of total isomers. Each of the group contributions in the model were fitted to differences in energy between previously published minimum potential energy configurations.[14] By fitting to minimum energy configurations, we expect the energy parameters (E_i) to implicitly include contributions from non-first neighbor pairs that are not explicitly counted in the LGC model. The groups and their energy contributions are given in Table V for two potentials.

Figure 5 shows that the LGC model reproduces the binding energy of Northby's structures[14] to within 1% or $0.5D_e$. The accuracy of this fit justifies the use of the LGC method to estimate the energy of other structures. There are slight systematic trends in the residuals due to the effect of 2^{nd} and more distant neighbors. Thus,

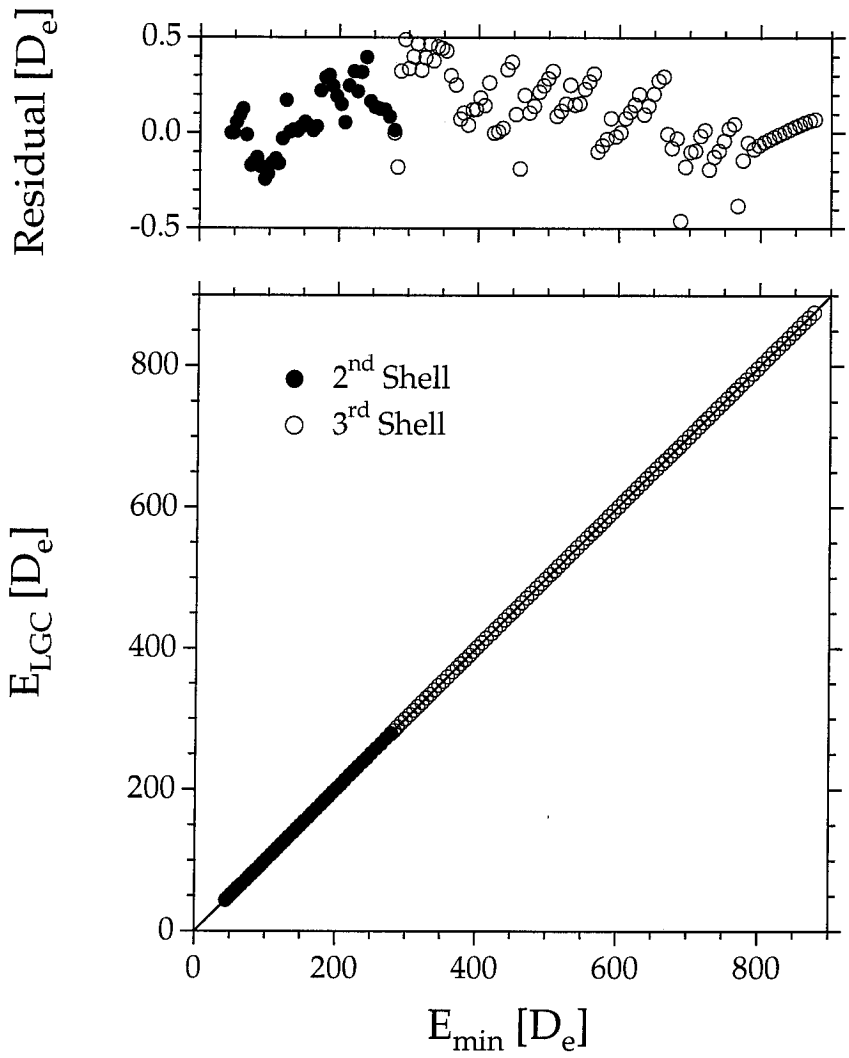

FIGURE 5 Cluster energy (E_{min}) as determined from off-lattice minimization[14] versus the LGC prediction (E_{fit}). The line y=x represents perfect agreement. Since the LGC method faithfully reproduces the published results, we use it to estimate binding energies of other structures. The residual $E_{LGC} - E_{min}$ is shown separately; it remains smaller than $0.5D_e$.

TABLE V Linear Group Contribution (LGC) parameters ($\frac{E_i}{D_e}$) for two potentials. The parameters based on the Lennard-Jones potential are similar to those based on the square-well potential, indicating that the Lennard-Jones-based parameters are dominated by first-neighbor interactions.

Potential	Square Well	Lennard-Jones		
Shell	(all)	2^{nd}	3^{rd}	4^{th}
Inter-Shell Interactions				
Centered face	3	3.518	4.217	N/A
Off-center face	3	N/A	4.213	4.612
Edge	2	2.184	2.690	
Vertex supported by FC particles[a]	6	5.968	6.279	
Vertex supported by IC particles	1	0.588	1.195	
IntraShell Interactions				
FC / FC	1	1.015	0.994	1.004
IC / IC	1	1.522	1.241	
Edge / vertex	1	1.276	1.200	
5-member ring of face particles	0	-0.470	-0.148	
5-member ring of edge particles	0	-0.460	0.383	

[a] This group contribution includes five face/vertex interactions since they are implied by SFR 3. (See Sec. V.)

the precision of the shell energy estimates can be improved through the use of the (published) minimum energy configurations,

$$\Delta E^{shell} \equiv E^{shell} - E^{shell}_{min} \approx \left(E^{shell} - E^{shell}_{min}\right)_{LGC}. \tag{30}$$

For this reason, the LGC method is used to estimate energy differences between clusters with different surface shells. Recall that E^{shell} is the energy of interaction among the shell atoms and with a dense core. Hole effects are covered below.

Although the LGC parameters are fitted to Eq. (30), they have physical interpretations. The intershell interaction terms reflect the interactions between shell atoms and a dense core. The FC/FC, IC/IC, and edge/vertex terms reflect intrashell interactions. There is no edge/face interaction term since configurations containing such interactions have high energies due to hard-core repulsions. ($E_{e/f}$ would be very large and positive, which is the basis for SFR 1.) There is no separate face/vertex interaction term since its energetics are confounded by the requirement that a vertex atom

be surrounded by all five face atoms. The corresponding edge/vertex interaction is not confounded since four edge atoms are sufficient to support a vertex atom. (SFR 3)

Two subtle effects lead to contributions from five-membered rings. The first effect involves the loss of one easy degree of freedom for the relaxation of atoms within the shell. For five atoms in a ring, there are five pairs of which any four pairs can relax across the saddles between lattice sites. Simultaneous relaxation of the 5^{th} pair would shorten the circumference of the ring causing all five atoms to "climb" the hard core of the vertex particle's potential. This implies that all five pairs cannot simultaneously reduce the cluster energy by relaxing across a saddle. Therefore, the first effect tends to make the five-membered ring contribution negative. The second effect involves 2^{nd} neighbors. Since the number of five-membered rings correlates with the number of distant pairs (which are not explicitly included in the LGC method), the five-membered ring contributions include this positive effect. Therefore, the five-membered ring group contributions are a balance between these competing effects.

Hole Energy

We use a mean-field approach to calculate the interaction energy between holes in shell α and the atoms in shell β ($E_{\alpha,\beta}^{shell/holes}$). For each of the h_α holes in shell α, we use the average energy of interaction (ϵ) between particles at the L_α lattice sites in shell α and particles at all of the L_β lattice sites in shell β. The distances ($r_{t,u}$) between the hole sites (t) and particle sites (u) are estimated using the corresponding distances between particles in minimized dense clusters.[37]

$$E_{\alpha,\beta}^{shell/holes} = f_\beta h_\alpha \sum_{t=1}^{L_\alpha} \sum_{u=1}^{L_\beta} \epsilon(r_{t,u})/(L_\alpha L_\beta). \tag{31}$$

Conceptually useful subsets of the isomer distribution can be characterized by the total number of holes (h),

$$h = \sum_{\alpha=1}^{N} h_\alpha, \tag{32}$$

TABLE VI Mean-field estimate of the hole interaction energy for a single hole interacting with a single occupied lattice site, $E_{\alpha,\beta}^{shell/holes}/(D_e h_\alpha n_\beta)$. See Eq. 31.

Hole Index (α)	Shell Index (β)	Hole Interaction Energy $\left(\frac{E_{\alpha,\beta}^{shell/holes}}{D_e h_\alpha n_\beta}\right)$	Cluster Sizes Used[37]
1	2	0.2212	14,55
1	3	0.02374	56,147
1	4	0.002823	148,309
2	3	0.07861	56,147
2	4	0.008270	148,309
3	4	0.04034	148,309

and the total number of particles (n),

$$n = \sum_{\beta=1}^{N} f_\beta. \tag{33}$$

Since the relative orientations of shells α and β do not appear in Eq. (31), this is a mean-field estimate. Values for $E_{\alpha,\beta}^{shell/holes}$ are summarized in Table 6.

Distribution of Inherent Structures

The LGC method along with the mean field estimate for the hole interaction energy can be used to generate the distribution of cluster inherent structures from the purely geometric data in Section V. We will illustrate using the 55-atom cluster because we can compare with other detailed studies.[18,24,38,39] With zero holes ($h = 0$), there is only one unique minimal structure, with a rotational symmetry number of 60. With one hole ($h = 1$), the hole can reside at a vertex site in the first shell or at an edge or vertex in the second shell. Furthermore, the promoted atom can occupy one of 20 centered local minima or 60 off-center local minima in the third shell. This gives rise to six additional groups of structures. (See Table VII.) The off-lattice energies for four of these isomers have been calculated explicitly by Doye and Wales.[39] Their values are reproduced in Table VII and are consistent with the previously stated accuracy

TABLE VII Isomer energies for the 55-atom cluster.

j	Structure	E_j^{39} (D_e)	E_j^{LGC} (D_e)	d_j/σ_j
0	Mackay Icosahedron	-279.248	-279.248	1/60
1	2^{nd} Shell vertex vac., face-centered cap	-276.597	-276.418	4
2	2^{nd} Shell vertex vac., off-center cap	-276.199	-276.415	12
3	2^{nd} Shell edge vac., face-centered cap	-274.090	-273.482	10
4	2^{nd} Shell edge vac., off-center cap		-273.479	30
5	1^{st} Shell vacancy, face-centered cap		-267.791	4
6	1^{st} Shell vacancy, off-center cap		-267.788	12
7+	Many others ...			

of the LGC method. ($\pm 0.5 D_e$) Allowing additional holes leads to a huge number of inherent structures with higher energies.

Figure 6 shows the convergence of the SLS/LGC method for the 55-atom cluster as a function of the maximum number of holes. To interpret Figure 6, note that ($E - E^{min} \leq nkT_b/2 \approx 21 D_e$) corresponds to the normal boiling point. Thus a maximum of six holes is sufficient to generate the classically accessible structures at the normal boiling point. Our results are similar to Ref. 38 (based on simulated quenching) with the differences arising from our inclusion of the rotational symmetry number and from the finite sample generated by quenching. Also shown is the prediction of the CB model.[18] By ignoring the structure of the various shells, this model tends to over-estimate the number of inherent structures, particularly for non-magic-numbered clusters. It should be noted that Cheng and Berry chose to apply their model only to magic number clusters. Subsequent modeling studies should be tested on magic number and non-magic number clusters to avoid this bias.

Figure 7 shows the cumulative distribution of structures as a function of binding energy for clusters having 15 to 140 atoms. (For clarity, only every fifth cluster size is

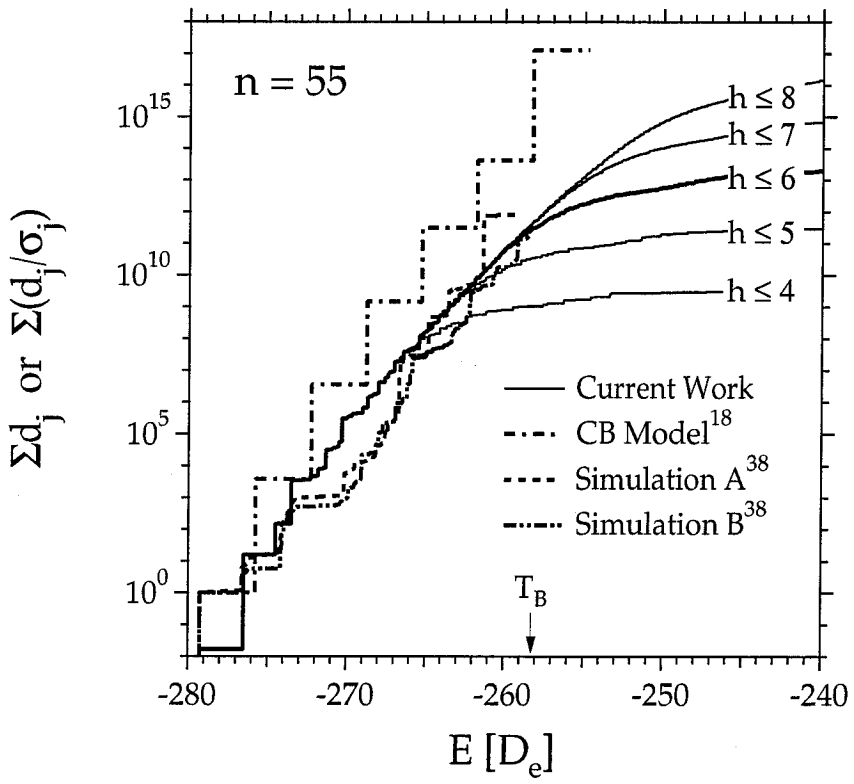

FIGURE 6 Cumulative number of isomers ($\sum_{E_j \leq E} d_j^{rot}$) as a function of binding energy (E) for a cluster of 55 particles. The curves demonstrate the effect of limiting the total number of holes (h). We find that six holes are sufficient to generate most cluster isomers contributing significantly to the partition function at temperatures up to the normal boiling point. ($E - E_{min} \approx 21 D_e$ or $E = -258 D_e$). The prediction of the Cheng and Berry model[18] and results based on simulations by Doye and Wales[38] are also shown for comparison.

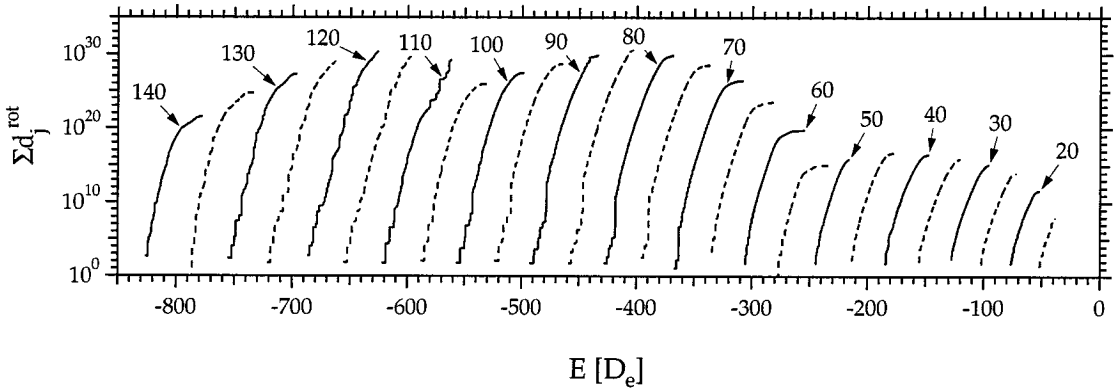

FIGURE 7 Cumulative number of isomers ($\sum_{E_j \leq E} d_j^{rot}$) as a function of binding energy (E) and number of particles (n). The summation was carried out for up to 6 holes ($h \leq 6$).

shown.) Up to six holes ($h \leq 6$) were used in generating these structures. Although a huge number of isomers are observed, the total falls far short of a simple extrapolation of the Tsai and Jordan results for $n \leq 13$.[25] As pointed out by Doye and Wales,[38] this observation suggests that there are additional isomers at higher energies but that these structures are not thermally accessible at reasonable temperatures.

In Sec. V, we argued that there are too many shell configurations to enumerate them all; however, it is conceivable that, in some cases, all of the bins of configurations were identified. This is possible since configurations with similar energies were binned together. Our sampling was sufficient to contain the minimum energy structures as reported by Northby[14] for the following ranges: $13 \leq n \leq 30$, $41 \leq n \leq 63$, and $140 \leq n \leq 147$. This suggests that most of the structures in these size ranges have been identified. In the intermediate ranges, there are simply too many structures to expect an undirected search to find most of the structures in the time available. Still, sampling is sufficient to represent the distribution of structures. Since only a small fraction of low energy structures seem to contribute to the configurational partition function, improved estimates for q_{config} could be obtained using the LGC method and an acceptance sampling Monte Carlo algorithm.

4.7 Discussion and Applications

Extrapolation to Bulk Properties

In a previous paper,[35] we showed that a quadratic fit to a plot of free energy per particle (F/n) versus $n^{-1/3}$ yields estimates for the bulk chemical potential (μ_o), bulk surface tension (σ_o), and Tolman length (δ).

$$\frac{F}{n} = \mu + \sigma_o(4\pi)^{1/3}(3v)^{2/3}n^{-1/3} - 2\sigma_o\delta(4\pi)^{2/3}(3v)^{1/3}n^{-2/3}. \tag{34}$$

The Tolman length gives the first correction to the surface tension (σ) due to the radius of curvature (r),

$$\sigma(r) = \sigma_o(1 - \frac{2\delta}{r}) + \mathrm{O}(r^{-2}). \tag{35}$$

The molecular volume (v) is assumed to be constant to be consistent with the assumed form for the partition function (4).

We calculated cluster free energies (F) using Eq. (5) and the following estimates (from a previous paper in this series[35]) for the binding energy (E^{min}),

$$E^{min}/(nD_e) = -8.610 + 15.744n^{-1/3} - 11.894n^{-2/3} + 17.194n^{-1} - 20.387n^{-4/3}, \tag{36}$$

the zero point energy (E^{zp}),

$$E^{zp} = \frac{h}{2}\sum_{i}^{3n-6}\nu_i, \tag{37}$$

$$E^{zp} \approx (3n-6)h\nu_{char}\left[10.287 - \frac{7.679}{N} + \frac{5.422}{N^2} - \frac{1.439}{N^3}\right], \tag{38}$$

the product of the principal moments of inertia ($I_AI_BI_C$),

$$(I_AI_BI_C)^{1/3} \approx I_{char}\sum_{y=1}^{N} y^2\left(10y^2+2\right)\left[0.4298 + \frac{0.0104}{N} + \frac{0.2457}{N^2} - \frac{0.0666}{N^3}\right], \tag{39}$$

and the vibrational free energy (F_{vib}).

$$F^{vib} = RT \sum_{i=1}^{3n-6} \ln \left[1 - \exp\left(-\frac{h\nu_i}{kT} \right) \right], \tag{40}$$

$$F^{vib} \approx \xi RT(3n-6) \ln \left[1 - \exp\left(-\frac{\theta_E}{T} \right) \right], \tag{41}$$

$$\xi = \exp\left(\frac{\alpha(\theta_E - \theta_{min})}{T(T+\alpha)} \right), \tag{42}$$

$$\frac{\alpha}{T_{char}} = 1.05 + \frac{1.97}{N} - \frac{1.88}{N^2} + \frac{0.47}{N^3}, \tag{43}$$

$$\frac{\theta_E}{T_{char}} = 19.27 - \frac{16.95}{N} + \frac{15.42}{N^2} - \frac{5.40}{N^3}, \tag{44}$$

$$\frac{\theta_{min}}{T_{char}} = 0 + \frac{17.16}{N} - \frac{14.49}{N^2} + \frac{4.67}{N^3}. \tag{45}$$

Planck's constant (h) in Eqs. (37), (38), and (40) should not be confused with the number of holes in a cluster. The binding energy estimate Eq. (36) is based on minimum energy structures for large clusters.[40] We use it to estimate bulk properties. For smaller clusters, ($n \leq 147$) tabulated values were used.[14] The characteristic values ν_{char}, I_{char}, and T_{char} are defined and tabulated for four noble gases in Table IV. Although Eqs. (38), (39), and (43)-(45) were based on magic-numbered clusters,[35] we have used Eqs. (38) and (43)-(45) as interpolating functions by inverting (1) to give values for N for clusters containing arbitrary numbers of particles (n) and have used a linear interpolation in Eq. (39).

Figure 8 shows polynomial fits to the free energy of argon clusters at several temperatures as motivated by Eq. (34). Also shown are the asymptotic polynomials which were used to determine bulk properties. Note that translation and rotation contribute terms of order $ln(n)/n$, which are negligible in the large n limit. Table VIII summarizes the estimated bulk properties of four noble gases and Table IX gives polynomial fits to the cluster free energies for use by the reader. (Tables of cluster free energy as a function of temperature and cluster size are too extensive to publish.)

TABLE VIII The bulk chemical potential (μ), surface tension (σ), and Tolman length (δ) for the solid form of four noble gases, estimated using Eq. (34) and asymptotic analysis on Eqs. (36)-(45). For the 0 K evaluations, the temperature-dependent contributions to the free energy were set to zero.

Solid	T (K)	μ $\left(\frac{kcal/mol}{particle}\right)$	σ $\left(\frac{dyn}{cm}\right)$	δ $\left(\mathring{A}\right)$
Ne	0	-0.448	17.2	0.74
	10	-0.449	17.0	0.74
Ar	0	-1.852	45.2	0.81
	10	-1.853	45.1	0.81
	20	-1.861	44.5	0.82
	30	-1.884	43.8	0.83
	40	-1.920	42.8	0.84
	50	-1.967	41.7	0.85
Kr	0	-2.653	56.3	0.85
	10	-2.655	56.1	0.85
	20	-2.670	55.5	0.85
	30	-2.703	54.7	0.86
	40	-2.751	53.9	0.87
	50	-2.813	52.9	0.89
	60	-2.886	51.9	0.90
	70	-2.967	50.8	0.90
Xe	0	-3.695	66.3	0.92
	10	-3.697	66.1	0.92
	20	-3.717	65.5	0.92
	30	-3.756	64.8	0.93
	40	-3.813	64.1	0.94
	50	-3.882	63.3	0.94
	60	-3.962	62.5	0.95
	70	-4.054	61.7	0.96
	80	-4.152	60.8	0.97
	90	-4.258	59.8	0.98
	100	-4.371	58.7	0.99

TABLE IX Free energy per particle based on quadratic fits as in Figure 8. This data is provided as a concise summary of the cluster free energies which are used in Sec. VII, but are too exhaustive to reproduce.

Solid	T (K)	F/n $\left(\frac{kcal/mol}{particle}\right)$
Ne	0	$-0.448 + 0.951n^{-1/3} - 0.546n^{-2/3}$
	10	$-0.449 + 0.961n^{-1/3} - 0.751n^{-2/3}$
Ar	0	$-1.850 + 3.529n^{-1/3} - 1.804n^{-2/3}$
	10	$-1.850 + 3.544n^{-1/3} - 2.037n^{-2/3}$
	20	$-1.859 + 3.534n^{-1/3} - 2.295n^{-2/3}$
	30	$-1.882 + 3.503n^{-1/3} - 2.548n^{-2/3}$
	40	$-1.917 + 3.461n^{-1/3} - 2.800n^{-2/3}$
	50	$-1.965 + 3.412n^{-1/3} - 3.053n^{-2/3}$
Kr	0	$-2.653 + 4.967n^{-1/3} - 2.480n^{-2/3}$
	10	$-2.655 + 4.982n^{-1/3} - 2.735n^{-2/3}$
	20	$-2.670 + 4.961n^{-1/3} - 3.000n^{-2/3}$
	30	$-2.703 + 4.922n^{-1/3} - 3.254n^{-2/3}$
	40	$-2.751 + 4.874n^{-1/3} - 3.502n^{-2/3}$
	50	$-2.813 + 4.824n^{-1/3} - 3.753n^{-2/3}$
	60	$-2.885 + 4.770n^{-1/3} - 4.005n^{-2/3}$
	70	$-2.967 + 4.712n^{-1/3} - 4.255n^{-2/3}$
Xe	0	$-3.715 + 6.898n^{-1/3} - 3.408n^{-2/3}$
	10	$-3.717 + 6.911n^{-1/3} - 3.677n^{-2/3}$
	20	$-3.737 + 6.886n^{-1/3} - 3.948n^{-2/3}$
	30	$-3.776 + 6.844n^{-1/3} - 4.206n^{-2/3}$
	40	$-3.833 + 6.794n^{-1/3} - 4.458n^{-2/3}$
	50	$-3.902 + 6.742n^{-1/3} - 4.707n^{-2/3}$
	60	$-3.983 + 6.688n^{-1/3} - 4.954n^{-2/3}$
	70	$-4.074 + 6.632n^{-1/3} - 5.200n^{-2/3}$
	80	$-4.172 + 6.575n^{-1/3} - 5.450n^{-2/3}$
	90	$-4.278 + 6.516n^{-1/3} - 5.698n^{-2/3}$
	100	$-4.391 + 6.455n^{-1/3} - 5.950n^{-2/3}$

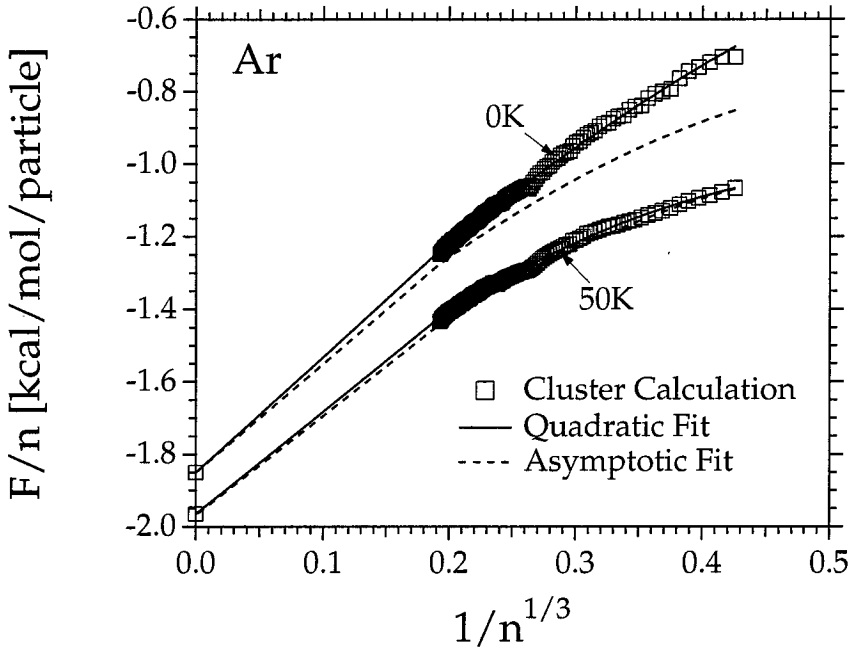

FIGURE 8 Calculated free energy per particle vs $n^{-1/3}$ for argon as motivated by Eq. (34). The intercept is the bulk chemical potential, the slope at the origin is proportional to the surface tension, and the curvature is related to the Tolman length.

Since the bulk properties listed in Table VIII were not used to determine the parameters in the atomic potential,[36] they can be used to check the potential. The chemical potential relative to the ideal gas at 0 K and zero pressure is related to the vapor pressure as follows:[30]

$$P^{vap} = \frac{(2\pi m)^{3/2}(kT)^{5/2}}{h^3} \exp\left(\mu/kT\right). \tag{46}$$

We compare vapor pressures calculated using the estimated bulk chemical potential (Table VIII) with experimental data[41,42] in Figure 9. The agreement is excellent up to about 60% of the normal boiling point. We overestimate the vapor pressure at the boiling point by about 30%, probably due to the harmonic approximation that tends to underestimate the entropy of the solid at elevated temperatures.

Figures 10 and 11 compare the calculated surface tension and Tolman length with the available data.[43–45] Based on these comparisons with experimental data, we are confident in applying SLS/LGC to noble gas clusters up to 60% of the normal boiling

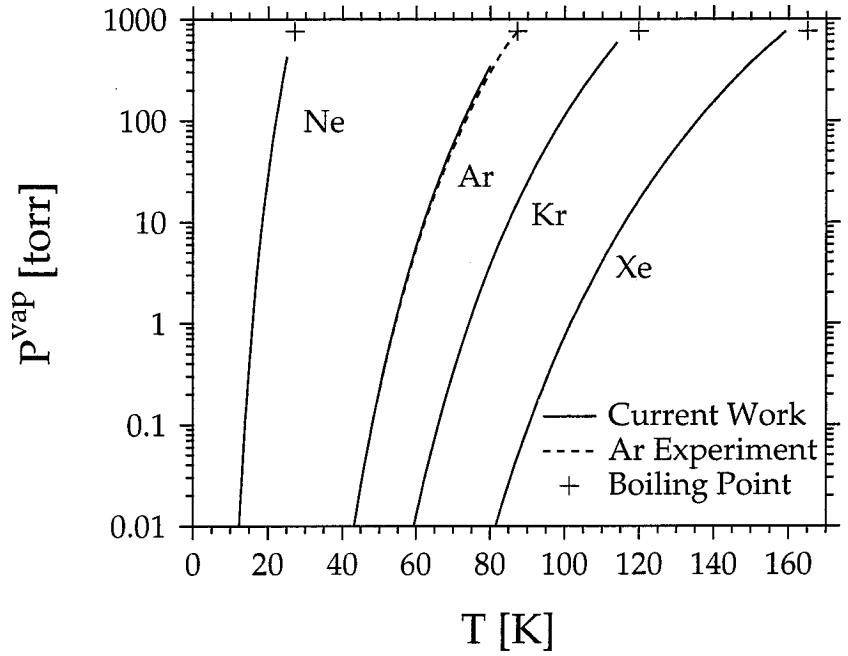

FIGURE 9 Calculated vapor pressure for four noble gases. Also shown are the normal boiling points[41] and the experimental vapor pressure for Argon.[42] The slight deviations near the boiling points are the result of anharmonicity of the vibrational modes.

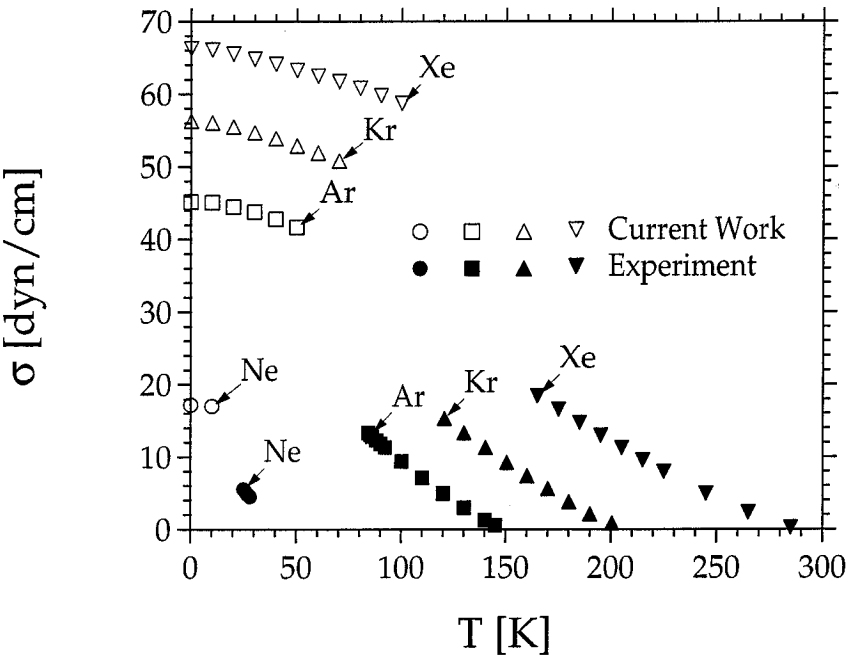

FIGURE 10 Calculated and experimental[43,44] surface tension for four noble gases.

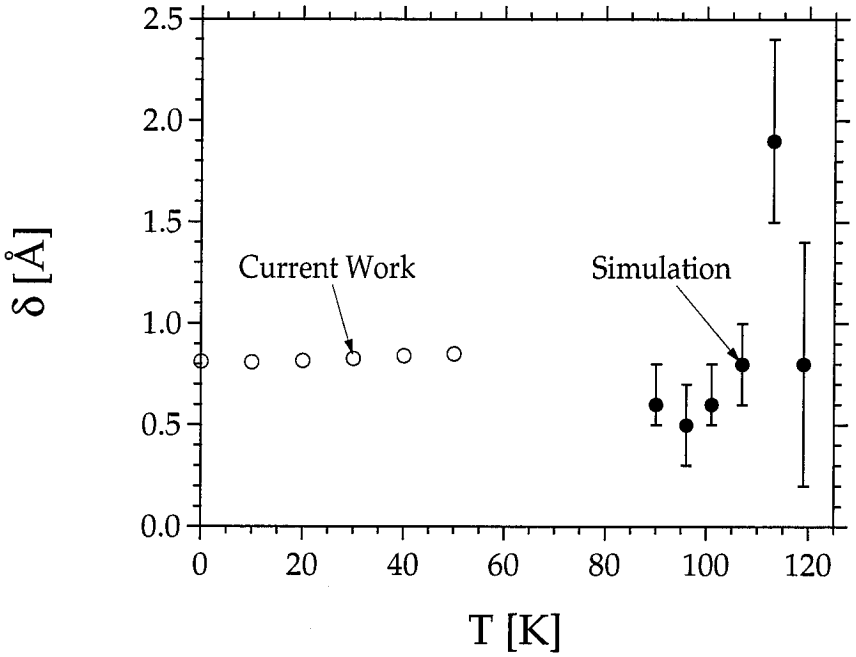

FIGURE 11 Calculated and simulated[45] Tolman length for Argon. The error bars on the simulation results are $\pm 1\sigma$.

point.

Homogeneous Nucleation Rates

As a further application of SLS/LGC, we will use the thermodynamic data in Table VII and the cluster free energies calculated using Eq. (5) to predict the flux of nuclei J from a super-saturated vapor. According to classical theory,[46,47] the flux (J_n) of clusters through a size (n) is

$$J_n = \alpha_n \beta A_n C_n - E_{n+1} C_{n+1}, \tag{47}$$

where α_n is the accommodation coefficient (commonly assumed to be unity), β is the flux of monomers through a unit area, A_n is the surface area of the cluster, C_n is the number concentration, and E_n is the frequency of monomer evaporation from an n-mer. To determine E_n, we follow the approach of Katz.[47] Applying detailed

balancing at full thermodynamic equilibrium yields

$$J_n^{eq} = 0 = \alpha_n \beta^{eq} A_n C_n^{eq} - E_{n+1}^{eq} C_{n+1}^{eq}. \tag{48}$$

Assuming that the evaporation rate is independent of the vapor conditions leads to the following estimate for E_{n+1}.

$$E_{n+1} = \alpha_n \beta^{eq} A_n C_n^{eq} / C_{n+1}^{eq}. \tag{49}$$

Substituting Eq. (49) into Eq. (47),

$$J_n = \alpha_n \beta A_n C_n^{eq} \left[\frac{C_n}{C_n^{eq}} - \frac{\beta^{eq} C_{n+1}}{\beta C_{n+1}^{eq}} \right], \tag{50}$$

multiplying and dividing by $(\beta^{eq}/\beta)^n$, and rearranging gives

$$\frac{J_n}{\alpha_n \beta A_n C_n^{eq} (\beta/\beta^{eq})^n} = \frac{C_n}{C_n^{eq}} \left(\frac{\beta^{eq}}{\beta} \right)^n - \frac{C_{n+1}}{C_{n+1}^{eq}} \left(\frac{\beta^{eq}}{\beta} \right)^{n+1}. \tag{51}$$

For steady state nucleation, $J_1 = J_2 = ... = J_n = J$. Summing Eq. (51) over n yields

$$J \sum_{n=1}^{b} \frac{1}{\alpha_n \beta A_n C_n^{eq} (\beta/\beta^{eq})^n} = \frac{C_1}{C_1^{eq}} \left(\frac{\beta^{eq}}{\beta} \right) - \frac{C_{b+1}}{C_{b+1}^{eq}} \left(\frac{\beta^{eq}}{\beta} \right)^{b+1}. \tag{52}$$

From the kinetic theory of gases,

$$\beta = P/(2\pi m k T)^{1/2}, \tag{53}$$

$$\beta/\beta^{eq} = P/P^{vap} = C_1/C_1^{eq} = S, \tag{54}$$

where P is the monomer pressure and S is the saturation ratio. By the law of mass action,

$$C_n^{eq} = C_1^{eq} \exp(-\Delta G_n/kT), \tag{55}$$

$$\Delta G_n = F_n - n\mu_{bulk}. \tag{56}$$

Finally, using Eqs. (54) and (55) and allowing b to become large gives the desired form for the nucleation rate.

$$J = \beta / \sum_{n=1}^{\infty} \left[\alpha_n A_n C_1^{eq} \exp\left(n \ln S - \Delta G_n / kT\right)\right]^{-1}. \tag{57}$$

We use the molar volume (v) to estimate the cluster surface area,

$$A_n = (4\pi)^{\frac{1}{3}} (3nv)^{\frac{2}{3}}. \tag{58}$$

When evaluating ΔG_n, it is common to assume that the bulk surface tension applies to the cluster. This is the capillarity approximation,

$$\Delta G_n^{cap} = \sigma_o A_n, \tag{59}$$

Previous workers[48,49] have compared nucleation rates for argon based on cluster calculations with rates based on the capillarity approximation. Hoare, Pal, and Wegener[48] performed calculations using only the minimum energy structure for each cluster which limits the results to the purely solidlike (low temperature) limit. Garcia and Torroja[49] used a purely classical calculation scheme which neglects zero-point energy contributions to the cluster energy. In both studies, it was unclear whether the comparison tested the capillarity approximation, the model potential used for the cluster calculations, or the simplifying assumptions employed.

We use the extrapolations discussed above to make an internally consistent test of the effect of the capillarity approximation since both our cluster calculations and our estimated bulk properties are based on the same model potential. Furthermore, we verified the model potential using vapor pressure, surface tension, and Tolman length predictions. (See Sec. VII A.) The most limiting assumption used in our calculation of the free energy (5) is the harmonic approximation for the vibrational modes. As stated earlier, this approximation is justified up to about $0.6T_b$. Therefore, we are able to make definitive tests of the capillarity approximation.

Figure 12 shows that the nucleation rate of argon as estimated using cluster calcu-

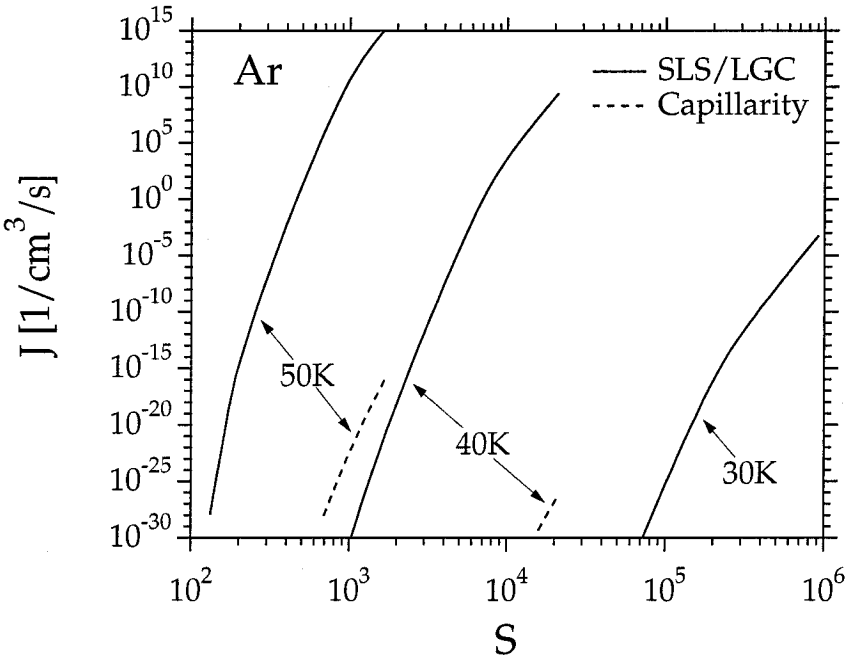

FIGURE 12 Nucleation rate (J) as a function of saturation ratio ($S = P/P^{vap}$) for argon. The dotted lines are based on the capillarity approximation using the surface tension extrapolated from the clusters calculations. Therefore, this is an internally consistent test of the capillarity approximation. We find that the capillarity approximation leads to an underestimate of the nucleation rate by $O(10^{30})$ at 50 K and by $O(10^{35})$ at 40 K.

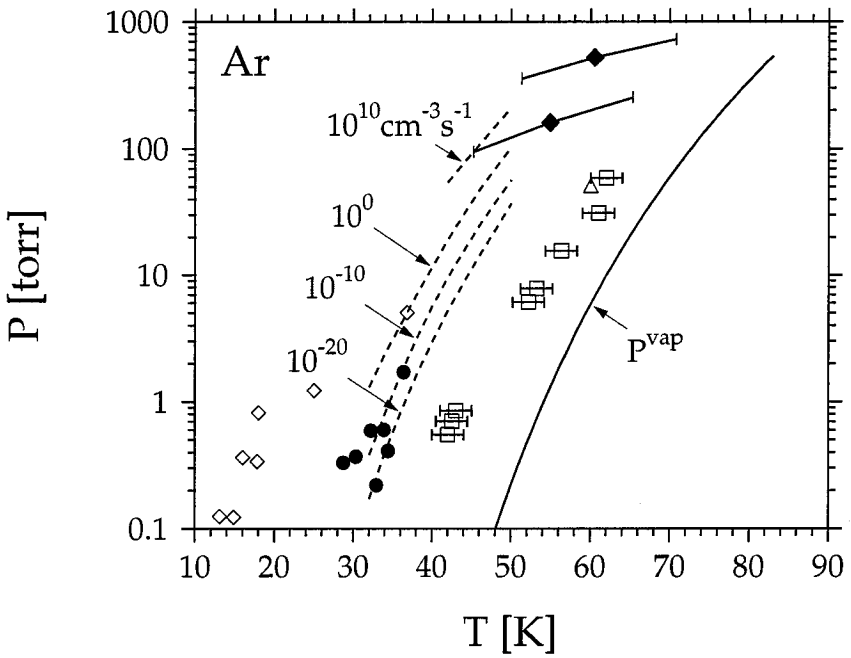

FIGURE 13 Nucleation rate (J) as a function of temperature and pressure for argon. The lines are loci of constant nucleation rate ($events/cm^3/s$) based on the current work. The symbols are experimental determinations of the onset of nucleation [50–54] as determined by: (◆) Pierce *et al.* (1971), (◇) Lewis and Williams (1974), (△) Stein (1974), (•) Wu *et al.* (1978), and (□) Steinwandel and Buchholz (1984).

lations is 30 orders of magnitude faster than the capillarity estimate. The discrepancy decreases somewhat with increased temperature.

Despite the discontinuities in the free energy as a function of cluster size (Figure 8), the nucleation rate is a smooth function of saturation ratio (S). (See Figure 12.) This is because the nucleation rate is determined by a summation of terms along a path through cluster space. Although the individual terms are not smooth with respect to their neighbors, each varies smoothly with S. Therefore, the path sum (nucleation rate) is a smooth function of S even though the path is a discontinuous function of cluster size. Since the details of the cluster free energy function are not reflected in the nucleation rate, subsequent modeling studies will be able to concentrate on a few cluster sizes and interpolate the data. This will be a huge savings in effort compared to the exhaustive work presented here.

Figures 13 and 14 depict loci of constant nucleation rate as a function of temperature and partial pressure for four noble gases. These curves are bounded due to the

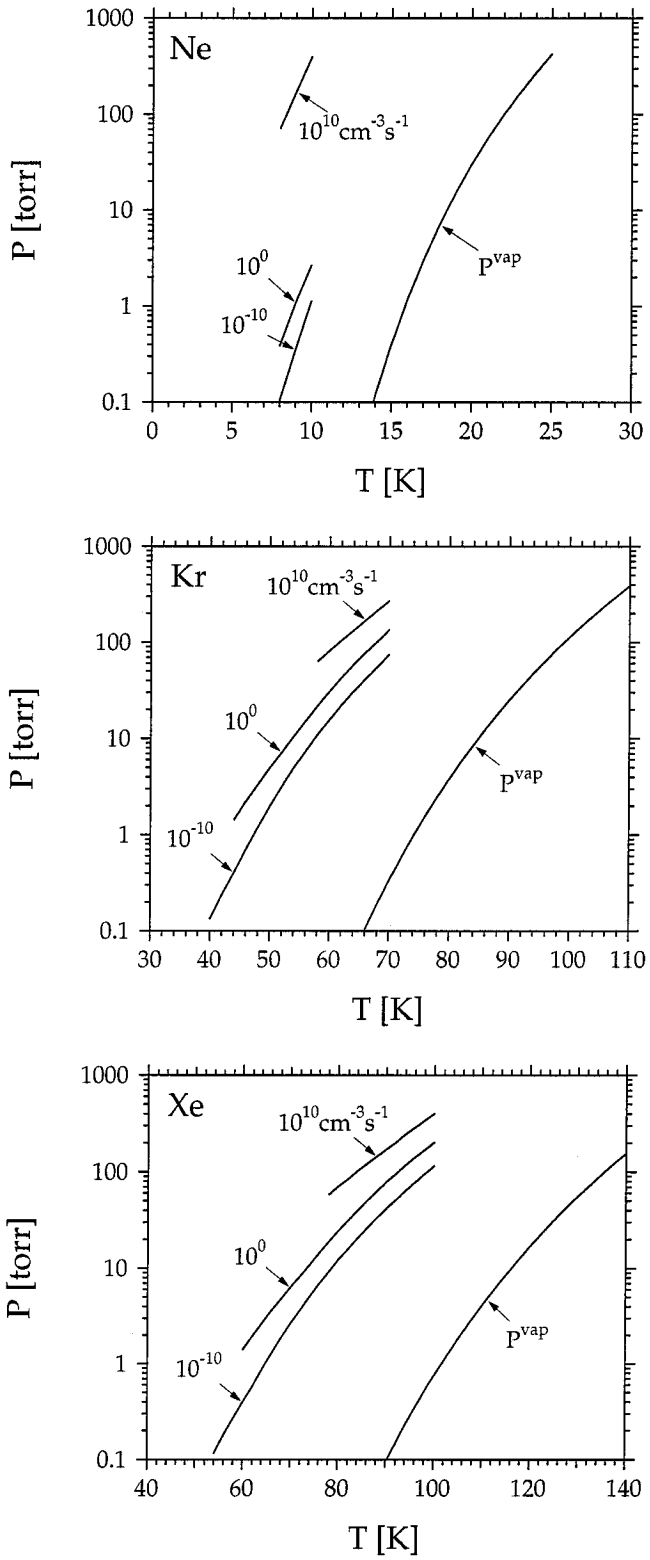

FIGURE 14 Nucleation rate (J) as a function of temperature and pressure for three noble gases as in Figure 13.

limit of applicability of the model ($T \leq 0.6T_b$) and the range of cluster sizes studied. In order to avoid truncation errors, we only report nucleation rates based on (57) if the summation is dominated by clusters of 17 to 135 atoms. The equilibrium vapor pressure curve calculated using Eq. (46) is also shown in Figures 13 and 14. The nucleation rate vanishes at the equilibrium curve.

Previous calculations for argon[48,49] yielded somewhat higher rates. Most of the discrepancy is due to the use of a formula that is larger than Eq. (57) by a factor of S. It is now commonly accepted that Eq. (57) is the correct form.[46]

The available data for argon nucleation, reproduced in Figure 13, is based on onset determinations.[50–54] Several researchers determined a locus of points that mark the detection limit of nucleation for their apparatus. A given researcher's detection limit should be relatively insensitive to operating conditions, so each data set in Figure 13 should follow one of our curves of constant nucleation rate. Since none of them report estimates of their detection limit, only qualitative comparisons are possible. The data by Pierce *et al.*[50] and Wu *et al.*[53] are generally consistent with our calculations. Error bars on Pierce's data are the author's. Wu's data center on our curve for 10^{-10} $cm^{-3}s^{-1}$ with a scatter of $\pm 3K$, suggesting the experimental uncertainty in those trials. Calculated nucleation rates in this temperature range differ by 10 orders of magnitude. Realistic detection limits for nucleation in jets are $O(10^{10})$. The data by Stein[52] and by Steinwandel and Buchholz[54] is too near the saturation curve to be consistent with the current results. (This would imply a sensitivity of roughly 10^{-40} $cm^{-3}s^{-1}$.) The error bars on the latter data set are estimated from Figure 5 in Ref. 54. Lewis and William's data[51] imply enormous saturation ratios which seem unlikely in light of this work.

Detailed comparisons with experiments awaits quantitative nucleation rate measurements for noble gas vapors. Previous experiments have used argon because it is inexpensive and available in very high purity. However, argon has the disadvantage of requiring extremely low temperatures to initiate nucleation. Figures 14(a) and 14(b) show that neon and krypton also require extreme conditions. Future experiments may benefit from the more accessible range of pressures and temperatures appropri-

ate for xenon as depicted in Figure 14(c). We predict reasonable nucleation rates for xenon vapor at a few tens of torr at liquid nitrogen temperature (77 K). At these conditions, it should be possible to use a fixed volume apparatus rather than the continuous flow methods used previously for argon. (See Ref. 55 for brief descriptions of various nucleation apparatus.) Using a fixed volume would offset the higher cost of xenon. Quantitative nucleation rate measurements for xenon would be invaluable in guiding theoretical work in nucleation theory.

4.8 Acknowledgments

We thank Jon Doye and Prof. D. J. Wales for providing the data from their prior work (Ref. 38) which we have included in Figure 5. RBM acknowledges a National Science Foundation Graduate Research Fellowship. Partial support of the work was provided by grants from the NSF (CHE 94-13930, CTS 91-13191, and ASC 92-17368) and from the International Fine Particle Research Institute. Portions of this research were performed using the Intel Delta System operated by Caltech on behalf of the Concurrent Supercomputing Consortium. We thank Donald Dabdub for his expertise in preparing our code for the Delta System and for handling the scheduling of the runs. The facilities of the MSC are also supported by grants from DOE-BCTR, Allied-Signal Corp., Asahi Chemical, Asahi Glass, Chevron Petroleum Technology Co., Chevron Research Technology Co., Hughes Research Laboratories, and Beckman Institute.

4.9 Appendix

As noted above, Eq. (12) overestimates the number of distinct isomers due to the inclusion of rotationally equivalent configurations. Similarly, the number of distinguishable rotational states (q_{rot}) should be reduced to account for the rotational symmetry of the isomers. Both issues can be addressed simultaneously with the aid of group theory.

We follow the notation of Wigner.[56] Script capital letters represent groups of symmetry operations and lowercase letters are integers. Let $\mathcal{A}$ be the group of proper rotations of a dense icosahedral core and let $\mathcal{B}$ be the group of proper rotations of a shell built around that core. By definition,[41] the symmetry numbers of the dense core and shell (σ_c and σ_s) are the orders of $\mathcal{A}$ and $\mathcal{B}$, respectively.

CASE 1: Dense core, coincident centers of symmetry

For a dense core, the group of proper rotations is I and $\sigma_c = 60$. The center of symmetry of the core coincides with the atom at the center of the core. In the vast majority of clusters, this atom is unique and must therefore lie at the center of symmetry of the full cluster. (The exceptions are addressed below.) For coincident centers of symmetry, it can be shown[56] that $\mathcal{B}$ and its $(l-1)$ distinct cosets each have the same order (σ_s) and together span the σ_c elements of $\mathcal{A}$ without repeated elements. Simple accounting of elements leads to

$$\sigma_c = \sigma_s l. \tag{A1}$$

Once an orientation for the shell is chosen, the $(l-1)$ rotationally equivalent configurations can be identified in a one-to-one manner with the $(l-1)$ distinct cosets. Therefore, l can be replaced by d^{rot}

$$\frac{1}{\sigma_s} = \frac{d^{rot}}{60}. \tag{A2}$$

The degeneracies (d^{rot}) calculated in Sec. 4 are for one or more isomers of similar energies. Due to the distributive property of division over addition, binning of isomers does not change the result of Eq. (A2).

$$\frac{1}{60}\sum_j d_j^{rot} \exp(\frac{-\Delta E_j}{RT}) = \sum_j \left(\frac{d_j}{\sigma_j}\right) \exp(\frac{-\Delta E_j}{RT}), \tag{A3}$$

$$\frac{d_j}{\sigma_j} = \frac{d_j^{rot}}{60}. \tag{A4}$$

CASE 2: Dense core, non-coincident centers of symmetry

In polyicosahedral (PIC) clusters,[57] the structure consists of two or more interpenetrating icosahedra. For PIC clusters with an even number of icosahedra, the center of symmetry does not necessarily coincide with the center of symmetry of any of the icosahedra considered separately. Therefore, for a few very special structures, there is no unambiguous choice for the core of the cluster. Then, the analysis of Case 1 does not hold because $\mathcal{A}$ and $\mathcal{B}$ are not groups of symmetry operations with respect to the same center.

An example will help illustrate the situation. The 19-atom PIC structure, which has D_{5h} symmetry, consists of two interpenetrating icosahedra. The center of one icosahedron is a vertex of the other (and *vice versa*) and they share five other vertex atoms. The center of symmetry of the cluster is midway between the centers of symmetry of the icosahedra considered separately. Therefore, neither of the icosahedra can be unambiguously labeled the core. For this structure, Eq. (A2) underestimates σ_s by a factor of two.

Fortunately, the 19-atom PIC structure is the only structure which has both an ambiguous core assignment and a favorable binding energy. The other PIC structures presented by Farges *et al.*[57] have centers of symmetry which are coincident with the center of symmetry of one of its constituent icosahedra. One can construct other PIC structures with ambiguous core assignments, but none of them have large enough binding energies to contribute significantly to q_{config} due to the Boltzmann weighting in Eq. (6). Therefore, we consider the 19-atom PIC structure as a special case and neglect the error in the estimates of the symmetry numbers of other PIC structures with ambiguous core assignments.

CASE 3: Cores containing holes

For clusters containing holes, two (or more) shells lack some of the symmetry of the core before the promoted atoms left the core. The same argument used in Case 1 can be used here if $\mathcal{A}$ is defined as the group of proper rotations of the core before the promoted atoms left the core and $\mathcal{B}$ is defined as the group of proper rotations of the composite shell composed of all incomplete shells. Therefore, Eq. (A2) also

applies for clusters containing holes.

4.10 References

[1]D. Kashchiev, J. Chem. Phys. **76**, 5098 (1982); D. W. Oxtoby and D. Kashchiev, *ibid.* **100**, 7665 (1994).

[2]H. Haberland in *Clusters of Atoms and Molecules*, edited by H. Haberland, (Springer-Verlag, Berlin, 1994) pp208-223.

[3]J. Farges, M.F. DeFeraudy, B. Raoult, and G. Torchet, J. Phys. Colloq. **38**, C2-47 (1977); J. Chem. Phys. **78**, 5067 (1983); **84**, 3491 (1986).

[4]S. S. Kim and G. D. Stein, J. Colloid Int. Sci. **87**, 180 (1982).

[5]J. W. Lee and G. D. Stein, Surf. Sci. **156**, 112 (1985).

[6]B. Raoult, J. Farges, M. F. DeFeraudy, and G. Torchet, Philos. Mag. B. **60**, 881 (1989).

[7]U. Buck in Ref. 2, pp232-239.

[8]H. Haberland, Surf. Sci. **156**, 305 (1985).

[9]C. Brechignac, Ph. Cahuzac, J. Leygnier, R. Pflaum, and J. Weiner, Phys. Rev. Lett. **61**, 314 (1988).

[10]U. Buck and H. Meyer, J. Chem. Phys. **84**, 4854 (1986).

[11]U. Buck, Ber. Bunsenges. Phys. Chem. **96**, 1294 (1992).

[12]M. R. Hoare, Adv. Chem. Phys. **40**, 49 (1979), and references therein.

[13]J. Farges, M. F. DeFeraudy, B. Raoult, and G. Torchet, Adv. Chem. Phys. **70B**, 45 (1988), and references therein.

[14]J. A. Northby, J. Chem. Phys. **87**, 6166 (1987).

[15]J. A. Northby, J. Xie, D. L. Freeman, and J. D. Doll, Z. Phys. D. **12**, 69 (1989). J. Xie, J. A. Northby, D. L. Freeman, and J. D. Doll, J. Chem. Phys. **91**, 612 (1989).

[16]J. D. Honeycutt and H. C. Andersen, J. Phys. Chem. **91**, 4950 (1987).

[17]J. Jellinek, T. L. Beck, and R. S. Berry, J. Chem. Phys. **84**, 2783 (1986); T. L. Beck, J. Jellinek, and R. S. Berry, *ibid.* **87**, 545 (1987); T. L. Beck and R. S. Berry, *ibid.* **88**, 3910 (1988); R. S. Berry, Z. Phys. D **12**, 161 (1989).

[18]H. P. Cheng and R. S. Berry, Phys. Rev. A **45**, 7969 (1992).

[19]H. L. Davis, J. Jellinek, and R. S. Berry, J. Chem. Phys. **86**, 6456 (1987).

[20]R. D. Etters and R. Danilowicz, J. Chem. Phys. **71**, 4767 (1979).

[21]V. V. Nauchitel and A. J. Pertsin, Mol. Phys. **40**, 1341 (1980).

[22]N. Quirke and P. Sheng, Chem. Phys. Lett. **110**, 63 (1984).

[23]D. L. Freeman and J. D. Doll, Adv. Chem. Phys. **70B**, 139 (1988).

[24]H. P. Cheng, X. Li, R. L. Whetten, and R. S. Berry, Phys. Rev. A **46**, 791 (1992).

[25]C. J. Tsai and K. D. Jordan, J. Phys. Chem. **97**, 11227 (1993).

[26]R. S. Berry, J. Chem. Soc. Faraday Trans. **86**, 2343 (1990).

[27]A. L. Mackay, Acta Cryst. **15**, 916 (1962).

[28]R. F. K. Herzog, W. P. Poschenrieder, and F. G. Satkiewicz, Radiat. Effects **18**, 199 (1973).

[29]F. H. Stillinger and T. A. Weber, Phys. Rev. A **28**, 2408 (1983).

[30]T. L. Hill, *Statistical Thermodynamics* (Dover, New York, 1986), pp104, 161-167.

[31]F. H. Stillinger and T. A. Weber, J. Chem. Phys. **81**, 5095 (1984).

[32]G. J. Hahn and W. Q. Meeker, *Statistical Intervals* (Wiley, New York, 1991), pp104-107.

[33]The Touchstone Delta System is a massively parallel computer with 520 Intel i860 computational processors operated by Caltech on behalf of the Concurrent Supercomputing Consortium.

[34]S. J. Kline and F. A. McClintock, Mech. Eng. **75**, 3 (1953).

[35]R. B. McClurg, R. C. Flagan, and W. A. Goddard, III, J. Chem. Phys. **102**, 3322 (1995).

[36]The Lennard-Jones parameters used in this study were chosen to agree with the bulk lattice spacing [J. Donohue, *Structures of the Elements* (R. E. Krieger, Malabar, FL, 1982)] and the heat of vaporization at 0 K after correcting for zero point energy [R. Hultgren *et al.*, *Selected Values of the Thermodynamic Properties of the Elements* (American Soc for Metals, Metals Park, OH, 1973)]. The method used to calculate Lennard-Jones parameters from this information is detailed elsewhere [N. Karasawa and W. A. Goddard, III, J. Phys. Chem. **93**, 7320 (1989)].

[37]The coordinates of the atoms in minimized structures were determined using POLYGRAPH from Molecular Simulations Inc., Burlington, MA.

[38]J. P. K. Doye and D. J. Wales, J. Chem. Phys. **102**, 9659 (1995).

[39]J. P. K. Doye and D. J. Wales, J. Chem. Phys. **102**, 9673 (1995).

[40]K. T. Lim, S. Brunett, M. Iotov, R. B. McClurg, N. Vaidehi, S. Dasgupta, S. Taylor, and W. A. Goddard, J. Comp. Chem., (in press).

[41]P. Atkins, *Physical Chemistry,* 3^{rd} *ed.* (Freeman, New York, 1986), pp531,813.

[42]W. T. Ziegler, J. C. Mullins, and B. S. Kirk, Technical Report #2, Project #A-460, Contract #CST-7238, National Bureau of Standards, 1962.

[43]K. C. Nadler, J. A. Zollweg, W. B. Streett, and I. A. McLure, J. Colloid Interface Sci. **122**, 530 (1988).

[44]G. A. Cook, *Argon, Helium, and the Rare Gases* (Interscience, New York, 1961).

[45]M. J. Haye and C. Bruin, J. Chem. Phys. **100**, 556 (1994).

[46]D. W. Oxtoby, J. Phys. Condensed Matter. **4**, 7627 (1992).

[47]J. L. Katz, Pure Appl. Chem. **64**, 1661 (1992).

[48]M. R. Hoare, P. Pal, and P. P. Wegener, J. Colloid Interface Sci. **75**, 126 (1980).

[49]N. G. Garcia and J. M. S. Torroja, Phys. Rev. Lett. **47**, 186 (1981).

[50]T. Pierce, P. M. Sherman, and D. D. McBride, Astron. Acta **16**, 1 (1971).

[51]J. W. L. Lewis and W. D. Williams, "Argon Condensation in Free Jet Expansions," Report No. AEDC-TR-74-32, 1974; W. D. Williams and J. W. L. Lewis, Report No. AEDC-TR-76-67, 1976.

[52]G. D. Stein, Argon condensation in a supersonic nozzle, Report to ONR, available from Technical Information Service No. AD-A007357/7GI, 1974.

[53]B. J. C. Wu, P. P. Wegener, and G. D. Stein, J. Chem. Phys. **69**, 1776 (1978).

[54]J. Steinwandel and T. Buchholz, Aerosol Sci. Tech. **3**, 71 (1984).

[55]R. H. Heist and H. He, J. Phys. Chem. Ref. Data **23**, 781 (1994).

[56]E. Wigner, *Group Theory* (Academic Press, New York, 1959), pp58-61.

[57]J. Farges, M. F. DeFeraudy, B. Raoult, G. Torchet, Surf. Sci. **156**, 370 (1985).

Chapter 5 Mercury Vapor Nucleation

Influences of Binding Transitions on the Homogeneous Nucleation of Mercury

R. B. McClurg[†], R. C. Flagan[†], and W. A. Goddard, III[‡,*]

[†]Spalding Laboratory (210-41)

[‡]Materials and Process Simulation Center, Beckman Institute (139-74)

Division of Chemistry and Chemical Engineering

California Institute of Technology, Pasadena, California 91125

Abstract

Nucleation rates from supersaturated vapor are calculated for mercury. Previous measurements of nucleation rates using an upward thermal diffusion chamber demonstrated that critical supersaturations for Hg vapor are roughly three orders of magnitude lower than the predictions of the classical Becker-Doring-Zeldovich theory. [J. Martens, H. Uchtmann, and F. Hensel, J. Phys. Chem. **91**, 2489 (1987)] This discrepancy was attributed to a metal-nonmetal transition in Hg clusters that occurs near the critical cluster size. [H. Uchtmann, K. Rademann, and F. Hensel, Annalen der Physik. **48**, 207 (1991)] That view is supported by the similarity of cohesive energies and optical spectra for Hg clusters and rare gas clusters. [H. Haberland *et al.*, Z. Phys. D **26**, 8 (1993)] Using this analogy and the framework of the classical theory, we calculate nucleation rates that agree with the experiments within experimental uncertainties without any adjustable parameters.

5.1 Introduction

Syntheses of nanostructured materials often involve spontaneous nucleation from a supersaturated phase followed by growth, agglomeration, coarsening, and/or ripening. The relative rates of these processes determine the product morphology and size distribution. Since unique properties of nanostructured materials derive from their structure, quantitative predictions of the kinetics of these processes are essential for a design and understanding of processing/structure/property/performance relations. In this paper, we illustrate the application of simple models to make quantitative rate predictions.

Although mercury is not a standard in nanomaterials circles, it will serve to illustrate our techniques and there is a wealth of literature describing its properties. Small mercury clusters ($n \leq 13$) are largely bound by van der Waals interactions while larger clusters ($n > 13$) are dominated by covalent interactions.[1–4] Evidence for this transition comes from photoionization,[1] 5d $\rightarrow$ 6p auto-ionizing spectroscopy,[2] and electron-impact ionization.[3] Bennemann *et al.* [4] published a theory for this bond character transition that agrees well with experimental cohesive energies up to $n = 19$. The cohesive energy is the potential energy of the cluster at 0K. It is a large contributor to the cluster free energy up to the boiling point. At $n = 13$, their theory predicts a discontinuous first derivative of cohesive energy versus cluster size. Experimental values demonstrating that discontinuity are reproduced in Fig. 1. In this paper, we explore the implications of this discontinuity on the rate of nucleation of a condensed phase from a supersaturated vapor.

We will treat clusters on each side of this transition as if they were different "phases." Then we can write the free energy of each phase as an expansion about its bulk properties. We will truncate the series after three terms.[5]

$$G_n = n\mu_p + A_n\sigma_p\left(1 - \frac{2\delta_p}{r_n} + O(r_n^{-2})\right) \qquad (1)$$

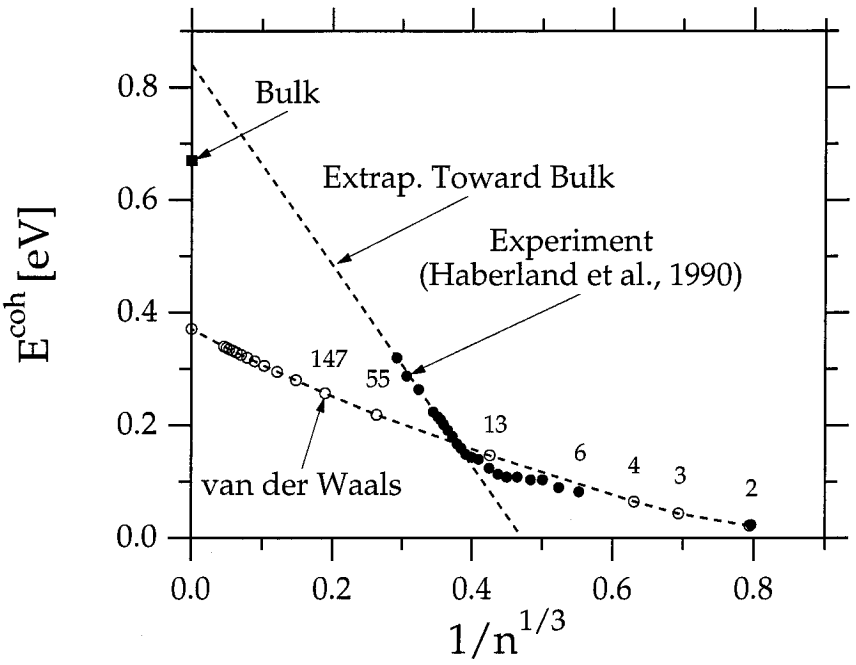

FIGURE 1 Cohesive energy E^{coh} versus cluster size n plot showing the discontinuous first derivative near $n = 13$.

$$p = \begin{cases} \text{vdW} & \text{for n} \leq 13 \\ \text{covalent} & \text{for n} > 13 \\ \text{metallic} & \text{for n} \to \infty \end{cases}$$

Thus, the chemical potential μ_p, surface tension σ_p, and Tolman length δ_p are (piecewise continuous) functions of the number of atoms in the cluster n or equivalently, the radius of the cluster r_n. This differential approach allows for a size-dependent "bulk" chemical potential unlike the typical analysis which lumps all of the size dependence in the surface energy terms.[6]

The outline of the balance of our paper is as follows. We review the classical theory of nucleation in Section 5.2. In Section 5.3, we use that framework to show that, over a broad range of conditions, the rate-limiting step in nucleation is the formation of 13 atom clusters. The available experimental data is consistent with this interpretation. In Section 5.5, we make quantitative predictions based on the classical nucleation theory and a simple model for Hg cluster properties, which is detailed in Section 5.4. The agreement with experimental results is excellent.

5.2 Classical Nucleation Theory

According to classical theory,[7,8] the flux (J_n) of clusters through a size (n) is

$$J_n = \alpha_n \beta A_n C_n - E_{n+1} C_{n+1} \tag{2}$$

where α_n is the accommodation coefficient (commonly assumed to be unity), β is the flux of monomers through a unit area, A_n is the surface area of the cluster, C_n is the number concentration, and E_n is the frequency of monomer evaporation from an n-mer. To determine E_n, we follow the approach of Katz.[8] Applying detailed balancing at full thermodynamic equilibrium yields

$$J_n^{eq} = 0 = \alpha_n \beta^{eq} A_n C_n^{eq} - E_{n+1}^{eq} C_{n+1}^{eq}. \tag{3}$$

Assuming that the evaporation rate is independent of the saturation ratio, i.e. $E_{n+1} = E_{n+1}^{eq}$, leads to the following estimate for E_{n+1}.

$$E_{n+1} = \alpha_n \beta^{eq} A_n C_n^{eq} / C_{n+1}^{eq} \tag{4}$$

Substituting Eq. (4) into Eq. (2),

$$J_n = \alpha_n \beta A_n C_n^{eq} \left[\frac{C_n}{C_n^{eq}} - \frac{\beta^{eq} C_{n+1}}{\beta C_{n+1}^{eq}} \right] \tag{5}$$

multiplying and dividing by $(\beta^{eq}/\beta)^n$, and rearranging gives

$$\frac{J_n}{\alpha_n \beta A_n C_n^{eq} (\beta/\beta^{eq})^n} = \frac{C_n}{C_n^{eq}} \left(\frac{\beta^{eq}}{\beta} \right)^n - \frac{C_{n+1}}{C_{n+1}^{eq}} \left(\frac{\beta^{eq}}{\beta} \right)^{n+1}. \tag{6}$$

For steady state nucleation, $J_1 = J_2 = ... = J_b = J$. Summing Eq. (6) over n yields

$$J \sum_{n=1}^{b} \frac{1}{\alpha_n \beta A_n C_n^{eq} (\beta/\beta^{eq})^n} = \frac{C_1}{C_1^{eq}} \left(\frac{\beta^{eq}}{\beta} \right) - \frac{C_{b+1}}{C_{b+1}^{eq}} \left(\frac{\beta^{eq}}{\beta} \right)^{b+1}. \tag{7}$$

From the kinetic theory of gases,

$$\beta = P/(2\pi mkT)^{1/2} \tag{8}$$

$$\beta/\beta^{eq} = P/P^{vap} = C_1/C_1^{eq} = S \tag{9}$$

where P is the monomer pressure and S is the saturation ratio. By the law of mass action

$$C_n^{eq} = C_1^{eq} \exp(-\Delta G_n/kT) \tag{10}$$

$$\Delta G_n = G_n - n\mu_{bulk} \tag{11}$$

where G_n is the free energy of a cluster of n atoms and μ_{bulk} is the bulk chemical potential for the equilibrium phase of the bulk material, i.e. metallic mercury. Finally, using Eqs. (9) and (10) and allowing b to become large gives the desired form for the nucleation rate.

$$J = \beta / \sum_{n=1}^{\infty} \left[\alpha_n A_n C_1^{eq} \exp\left(n \ln S - \frac{\Delta G_n}{kT} \right) \right]^{-1} \tag{12}$$

5.3 Critical Size Determination

Substituting Eqs. (11) into Eq. (12) gives the nucleation rate (J) in terms of the cluster free energy (G_n).

$$J = \beta C_1^{eq} / \sum_{n=1}^{\infty} \left[\alpha_n A_n \exp\left(n \ln S + \frac{(n\mu_{bulk} - G_n)}{kT} \right) \right]^{-1} \tag{13}$$

Since the product ($\alpha_n A_n$) changes slowly with n, the relative magnitude of each term of the summation is determined largely by the argument of the exponential. The value of n that minimizes the argument is called the critical cluster size (n^*). Because G_n is not a smooth function of n, some care must be taken in determining n^*. For sufficiently low(high) saturation ratios, the critical cluster size will be larger(smaller) than 13 atoms and one can differentiate the argument with respect to n to find the

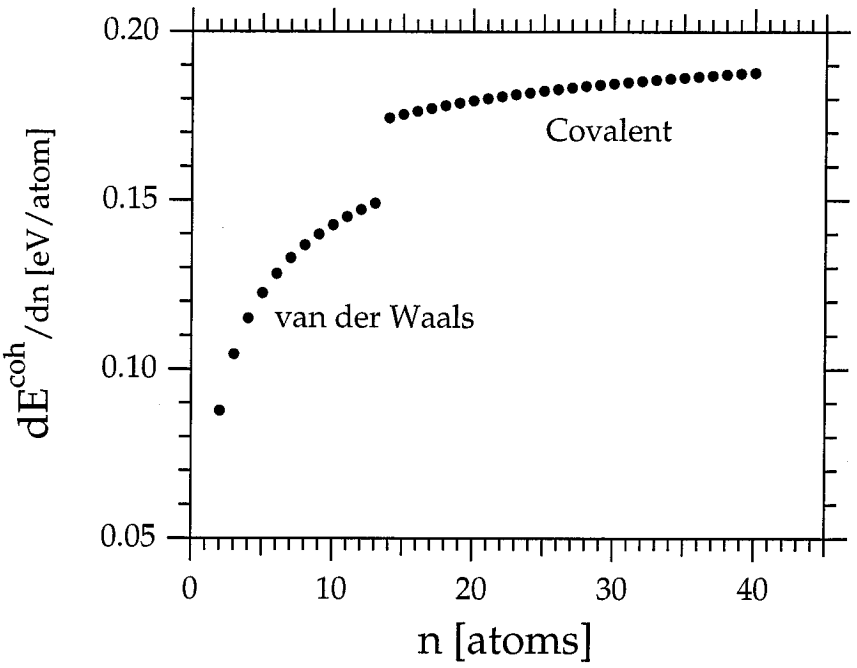

FIGURE 2 For a wide range of S, the critical size is 13 atoms due to the kink in E^{coh} (and G_n) at that size.

critical size. For a range of intermediate saturation ratios, the argument is minimized at the kink in G_n at $n = 13$. This is shown graphically in Fig. 2.

We define $S_l(S_h)$ as the lower(higher) saturation ratio such that the critical cluster size is 13 atoms. The size of the window defined by S_h/S_l can be estimated assuming that the other contributions to the free energy are smooth at $n = 13$.

$$S_h/S_l \approx \exp\left[\frac{-\left(dE^{coh}/dn\right)_{13^-} + \left(dE^{coh}/dn\right)_{13^+}}{kT}\right] \tag{14}$$

Fitting functions to the cohesive energy leads to

$$S_h/S_l \approx \exp\left(963K/T\right) \tag{15}$$

Therefore, at room temperature we expect a critical size of 13 atoms over a factor of 25 in saturation ratios. According to the nucleation theorem,[10,11] the nucleation rate is of the form

$$J = J_0 S^{(n^*+1)}. \tag{16}$$

Therefore, on a log-log plot, loci of nucleation rates (at a given temperature) as a function of the saturation ratio (S) should fall on a straight line of slope 14 over this range of S values. This is qualitatively consistent with experimental data.[12] We will make the comparison quantitative in the following sections.

5.4 Nucleation Rate Calculation

Since clusters in the covalent size range ($n > 13$) are much more strongly bound than in the van der Waals size range ($n \leq 13$), the terms in the summation of Eq. (13) after the 13th contribute negligibly to the sum for sufficiently large S values. We will truncate the sum after the 13th term. For the conditions discussed below, we estimate that this introduces an error of less than 1%. For ideal monatomic gas vapors, the chemical potential can be related to the vapor pressure as follows.[13]

$$\mu/kT = \ln\left(\frac{P^{vap}h^3}{(2\pi m)^{3/2}(kT)^{5/2}}\right) \tag{17}$$

Using this result in Eq. (13) gives

$$J = \beta C_1^{eq} / \sum_{n=1}^{13}\left[\alpha_n A_n S^n \left(\frac{P_{bulk}^{vap}}{P_{vdW}^{vap}}\right)^n \exp\left(\frac{-A_n\sigma_{vdW}}{kT}(1-2\delta_{vdW}/r_n)\right)\right]^{-1} \tag{18}$$

where β and C_1^{eq} are vapor properties, P_{vdW}^{vap}, σ_{vdW}, and δ_{vdW} are the bulk properties that mercury would have if it remained a van der Waals fluid up to bulk sizes, and P_{bulk}^{vap} is the vapor pressure of bulk (metallic) mercury. Next, we summarize our estimates of these material properties.

Vapor Properties

We will treat the vapor as an ideal gas. Then the equilibrium monomer concentration (C_1^{eq}) and the monomer flux (β) can be calculated from the ideal gas law and the kinetic theory of gases.

$$C_1^{eq} = P^{vap}/kT \tag{19}$$

$$\beta = P/(2\pi mkT)^{1/2} = SP^{vap}/(2\pi mkT)^{1/2} \tag{20}$$

van der Waals Properties

To model the vdW phase of Hg, we have used an effective Lennard-Jones potential.

$$\begin{aligned} \epsilon &= \rho^{-12} - 2\rho^{-6} \\ \epsilon &= E/D_e \\ \rho &= r/R_e \end{aligned} \tag{21}$$

Here E is the pairwise interaction energy and r is the distance between pairs of atoms in clusters of up to 13 atoms. The most recent experimental determination and *ab initio* calculation of the equilibrium distance for the dimer are 3.63 and 3.73Å, respectively.[14,15] Similarly, the dimer cohesive energy has been estimated at 0.043 and 0.047eV by experiment and theory.[16,15] The energy parameter D_e is larger than the cohesive energy due to the zero-point energy.

$$D_e = E^{coh} + \omega\hbar/2 \tag{22}$$

Here, ω is the dimer vibrational frequency which is approximately 19cm^{-1} for mercury.[14–16] To be consistent, we use the calculated values.

$$\begin{aligned} R_e &= 3.73\mathring{A} \pm 3\% \\ D_e &= 0.047eV \pm 3\% \\ m &= 200.59amu \end{aligned} \tag{23}$$

We use correlations from the literature to estimate P^{vap}_{vdW}, σ_{vdW}, and δ_{vdW} given the Lennard-Jones potential.[17–19] In addition, we estimate the sublimation pressure using the Classius-Clapeyron equation, and we assume that the solid surface tension is constant at its triple point value.

Metallic Properties

The only metallic Hg property that appears in Eq. 18 is the bulk vapor pressure. We should point out that this can be eliminated since

$$S^n \left(\frac{P_{bulk}^{vap}}{P_{vdW}^{vap}} \right)^n = \left(\frac{P_{Hg}}{P_{vdW}^{vap}} \right)^n . \tag{24}$$

This is consistent with our assumption that the nucleation event involves only non-metallic mercury clusters. Although this relation can be used to simplify the nucleation rate calculation, we have chosen to leave Eq. 18 in its present form to emphasize the influence of the binding character transition and to facilitate comparisons with other calculations of nucleation rate (J) as a function of saturation ratio (S). DeKruif, VanGinkel, and Langenberg [20] critically reviewed the low temperature vapor pressure data for Hg and present a correlation that agrees within 3% from the triple point (234K) to at least 1050K.[21] We will also make use of a correlation of the bulk surface tension.[22]

5.5 Results and Discussion

In Fig. 3, we show experimental measurements of mercury vapor nucleation rates and two estimates of that rate. The estimate from the current work is within the error bars (imposed primarily by the uncertainty in the Lennard-Jones energy parameter). (D_e) The other estimate is based on the capillarity approximation. In the capillarity approximation, the free energy difference (ΔG) is estimated using Eq. 2 and the bulk chemical potential and surface energy. The asymptotic expansion about the bulk equilibrium phase is truncated after the second term. For further discussion, see Refs.[7,8]. The capillarity approximation leads to large errors due to the metal/nonmetal transition that occurs around 13 mercury atoms. This is the hallmark of nanoscale materials: they have properties unlike single atoms or bulk.

The simple model that we have used to estimate the nucleation rate for mercury suggests that other systems are tractable, but that the unique character of nanoscale

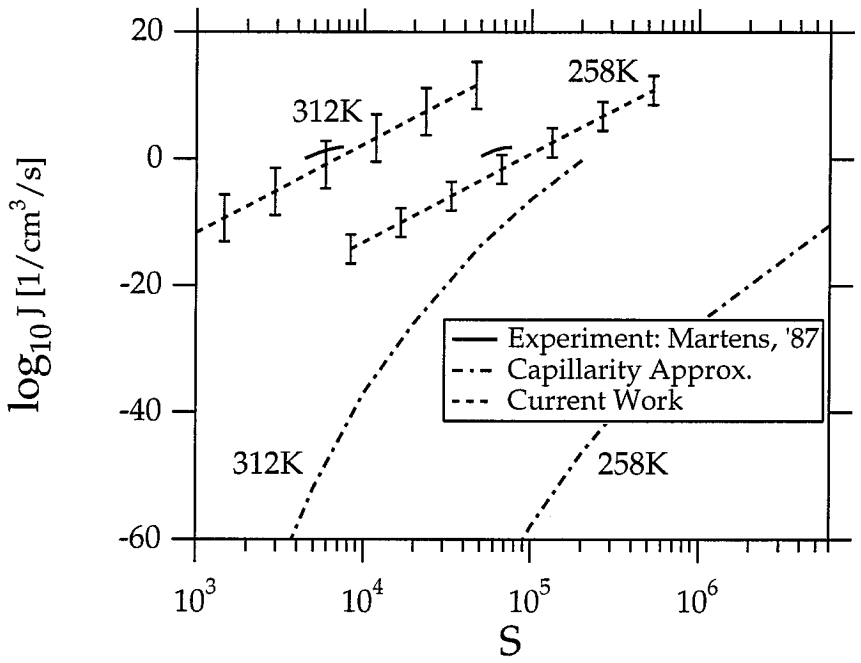

FIGURE 3 Nucleation rates (J) as a function of saturation ratio (S).

clusters must be incorporated in those estimates. Simple methods based on bulk properties are likely to give wildly erroneous results.

We are currently refining our model using *ab initio* calculations to obtain effective Lennard-Jones parameters appropriate for the 13-mer.[23]

5.6 Acknowledgments

Partial support of this work was provided by grants from NSF (CHE 95-22179) and from the International Fine Particle Research Institute.

5.7 References

[1]K. Rademann, B. Kaiser, U. Even, and F. Hensel, Phys. Rev. Lett. **59**, 2319 (1987).

[2]C. Bréchignac, M. Broyer, Ph. Cahuzac, G. Delacretaz, P. Labastie, J. P. Wolf, and L. Wöste, Phys. Rev. Lett. **60**, 275 (1988).

[3]H. Haberland, H. Kornmeier, H. Langosch, M. Oschwald, and G. Tanner, J. Chem. Soc. Faraday Trans. **86**, 2473 (1990).

[4]M. E. Garcia, G. M. Pastor, and K. H. Bennemann, Phys. Rev. Lett. **67**, 1142 (1991).

[5]R. C. Tolman, J. Chem. Phys. **17**, 333 (1949).

[6]R. B. McClurg, R. C. Flagan, and W. A. Goddard, J. Chem. Phys. **102**, 3322 (1995).

[7]D. W. Oxtoby, J. Phys. Condens. Matter. **4**, 7627 (1992).

[8]J. L. Katz, Pure Appl. Chem. **64**, 1661 (1992).

[9]R. R. Hultgren, *Selected values of the thermodynamic properties of the elements* (Am. Soc. for Metals, Metals Park, Ohio, 1973) p. 236.

[10]D. Kashchiev, J. Chem. Phys. **76**, 5098 (1982).

[11]D. W. Oxtoby and D. Kashchiev, J. Chem. Phys. **100**, 7665 (1994).

[12]J. Martens, H. Uchtmann, and F. Hensel, J. Phys. Chem. **91**, 2489 (1987).

[13]T. L. Hill, *Statistical Thermodynamics* (Dover, New York, 1986). p. 104.

[14]R. D. van Zee, S. C. Blankespoor, and T. S. Zwier, J. Chem. Phys. **88**, 4650 (1988).

[15]M. Dolg and H. J. Flad, J. Phys. Chem. **100**, 6147 (1996).

[16]A. Zehnacker, M. C. Duval, C. Jouvet, C. Lardeux-Dedonder, D. Solgadi, B. Soep, and O. J. Benoist d'Azy, J. Chem. Phys. **86**, 6565 (1987).

[17]A. Lotfi, J. Vrabec, and J. Fischer, Mol. Phys. **76**, 1319 (1992).

[18]J. E. Hunter and W. P. Reinhardt, J. Chem. Phys. **103**, 8627 (1995).

[19]The Tolman length is nearly independent of temperature for $T/T_c \leq 0.80$. [R. B. McClurg, R. C. Flagan, and W. A. Goddard, J. Chem. Phys. **105**, 7648 (1996).] For our system, this requires $kT/D_e \leq 1.06$ or $T < 575K$.

[20]C. G. DeKruif, C. H. D. VanGinkel, and A. Langenberg, Recueil. **92**, 599 (1973).

[21]R. H. Perry and D. W. Green (eds.), *Perry's Chemical Engineers' Handbook, 6th ed.* (McGraw-Hill, New York, 1984) p. 3-201. We suspect that the equilibrium pressure at 333.15K in the table has transposed digits and should read $3.536 \cdot 10^{-5}$bar.

[22]J. J. Jasper, J. Phys. Chem. Ref. Data **1**, 841 (1972).

[23]R. B. McClurg, B.-L. Tsai, R. C. Flagan, and W. A. Goddard, work in progress.

Chapter 6 Hindered Rotors in 1 Dimension

The Hindered Rotor Density-of-States Interpolation Function

Richard B. McClurg and Richard C. Flagan

Spalding Laboratory (210-41)

Division of Chemistry and Chemical Engineering

California Institute of Technology, Pasadena, California 91125

William A. Goddard, III[a)]

Materials and Process Simulation Center, Beckman Institute (139-74)

Division of Chemistry and Chemical Engineering

California Institute of Technology, Pasadena, California 91125

[a)]To whom correspondence should be addressed.

Abstract

We construct an approximation to the partition function for hindered rotors based entirely on their asymptotic behavior and no fitting parameters. The approximant is shown to be quite accurate in all temperature ranges. Explicit auxiliary functions are derived for the Helmholtz free energy, internal energy, heat capacity, and entropy. We apply this function to estimating the heat capacity and unimolecular dissociation rate for ethane.

05.20.-y 02.30.Mv 05.70.Ce

6.1 Introduction

Since the pioneering work of Pitzer[1,2] which showed that torsions about single bonds are not freely rotating, there have been many books[3–5] and reviews[6–11] on hindered rotation. The quantum mechanics of hindered rotors is well known, but the theory has been too cumbersome for many applications. Calculating the values from first principles requires evaluating and diagonalizing a large matrix. This is practical with modern computers, but this is often an unwelcomed diversion in the context of a larger problem. Pitzer's published tables for the thermodynamic functions of hindered rotors[1] are also inconvenient for use in computer programs. We would like to have a function that estimates the thermodynamic functions for hindered rotors without having to start from first principles for each application. One such function was proposed by Truhlar.[12] We will refer to this function as T91 hereafter. Herein we present an improvement, the Hindered Rotor Density-of-States (HRDS) interpolation function, which is asymptotically correct at low and high temperatures and accurate at intermediate temperatures.

In Sections 6.2 and 6.3, we derive asymptotic forms for the low-temperature (quantum) and high-temperature (classical) canonical partition functions (Q). The reader interested in applying the methods may skip to Sec. 6.4 which presents the HRDS interpolation function based on the asymptotic behavior of the partition function. There are no fitting parameters in determining this function. Instead, we construct a product of terms determined such that the function has the correct asymptotic behavior at both low and high temperature. By comparing with numerical values, we show that the function is accurate over the entire temperature range, much better than the previous function.[12] In Sec. 6.5, we compute thermodynamic functions based on the HRDS function. Finally, Sec. 6.6 gives two applications: calculation of the gas phase heat capacity of ethane and the dissociation rate constant of ethane. These examples serve to illustrate the benefits of the new function.

6.2 Low-Temperature (Quantum) Limit

In the low-temperature limit, the partition function must be calculated using the discrete energy levels computed using quantum mechanics. The time-independent Schrödinger Equation for rotation about a single axis is[13]

$$-\frac{\hbar^2}{2I}\frac{d^2\Psi}{d\phi^2} + V\Psi = E\Psi \tag{1}$$

$$0 \leq \phi < 2\pi.$$

Here, I is the reduced moment of inertia about the axis parametrized by ϕ. In many cases, I changes only slightly with ϕ and can be treated as a constant. Also, the potential (V) can be approximated using

$$V = \frac{W}{2}(1 - \cos n\phi) \tag{2}$$

where W is the height of the potential barrier, n is the number of equivalent minima, and $\phi = 0$ corresponds to a minimum.

With the following definitions,

$$2x = n\phi \tag{3}$$

$$\alpha = \frac{8I}{\hbar^2 n^2}(E - W/2) \tag{4}$$

$$2r^2 = \frac{8I}{\hbar^2 n^2}(W/2) \tag{5}$$

Eq. (1) transforms into Mathieu's equation:[14,15]

$$\frac{d^2\Psi}{dx^2} + (\alpha + 2r^2\cos 2x)\Psi = 0. \tag{6}$$

$$0 \leq x < n\pi$$

As discussed by Nielsen,[16] the periodicity of $n\pi$ in the potential requires solutions to

Eq. (6) having period $n\pi$, which have been studied primarily for $n = 1, 2$. Equation (6) has solutions only for characteristic values (α) which depend on r and n.

Large Barrier Limit (Harmonic Oscillator)

For barrier heights (W) which are large compared to both E and $\hbar\omega$, r is large and only the region of x near 0 is significant. Expanding Eq. (6) for small x leads to a perturbed harmonic oscillator (HO) with characteristic values (α)

$$\alpha = -2r^2 + (2 + 4m)r - \frac{1}{4}(1 + 2m + 2m^2) + \mathrm{O}(m^3/r) \tag{7}$$

$$m = 0, 1, 2, \ldots$$

that are n-fold degenerate, but otherwise independent of the periodicity (n).[15] Here, m is an integer index for the characteristic values. Solving Eqs. (4), (5), and (7) for E yields

$$E_m = \frac{\hbar^2 n^2 r}{2I}\left[(1/2 + m) - \frac{1}{16r}(1 + 2m + 2m^2) + \mathrm{O}(m^3/r^2)\right]. \tag{8}$$

Defining the HO frequency (ω) as

$$\omega = n\sqrt{\frac{W}{2I}}, \tag{9}$$

we see that Eq. (8) reduces to the energy levels of a harmonic oscillator[13] as r approaches ∞,

$$E_m = E_m^{HO} - \frac{\hbar\omega}{16r}(1 + 2m + 2m^2) + \mathrm{O}(m^3/r^2) \tag{10}$$

$$E_m^{HO} = \hbar\omega(1/2 + m). \tag{11}$$

The first effect of finite r is to *lower* the allowed energies relative to the corresponding HO values.

Eliminating I from Eqs. (5) and (9) yields

$$r = W/\hbar\omega. \tag{12}$$

Therefore, r is the ratio of the barrier height to the harmonic oscillator frequency (which is based on the curvature at the bottom of the potential well). Equivalently, r is a rough estimate of the number of quantum levels classically confined within a single well.

Using the limiting form for E at small m, we can calculate a limiting form for the canonical partition function (Q) at low temperature,

$$Q = \sum_m \exp[-E_m/kT]. \tag{13}$$

At sufficiently low temperature, Q is dominated by the first few terms of the summation in Eq. (13), for which the harmonic oscillator limit [Eq. (10)] holds,

$$\lim_{T\to 0} Q = \sum_{m=0}^{\infty} \exp\left[\frac{-E_m^{HO} + \frac{\hbar\omega}{16r}(1+2m+2m^2)}{kT}\right] \tag{14}$$

$$Q^{HO} = \sum_{m=0}^{\infty} \exp\left[-E_m^{HO}/kT\right] = \frac{\operatorname{csch}\left[\hbar\omega/2kT\right]}{2}. \tag{15}$$

Taking the first two terms of each summation and expanding yields:

$$\lim_{T\to 0} \frac{Q}{Q^{HO}} = \exp\left[\frac{\hbar\omega}{16rkT}\right]\left(1 + \exp\left[\Delta + \frac{\hbar\omega}{4rkT}\right] - \exp\left[\Delta\right]\right) \tag{16}$$

$$\Delta = \left(E_0^{HO} - E_1^{HO}\right)/kT = -\hbar\omega/kT.$$

Defining a non-dimensional temperature (Θ),

$$\Theta = kT/\hbar\omega, \tag{17}$$

simplifies Eq. (16) and helps quantify "sufficiently low temperature."

$$\lim_{\Theta \ll 1} \frac{Q}{Q^{HO}} = \exp\left[\frac{1}{16r\Theta}\right]\left(1 + \exp\left[\frac{-1}{\Theta} + \frac{1}{4r\Theta}\right] - \exp\left[\frac{-1}{\Theta}\right]\right) \tag{18}$$

Thus, for any finite value of r, the actual partition function *exceeds* Q_{HO} at low temperature. This follows directly from Eq. (11) since the first effects of finite r are to *lower* the allowed energies relative to the corresponding harmonic oscillator levels. The second term in Eq. (18) cannot be expanded about $\Theta = 0$. (The origin is an essential singular point[17] of $\exp[\pm\alpha/\Theta]$.) Therefore, we use the high-temperature asymptote.

Small Barrier Limit (Free Rotor)

If the barrier height (W) is small compared to E, then solutions to Eq. (6) are sums of slightly distorted sines and cosines with characteristic values[14,15]

$$\alpha = \left(\frac{2m}{n}\right)^2 + \frac{r^4}{2\left[(2m/n)^2 - 1\right]} + \mathrm{O}(r^6/m^4). \tag{19}$$

Solving Eqs. (4) and (19) for E yields

$$E_m = \frac{W}{2} + \frac{m^2\hbar^2}{2I} + \frac{r^4\hbar^2 n^2}{16I\left[(2m/n)^2 - 1\right]} + \mathrm{O}(r^6/m^4). \tag{20}$$

$$m = 0, \pm 1, \pm 2, \ldots$$

The first two terms in Eq. (20) correspond to the energy levels of a 1-dimensional free rotor[13] displaced by the average potential energy ($W/2$). This series is accurate as m approaches ∞, but is not uniformly convergent. The second term in Eq. (19) is correct for $|m| > n/2$. For smaller values of m, there are expansions analogous to Eq. (19), but those expansions must be derived individually for each (small) value of m. Higher-order terms in Eq. (19) are also correct for large $|m|$, but they similarly break down for small values of m. The truncated series is not accurate for $|m| < rn/2$. For these reasons, we use a different approach for the high-temperature limit in Sec. 6.3.

6.3 High-Temperature (Classical) Limit

At high temperatures, the canonical partition function (Q) has significant contributions from a large number of quantum states. See Eq. (13). In this limit, it is useful to use classical statistical mechanics in which the summation over states is approximated as an integral over phase space.[1]

$$\lim_{T\to\infty} Q = \frac{1}{h}\int_{-\infty}^{\infty}\int_{\alpha}^{\beta} \exp\left[\frac{-\mathcal{H}}{kT}\right]\, dq\, dp \tag{21}$$

Here, α and β are limits on the spatial coordinate (q), $\mathcal{H}$ is the Hamiltonian, and p is the momentum. For a rigid rotor with hindering potential $V(\phi)$, this reduces to

$$\lim_{T\to\infty} Q = \frac{1}{nh}\int_{-\infty}^{\infty} \exp\left[\frac{-J^2}{2IkT}\right]\, dJ \int_{0}^{2\pi} \exp\left[\frac{-V}{kT}\right]\, d\phi \tag{22}$$

where J is the angular momentum. The factor $1/n$ eliminates over-counting of states due to the n equivalent wells. For the cosine potential in Eq. (2), the second integral can be simplified.

$$\lim_{T\to\infty} Q = \frac{2\exp\left[-W/2kT\right]}{nh}\int_{-\infty}^{\infty} \exp\left[\frac{-J^2}{2IkT}\right]\, dJ \int_{0}^{\pi} \exp\left[\frac{W}{2kT}\cos\phi\right]\, d\phi \tag{23}$$

Both of these integrals are in standard forms,[18] which can be integrated to give

$$\lim_{T\to\infty} Q = \left\{\frac{(2\pi IkT)^{1/2}}{n\hbar}\right\} \exp\left[\frac{-W}{2kT}\right] \mathrm{I}_0\left[\frac{W}{2kT}\right]. \tag{24}$$

The first term in Eq. (24) is the classical partition function for a one-dimensional free rotor (Q^{FR}).[13] The second term is a Boltzmann factor for the average potential energy. The third term, I_0, is a zeroth-order modified Bessel function,[15,18] which accounts for the rotor preferentially residing in the potential wells (as opposed to the potential maxima) at finite temperature. An equivalent function was used by Pitzer

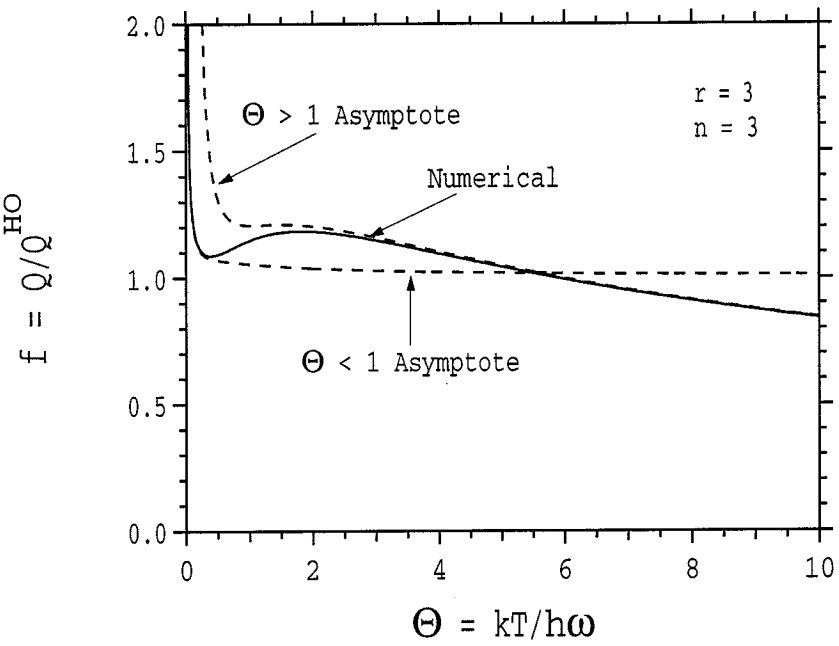

FIGURE 1 Asymptotes for $\Theta \ll 1$ (Eq. 18) and $\Theta \gg 1$ (Eq. 25). For $\Theta \approx 2r/3$, the hindered rotor is intermediate between a harmonic oscillator and a free rotor, requiring the use of an interpolation function.

and Gwinn.[2] Using the notation of Sec. 6.2, Eq. (24) can be simplified.

$$\lim_{\Theta \gg 1} Q = (\pi \Theta r)^{1/2} \exp\left[\frac{-r}{2\Theta}\right] \mathrm{I}_0\left[\frac{r}{2\Theta}\right] \tag{25}$$

This asymptote is depicted in Fig. 1 along with numerical results, both for $r = 3$. The numerical results were obtained by solving Eq. (6) for the first 400 characteristic values (α) using an eigenfunction expansion.[19,20] The numerical results agree with tabulated values.[14] We then calculated Q using Eq. (13) directly. In Fig. 1, we see that Q approaches the low temperature limit for $\Theta \ll 1$ and the high temperature limit for $\Theta \gg 1$.

Since Eq. (15) is the partition function for a harmonic oscillator at any temperature, it can be expanded in the limit of high temperature to give the classical limit for Q^{HO},

$$\lim_{\Theta \gg 1} Q^{HO} = \Theta + \mathrm{O}(\Theta^{-1}). \tag{26}$$

We use this result in Sec. 6.4.

6.4 The Hindered Rotor Density-of-States (HRDS) Function

In this section, we construct an interpolation function having the asymptotic forms determined in Sections 6.2 and 6.3. For this purpose, it is convenient to define f as follows:

$$f = Q/Q^{HO}. \tag{27}$$

Then Eqs. (18), (25), and (26) provide limiting values for f

$$\lim_{\Theta \ll 1} f = \exp\left[\frac{1}{16r\Theta}\right](1 + \mathrm{O}(\exp[-\alpha/\Theta])) \tag{28}$$

$$\lim_{\Theta \gg 1} f = \left(\frac{\pi r}{\Theta}\right)^{1/2} \exp\left[\frac{-r}{2\Theta}\right] \mathrm{I}_0\left[\frac{r}{2\Theta}\right]. \tag{29}$$

The first term in Eq. (28) comes from the zero-point energy which is a quantum-mechanical effect. The remainder of Eq. (28) and all of Eq. (29) are from density of states considerations. Therefore, we write Eq. (27) in the following form:

$$f = P \exp\left[\Delta E^{zp}/kT\right]. \tag{30}$$

We use the following Padé approximant for ΔE^{zp}

$$\Delta E^{zp} = \frac{\hbar\omega}{2 + 16r}, \tag{31}$$

and approximate P using its high-temperature limit

$$P = \left(\frac{\pi r}{\Theta}\right)^{1/2} \exp\left[\frac{-r}{2\Theta}\right] \mathrm{I}_0\left[\frac{r}{2\Theta}\right]. \tag{32}$$

The Padé approximant corrects for the over-estimate of the zero-point energy in the HO reference function. For large r, the over-estimate is $\hbar\omega/16r$. See Eq. (10). For $r = 0$, there is no hindering potential, so $E^{zp} = 0$ and the over-estimate is $\hbar\omega/2$.

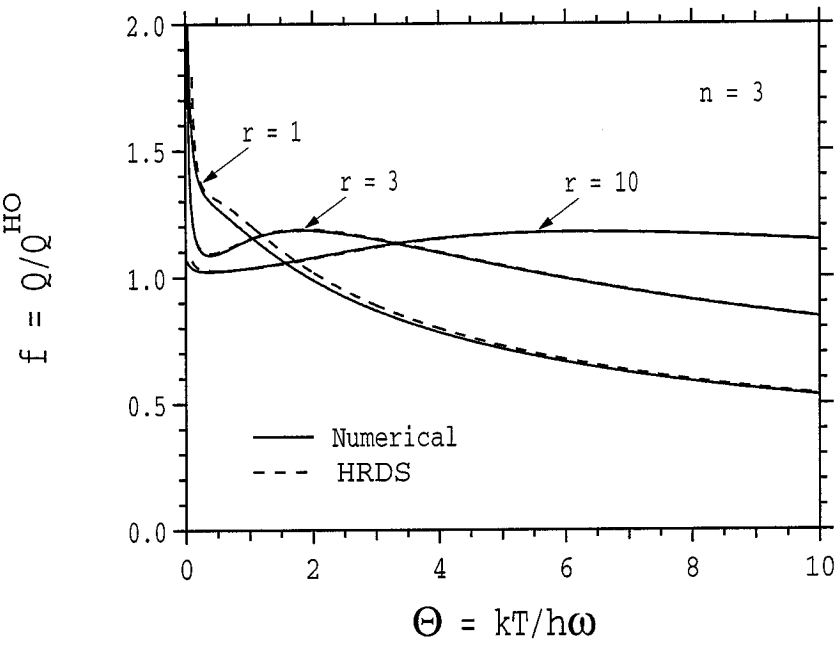

FIGURE 2 Accuracy of the HRDS interpolation function for various values of r. This shows that HRDS is accurate for both mildly hindered rotors ($r \approx 1$) and strongly hindered rotors ($r > 1$). On the scale of this plot, the curves are indistinguishable for r greater that about two.

Using the following expansion for $\mathrm{I}_0[z]$ where z can be complex[15,18]

$$\lim_{|z|\to\infty} \mathrm{I}_0[z] = \exp[z]/(2\pi z)^{1/2}, \tag{33}$$

it is simple to confirm that P approaches unity at low temperatures. We refer to P as the Hindered Rotor Density-of-States (HRDS) interpolation function. In Fig. 2, we show that the HRDS function is accurate for both mildly hindered rotors ($r \approx 1$) and strongly hindered rotors ($r > 1$). This is significantly more accurate than the previous interpolating function, T91, as shown in Fig. 3. The greatest improvement is in the neighborhood of $\Theta = 2r/3$ where the hindered rotator is intermediate between a harmonic oscillator and a free rotor.

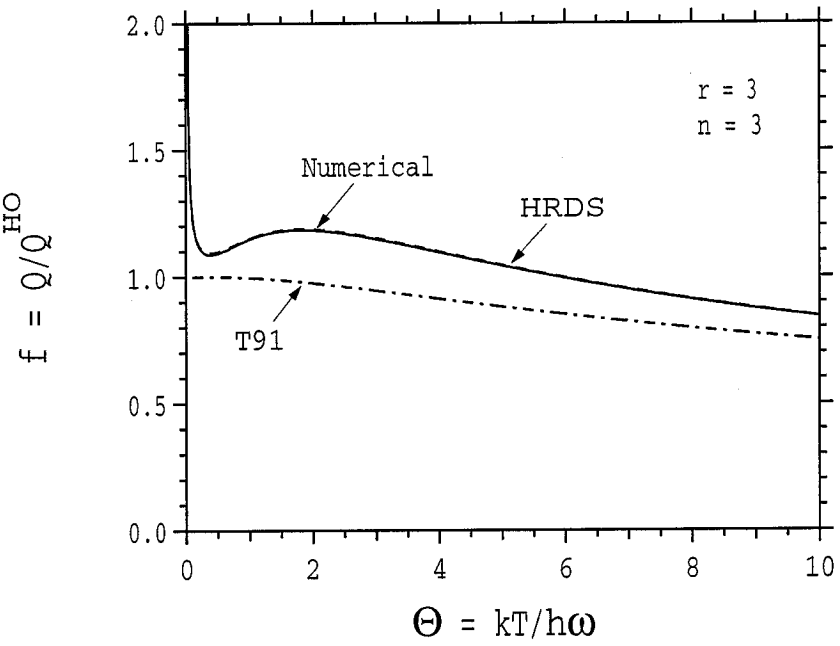

FIGURE 3 Accuracy of the current work (HRDS) and an alternative interpolation scheme by Truhlar (T91).[12] The current work better represents the numerical results, especially near $\Theta = 2r/3$ where the hindered rotor is intermediate between the harmonic oscillator limit and the free rotor limit.

6.5 Thermodynamic Functions

Using our estimate for f [Eqs. (30) and (32)], we calculate[13] deviations from the harmonic oscillator value for the Helmholtz free energy (ΔA),

$$\begin{aligned} \Delta A/kT &= -\ln f \\ &= \frac{-1}{(2+16r)\Theta} + \frac{r}{2\Theta} - \ln\left\{\left(\frac{\pi r}{\Theta}\right)^{1/2} \mathrm{I}_0\left[r/2\Theta\right]\right\}; \end{aligned} \tag{34}$$

internal energy (ΔU),

$$\begin{aligned} \Delta U/kT &= T\frac{d(\ln f)}{dT} \\ &= \frac{-1}{2} - \frac{1}{(2+16r)\Theta} + \frac{r}{2\Theta}\left\{1 + \frac{\mathrm{I}_1\left[r/2\Theta\right]}{\mathrm{I}_0\left[r/2\Theta\right]}\right\}; \end{aligned} \tag{35}$$

heat capacity (ΔC_v),

$$\begin{aligned}\Delta C_v/k &= T\frac{d^2(T\ln f)}{dT^2} \\ &= \frac{-1}{2}+\frac{r^2}{8\Theta^2}\left\{1-2\left(\frac{\mathrm{I}_1[r/2\Theta]}{\mathrm{I}_0[r/2\Theta]}\right)^2+\frac{\mathrm{I}_2[r/2\Theta]}{\mathrm{I}_0[r/2\Theta]}\right\};\end{aligned} \tag{36}$$

and entropy (ΔS),

$$\Delta S/k = \Delta U/kT - \Delta A/kT. \tag{37}$$

There are widely available routines for calculating $\mathrm{I}_\nu[x]$ where x is real and ν is an integer.[21] Alternatively, the following expressions can be used.[15,18]

$$\mathrm{I}_\nu[x] = \sum_{k=0}^{\infty}\frac{(x/2)^{\nu+2k}}{k!(k+\nu)!} \tag{38}$$

$$\mathrm{I}_\nu[x] = \frac{\exp[x]}{(2\pi x)^{1/2}}\sum_{k=0}^{\infty}\frac{(-1)^k\Gamma[\nu+k+1/2]}{(2x)^k k!\Gamma[\nu-k+1/2]} \tag{39}$$

The first expression is recommended[15] for $|x| < 3.75$ and the second for $|x| > 3.75$.

6.6 Applications

The only input parameters to HRDS are the periodicity (n), the ratio of barrier height to harmonic frequency (r), and the scaled temperature (Θ). Before applying HRDS to calculate the heat capacity and rate constant for dissociation of ethane, we briefly discuss how to estimate these values.

For simple cases, n can be determined by symmetry. Following the notation of Wolfe,[22] consider a torsion between atoms M and N with ligands a, b, c, x, y, and z. The ligands can be atoms, groups of atoms, or lone pairs of electrons.

(i.) $abcM-Nxyz$: If a, b, and c (and/or x, y, and z) are identical, then there are three equivalent minima. ($n = 3$) (e.g. Ethane $\{H_3C-CH_3\}$, Methyl amine $\{H_2N-CH_3\}$, and Methanol $\{HO-CH_3\}$)

(ii.) $abcM-Nxy$: If a, b, and c are identical and x and y are identical, then there are six equivalent minima. ($n = 6$) (e.g. Methyldifluoroborane $\{CH_3-BF_2\}$ and

Toluene $\{H_3C - Ph\}$ where N, x, and y are all part of the phenyl ring)

(iii.) $abcM - Nxyz$: For particular choices of ligands, there may be two equivalent minima. ($n = 2$) (e.g. HSSH has two minima at $\phi = \pm 90$ deg.)

For torsions that do not meet the restrictions of the above three cases, the potential may not be well-represented by Eq. (2) and this method may not be appropriate. For example, Hydrogen peroxide ($HO-OH$) has two equivalent minima separated by one large and one small barrier.[22] Diphenyl ($Ph - Ph$) has four minima with alternating large and small barriers to rotation. These potentials cannot be represented using a single Fourier component as in Eq. (2).

The harmonic oscillator frequency (ω) and the height of the potential barrier (W) can be measured experimentally or calculated using quantum mechanics or empirical force fields. See Berg[11] for a recent survey of the various methods. Also, see Lowe[8] for an extensive tabulation of experimental data. Once ω and W are known and the temperature of interest (T) is chosen, r and Θ are calculated using Eqs. (12) and (17).

Ethane Heat Capacity

As a sample application of the HRDS function, we calculate the heat capacity of ethane. Heat capacity provides a stringent test of the shape of the partition function since it requires second derivatives. See Eq. (36). We have used spectroscopic data recommended by Chao[23] (ω=289cm^{-1}, W = 2.96 kcal/mol, n = 3). For comparison with experimental data, we use an equation of state for ethane based on a critical review of the available spectroscopic and thermodynamic experiments.[24]

Figure 4 shows that the HRDS interpolation function provides a good approximation to the experimental data in the temperature range where data is available. Both HRDS and T91 utilize the harmonic oscillator and rigid rotor limiting behavior, but HRDS puts greater emphasis on accurately reflecting how those asymptotes are reached. This is particularly evident in the neighborhood of the peak in ΔC_v where the hindered rotor is far from either limiting case. For ethane, this occurs near room

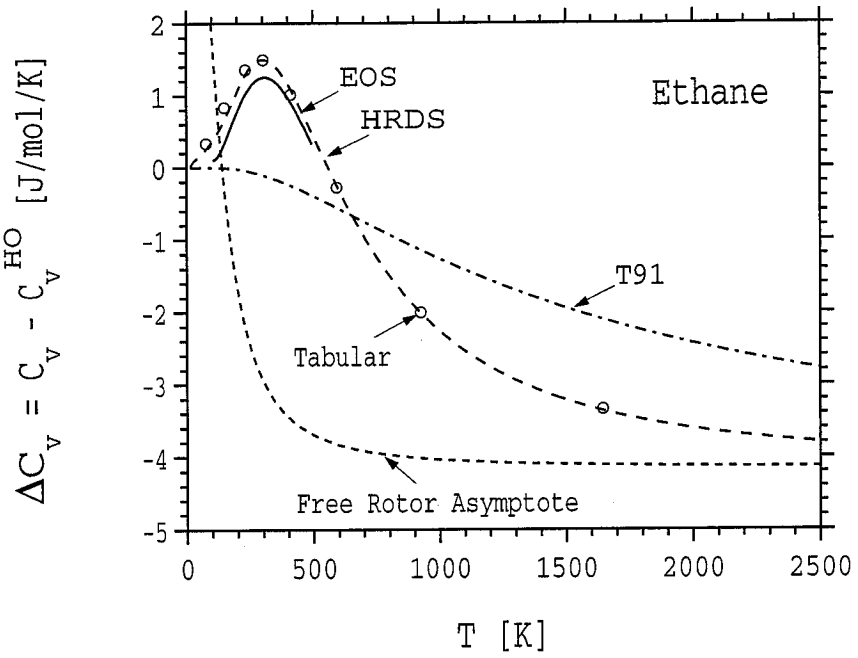

FIGURE 4 Comparison of the deviations from the harmonic oscillator heat capacity for ethane as calculated using linear interpolation from Pitzer's tables (Tabular),[2] the T91 interpolation function,[12] and the current work (HRDS). The equation of state curve (EOS) is the result of fitting a partition function to a critically analyzed set of experimental data.[24] Also shown is the rigid rotor (high-temperature) asymptote. HRDS agrees well with the tabulated results and the EOS.

temperature.

Ethane Dissociation Rate Constant

Our second illustration is estimating the high-pressure, unimolecular rate constant for ethane dissociation into methyl radicals. We use canonical transition state theory as discussed by Benson.[25] This is not the most accurate theory available, but it serves to illustrate the contribution of hindered rotation without unnecessary complication. See Marcus[26] for a discussion of microcanonical methods applied to methyl radical recombination. In transition state theory, the rate constant for unimolecular dissociation (k_d) can be expressed as

$$k_d = (kT/h)K^{\ddagger} \tag{40}$$

where $K^{\ddagger}$ is the equilibrium constant for formation of the activated complex with the reaction coordinate vibration factored out. An equilibrium constant can always be expressed as a ratio of partition functions. In the present case, this leads to

$$K^{\ddagger} = \frac{q^{\ddagger}}{q^{r}} = g_e \frac{\left(q^{rot} \prod_{i=1}^{3n-7} q_i^{vib}\right)^{\ddagger}}{\left(q^{rot} \prod_{i=1}^{3n-6} q_i^{vib}\right)^{r}} \exp\left[\frac{-\Delta E}{kT}\right]. \tag{41}$$

In Eq. (41), ΔE is the potential energy of the transition state relative to the reactant, q^{rot} is the partition function for rigid rotation of the molecule as a whole, q^{vib} is the vibrational partition function for each of the internal degrees of freedom, r refers to the reactant molecule, and $\ddagger$ refers to the transition state. Since $K^{\ddagger}$ is the ratio of partition functions, this application serves to test the magnitude of the partition function. We assume that the transition state and equilibrium ethane are singly degenerate ($g_e = 1$) with D_{3d} symmetry ($\sigma^{\ddagger} = \sigma^{r}$). This simplifies the equilibrium constant.

$$K^{\ddagger} = \left(\frac{I_A^{\ddagger} I_B^{\ddagger} I_C^{\ddagger}}{I_A^{r} I_B^{r} I_C^{r}}\right)^{1/2} \frac{\left(\prod_{i=1}^{3n-7} q_i^{vib}\right)^{\ddagger}}{\left(\prod_{i=1}^{3n-6} q_i^{vib}\right)^{r}} \exp\left[\frac{-\Delta E}{kT}\right] \tag{42}$$

Here, I_A, I_B, and I_C are the principle moments of inertia of the molecule as a whole.

We use a published parametrization of the potential energy surface along the minimum energy path for dissociation.[27] It gives the vibrational frequencies, the barrier to internal rotation, and the molecular geometry as a function of the separation between carbon atoms. This distance is identified as the reaction coordinate. The transition state is the point along the reaction coordinate that minimizes $K^{\ddagger}$.

Figure 5 shows that using the HRDS function leads to slightly better agreement with the experimental results than using T91 over the entire temperature range covered. The largest difference between the approximations occurs when $\Theta \approx 2r/3$. At this point, ethane is intermediate between the harmonic oscillator and the free rotor limit and the ratio between HRDS and T91 is about 1.2. The transition state for ethane dissociation is "loose." This means that the carbon-carbon bond is nearly bro-

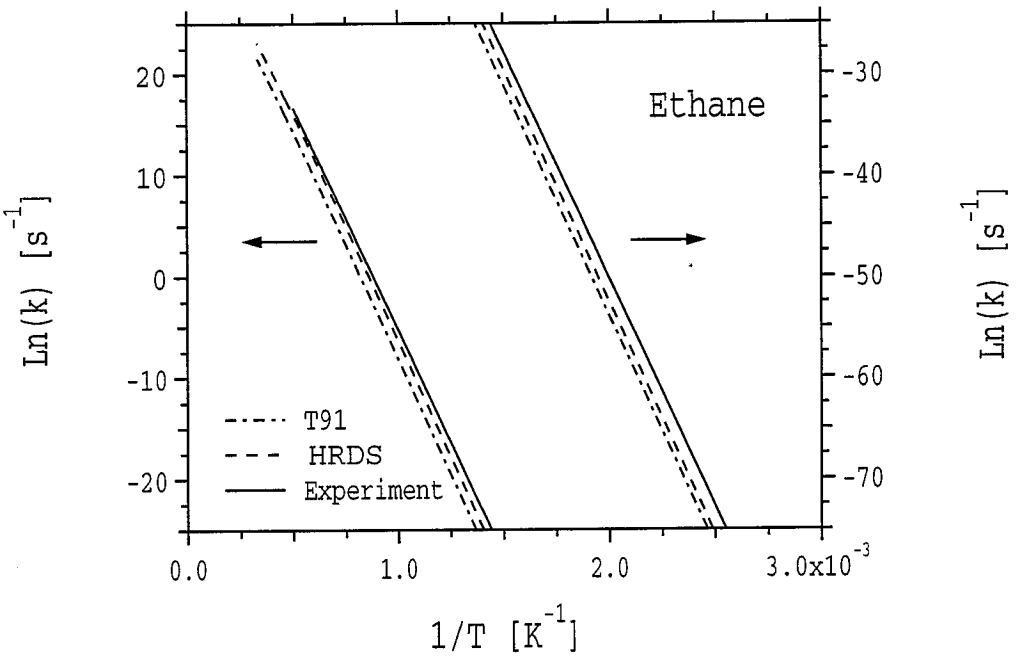

FIGURE 5 High-pressure, unimolecular rate constant for dissociation of ethane into methyl radicals. The calculated values are based on Robertson's potential energy parametrization[27] and two approximations for the hindered rotor. The experimental curve is a correlation from a critical analysis of kinetic and thermodynamic data.[28] Calculations based on the current work (HRDS) are closer to the experimental values than T91, but the maximum ratio between them is within the uncertainty of the experimental values. (The author estimates this uncertainty at a factor of two, which is ±0.7 on this scale.)

ken and the hindering potential is very small at the transition state. In the free rotor limit, HRDS and T91 agree, so their ratio approaches one. Therefore, the largest difference between the estimates for reaction rates is about 20%, which is well within the error bounds for kinetics experiments. Since the HRDS function is just as easy to use and more accurate, it can still be recommended over T91 even though kinetics experiments are unlikely to confirm one over the other.

6.7 Conclusions

We developed the HRDS interpolation function for readily estimating the partition function and thermodynamic functions for hindered rotors. The function is considerably easier to use than recalculation from first principles or interpolating from existing tables.[1,2] Our approximant to the partition function (HRDS) is based entirely on the

asymptotic behavior of the quantum-mechanical partition function at low temperature and the classical partition function at high temperature. There are no fitting parameters in this function. We have shown this function to be accurate in the temperature range intermediate between the harmonic oscillator and free rotor limits. We expect that this interpolation function will be useful in estimating thermodynamic and kinetic data for molecules and solids with hindered rotation about one axis.

6.8 Acknowledgments

This research was funded by NSF (CHE 95-22179 and ASC 92-17368). The facilities of the MSC are also supported by grants from DOE-BCTR, Chevron Petroleum Technology, Asahi Chemial, Aramco, Owens Corning, Chevron Chemical Co., Asahi Glass, Chevron Research and Technology Co., BP Chemical, Hercules, Avery Dennison, and Beckman Institute.

6.9 References

[1]K. S. Pitzer, J. Chem. Phys. **5**, 469 (1937).

[2]K. S. Pitzer and W. D. Gwinn, J. Chem. Phys. **10**, 428 (1942).

[3]S. Mizushima, *Structure of Molecules and Internal Rotation* (Academic Press, New York, 1954).

[4]W. J. Orville-Thomas, *Internal Rotation in Molecules* (Wiley, London, 1974).

[5]D. G. Lister, J. N. Macdonald, and N. L. Owen, *Internal Rotation and Inversion* (Academic Press, London, 1978).

[6]E. B. Wilson, Jr., Adv. Chem. Phys. **2**, 367 (1959).

[7]J. Dale, Tetrahedron **22**, 3373 (1966).

[8]J. P. Lowe, Prog. Phys. Org. Chem. **6**, 1 (1968).

[9]H. Förster and F. Vögtle, Agnew. Chem. **16**, 429 (1977).

[10]D. A. Long, J. Mol. Struct. **126**, 9 (1985).

[11]U. Berg and J. Sandström, Adv. Phys. Org. Chem. **25**, 1 (1989).

[12]D. G. Truhlar, J. Comput. Chem. **12**, 266 (1991).

[13]D. A. McQuarrie, *Statistical Mechanics* (Harper & Row, New York, 1976), pp. 10, 58, 96-98, and 138-140.

[14]N. W. McLachlan, *Theory and Application of Mathieu Functions* (Dover, New York, 1964), pp. 10, 17, and 371. For convenience, we have used $-q = r^2$.

[15]M. Abramowitz and I. A. Stegun (eds.), *Handbook of Mathematical Functions* (Dover, New York, 1965), pp. 374-379 and 722-726. This reference uses different, but equivalent notation for the Mathieu function. The following rules can be used to translate their notation to ours: $r \rightarrow m$, $a \rightarrow \alpha$, and $q \rightarrow -r^2$.

[16]H. H. Nielsen, Phys. Rev. **40**, 445 (1932).

[17]R. V. Churchill and J. W. Brown, *Complex Variables and Applications, 5th ed.*, (McGraw Hill, New York, 1990), pp. 173-174.

[18]I. S. Gradshteyn and I. M. Ryzhik, *Tables of Integrals, Series, and Products, 5th ed.*, (Academic Press, San Diego, 1994), pp. 354, 961, 968, 971, and 973.

[19]D. Zwillinger, *Handbook of Differential Equations, 2nd ed.*, (Academic Press, Boston, 1992), pp. 223-230.

[20]The eigenvalues (α) were calculated using a program written by one of us. (RBM) The program uses the LAPACK routines for the matrix diagonalization. E. Anderson, Z. Bai, C. Bischof, *et al.*, LAPACK, (SIAM, Philadelphia, 1992).

[21]W. H. Press, S. A. Teukolsky, W. T. Vetterling, and B. P. Flannery, *Numerical Recipes in FORTRAN, 2nd ed.*, (Cambridge University Press, Cambridge, U.K., 1992), pp. 229-233.

[22]S. Wolfe, Acc. Chem. Res. **3**, 102 (1970).

[23]J. Chao, R. C. Wilhoit, and B. J. Zwolinski, J. Phys. Chem. Ref. Data **2**, 427 (1973).

[24]D. G. Friend, H. Ingham, and J. F. Ely, J. Phys. Chem. Ref. Data **20**, 275 (1991).

[25]S. W. Benson, *The Foundations of Chemical Kinetics* (Krieger, Malabar, FL, 1982) pp. 247-250.

[26]D. M. Wardlaw and R. A. Marcus, J. Phys. Chem. **90**, 5383 (1986).

[27]S. H. Robertson, D. M. Wardlaw, and D. M. Hirst, J. Chem. Phys. **99**, 7748 (1993).

[28]D. L. Baulch, C. J. Cobos, R. A. Cox, *et al.*, J. Phys. Chem. Ref. Data **23**, 847 (1994).

Chapter 7 C_{60} Multipole Moments

C_{60} Multipole Moments

Richard B. McClurg

Spalding Laboratory (210-41)

Division of Chemistry and Chemical Engineering

California Institute of Technology, Pasadena, California 91125

William A. Goddard, III[a)]

Materials and Process Simulation Center, Beckman Institute (139-74)

Division of Chemistry and Chemical Engineering

California Institute of Technology, Pasadena, California 91125

[a)]To whom correspondence should be addressed.

Abstract

We estimate the multipole moments of C_{60} using the distributed multipole approach of Stone. (A. J. Stone, Chem. Phys. Lett. **83**, 233 (1981).) We find that by placing small dipoles on carbon centers and bond centers we fit the first four symmetry allowed multipoles to within about 15%. In addition, the fifth multipole, which was not fit, is in error by only 25%, indicating that this model captures the essence of the electron distribution in C_{60}. We interpret the fit dipoles in terms of modifications of atomic orbitals. The model qualitatively explains the observed interaction potential in solid C_{60}.

To be submitted for publication.

7.1 Introduction

For the past several years, C_{60} has attracted attention as an ideal plastic crystalline substance.[1–6] Plastic crystals are molecular solids with translational order, but with no orientational order.[7] There is a range of temperatures, below the melting temperature but above a lower limit, in which the molecules pack as if they were spinning and/or tumbling rapidly but the center of mass librates about an equilibrium position within the crystal. James and Keenan developed the theory which is used to describe the phase transitions in plastic crystalline substances based on the multipole interactions between molecules.[8]

Existing models for the charge distribution of C_{60} have been based on distributed point charges.[9,10,12] In this paper, we fit the multipoles of C_{60} determined by *ab initio* calculation[12] using the distributed multipole approach of Stone.[13] He proposed that the molecular charge distribution of a molecule should be represented as a collection of charges and multipoles on atoms and bond centers, rather than a single center for the entire molecule. For quantum-mechanical calculations with basis sets composed of linear combinations of atomic orbitals, the expansions about atoms and bond centers are finite. Expansions about other points are infinite and tend to have rapidly growing coefficients.[13] This property leads to sizable truncation errors when a finite number of terms are used. A drawback to this approach is that the computed multipoles are basis set dependent, particularly for high order multipoles.

7.2 Symmetry Adapted Functions

We make use of functions which contain the icosahedral symmetry of the C_{60} molecule to ensure that the results are consistent. First, we define regular solid harmonics (R_l^m) in terms of the spherical surface harmonics (Y_l^m)

$$R_l^m(\mathbf{r}) = \left(\frac{4\pi}{2l+1}\right)^{1/2} |\mathbf{r}|^l Y_l^m(\omega). \tag{1}$$

Here, $\mathbf{r}$ is the vector from the origin to a point in space and ω is the direction of that vector in terms of the angles θ and ϕ relative to a fixed set of coordinates. Linear combinations of regular solid harmonics (R_l^m) which transform like the irreducible representations (Γ) of a point group are called symmetry adapted functions (SAFs)

$$S_{l,\Gamma,i} = \sum_{m=-l}^{l} C_{l,\Gamma,i,m} R_l^m. \tag{2}$$

In Eq. (2), i is an index for the $h(\Gamma)$ members in the Γ representation. The values of the coefficients ($C_{l,\Gamma,i,m}$) depend upon the orientation of the molecule with respect to the coordinate system for the surface harmonics. Tabulated values for the icosahedral point group (I_h) are available for the x-z plane coincident with a mirror plane and a five-fold axis oriented along the z-axis[14–18] and for the x-z plane coincident with a mirror plane and a two-fold axis oriented along the z-axis.[4,19] Coefficient values for other orientations can be determined from the tabulated values using standard methods.[20] In this paper, we make extensive use of the one dimensional, even parity functions ($\Gamma = A_{1g}$, $i = 1$) which have the full symmetry of the molecule. Any observable property of the molecule, including its multipoles, can be expanded in terms of these functions. From here on, we will drop the second and third indices from the S functions and the coefficients (C) with the understanding that we are working with the fully symmetric functions only.

7.3 Form Factors

We use the SAFs to define form factors (f_l) for the various centers (s = c, ph, hh)

$$f_l^s = \sum_i S_l(\mathbf{r_i}). \tag{3}$$

The index i identifies each of the 60 carbon centers, 60 bonds between pentagonal and hexagonal faces (ph bonds), or 30 bonds between two hexagonal faces (hh bonds). Due to symmetry, there are non-zero SAFs only for certain values of l.[16] The first

allowed ls are 0, 6, 10, 12, 16, and 18. For $l > 30$, there can be more than one independent SAF, but this will not concern us. The form factors for the hh bonds are fixed by the icosahedral symmetry. They are $\{30/(4\pi)^{1/2}, -6.325, -13.746, 17.539, -4.823, -9.942\}$. The vectors $\mathbf{r_i}$ which point to the carbon centers and ph bonds are not imposed by symmetry. To determine them, we need to specify the locations of the carbon atoms. We use the experimentally determined average bond lengths (1.391Å, 1.455Å) for hh and ph bonds, respectively.[21] These values and icosahedral symmetry are sufficient to determine the needed vectors $\mathbf{r_i}$. Using these vectors leads to the form factors for the carbon centers $\{60/(4\pi)^{1/2}, 2.384, -19.482, -7.607, -17.782, 38.383\}$ and for the hp bond centers $\{60/(4\pi)^{1/2}, 11.218, -4.420, -24.193, 4.541, -20.577\}$. Michel uses a slightly different definition for the form factor and reports the absolute value of our definition.[2] His values differ from ours mainly because he used experimental values for the position vectors ($\mathbf{r_i}$) which deviate slightly from full icosahedral symmetry.

7.4 Charges

Since multipole moments (Q_l^m) are defined in terms of spherical surface harmonics (Y_l^m), it is trivial to determine the multipoles which result from charges on the carbon centers (q^c), hp bond centers (q^{hp}), and hh bond centers (q^{hh}),

$$Q_l^m = q^s f_l^s / C_l^m. \tag{4}$$

Electrical neutrality ensures that

$$0 = 60q^c + 60q^{hp} + 30q^{hh}. \tag{5}$$

It has been determined from *ab initio* calculations that the charge distribution on the hp and hh bonds are nearly identical.[12] Thus, we will require that

$$q^{hp} = q^{hh}. \tag{6}$$

We find that relaxing this restriction does not significantly change the results of our calculations. Combining Eqs. (3) - (6) gives the molecular multipoles due to charge redistribution

$$Q_l^m = q(3f_l^c/2 - f_l^{hp} - f_l^{hh})/C_l^m \tag{7}$$

$$Q_l^0 = q\{0,\ -0.439,\ -5.210,\ -3.851,\ -11.823,\ 41.208\}. \tag{8}$$

The parameter q is the absolute value of the charge on each bond. We have used the SAF coefficients (C_l^0) for the icosahedron oriented with a five-fold axis along the z-axis and a mirror plane in the x-z plane. This is the orientation used by Yildirim.[12] Multipoles with other values of m are readily computed using Eq. (7) and tables of C_l^m.[14–18]

7.5 Dipoles

Dipoles of magnitude μ can be imagined as being composed of two charges of magnitude $\mu e/2\epsilon$ and opposite sign, separated by a distance ϵ, where ϵ is small. By convention, the direction of the dipole is parallel to the vector pointing from the negative charge to the positive charge. The molecular multipoles which result from distributed dipoles at center s follows directly from this construction and the definition of the gradient

$$Q_l^m = \mu \cdot \nabla f_l^s / C_l^m. \tag{9}$$

Direct application of Eqs. (1) and (9) shows that the molecular multipole moments due to the radial component of the distributed dipoles are simply l times the multipole moments due to charges at the same location.

$$Q_l^m = l\mu_r^s f_l^s / C_l^m. \tag{10}$$

Here, μ_r^s stands for the radial component of the dipole at center s. The molecular multipole moments due to the tangential component of the distributed dipole are zero

by symmetry for the hh bond centers. As for the bond charges, we assume that the dipoles at the hh and ph bond centers are equal,

$$\mu_r^{hp} = \mu_r^{hh} \tag{11}$$

$$\mu_t^{hp} = \mu_t^{hh} = 0. \tag{12}$$

Using Eq. (10) leads to the following values for the molecular multipole moments due to the tangential component of dipoles at carbon centers (oriented along hh bonds by symmetry),

$$Q_l^0 = \mu_t^c\{0,\ -135.998,\ -98.652,\ -217.467,\ 125.413,\ 125.752\}; \tag{13}$$

the radial component of dipoles at carbon centers,

$$Q_l^0 = \mu_r^c\{0,\ 9.490,\ -70.710,\ -53.442,\ -127.569,\ 362.478\}; \tag{14}$$

and the radial dipoles at bond centers,

$$Q_l^0 = \mu_r^b\{0,\ 16.866,\ -53.960,\ -33.949,\ -2.188,\ -198.026\}. \tag{15}$$

We use b to stand for the hh and ph bond centers.

7.6 Multipole Moments

There are four undetermined parameters in Eqs. (7) and (13) - (15). They are the magnitudes of the bond charge and the various dipoles. We fit these values to the first four non-zero molecular multipole moments from *ab initio* calculations.[12] The fifth will serve as a check on our method. We find the best agreement for $q = 0$, $\mu_t^c = -0.00891$, $\mu_r^c = 0.0144$, and $\mu_r^b = -0.0610$. Our fit multipoles along with the calculated values and two point charge models are given in Table I and illustrated in Figs. 1 and 2.

TABLE I Molecular Multipole Moments

Source	q_6^0	q_{10}^0	q_{12}^0	q_{16}^0	q_{18}^0
Distributed Multipoles (Current Work)	0.319	3.154	-0.635	-2.819	16.180
ab initio[12] Method 1	0.295	3.550	-0.751	-2.614	22.895
ab initio[12] Method 2	0.285	3.626	-0.793	-2.431	19.997
LLM Model[9]	3.781	1.865	-7.339	1.243	-0.001
SCK Model[10]	1.582	0.198	-3.620	-0.842	4.807
GG Model[11]	1.184	0.880	-2.018	1.082	-2.445
YHE Model[12]	0.29	3.6	-0.77	-2.5	21.5

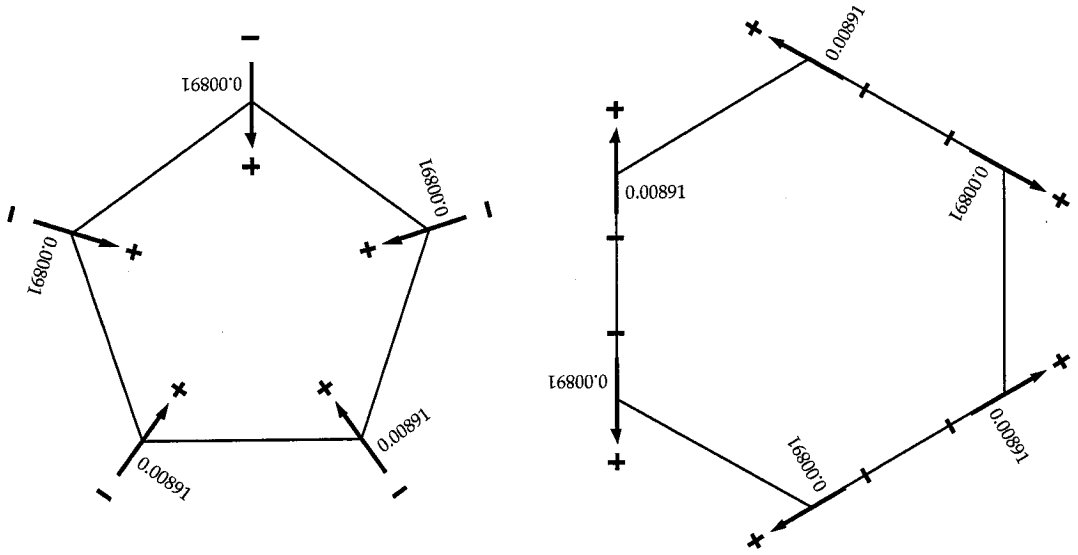

FIGURE 1 Distributed dipoles for C_{60} pentagonal and hexagonal faces. For clarity, only the tangential components are shown and they are labeled with the dipole magnitude, not the projected component in the plane of the face.

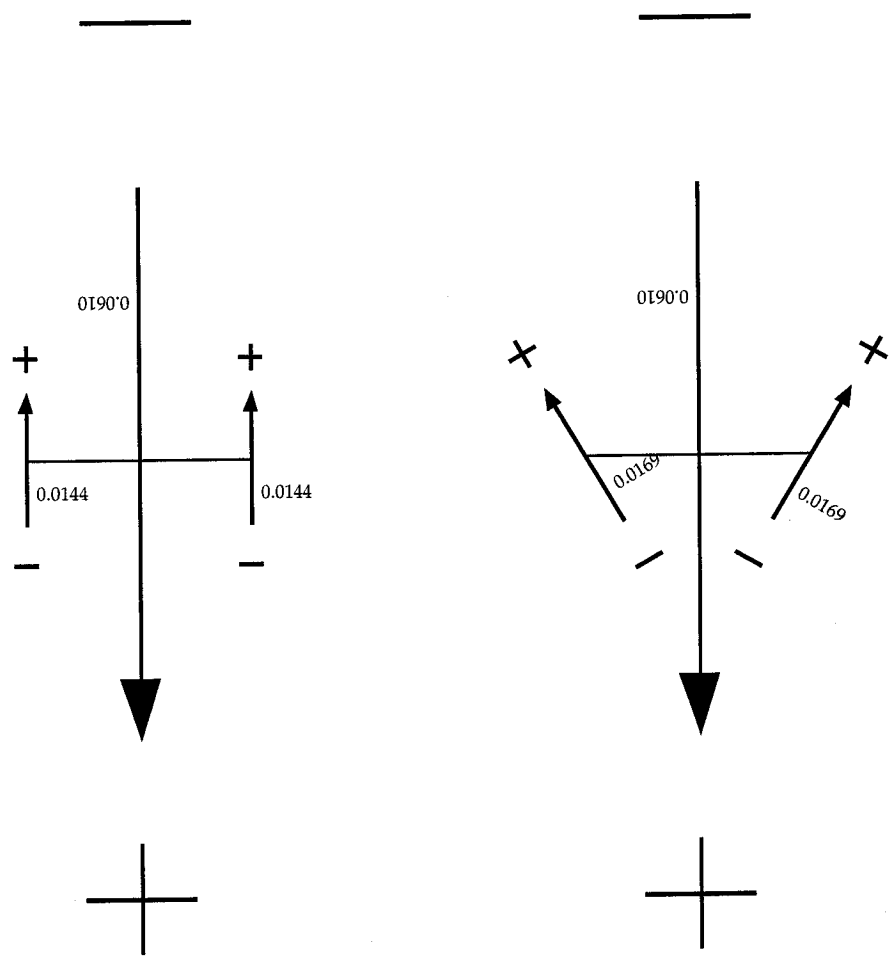

FIGURE 2 Distributed dipoles for C_{60} ph and hh bonds. For clarity, only the dipoles in the plane defined by the bond and the molecule center are shown. The tangential and radial components of the dipole on the carbon center have been combined in the hh bond diagram.

7.7 Discussion

Figure 1 shows the tangential distributed dipoles surrounding pentagonal and hexagonal faces of the C_{60} molecule. A simple explanation serves to rationalize each of the dipoles. The tangential dipoles contribute a small positive charge to the center of the pentagonal face and a slight negative charge to the hh bonds of the hexagonal face. This is qualitatively what is observed.[1] The attraction between pentagonal faces and hh bonds explains the observed low temperature phase of C_{60}. We attribute both of these effects to the π-bonds in C_{60}. In sp^2 hybridized carbon, as in graphite, the p_z orbitals are symmetric about the x-y plane and therefore directed normal to that plane. For C_{60}, the p_r orbital is not completely decoupled from the p_θ and p_ϕ orbitals due to the curvature of the molecular surface. This tends to polarize the p_r orbital such that its electron density is greater outside of the molecule rather than inside. See Fig. 2. Once the bonds are polarized in this way, their overlap can be improved by canting them towards one another pairwise. This canting explains the tangential components of the dipoles.

In Table II we compare the various models based on the statistical variance using the *ab initio* values as the "correct" values.[12] Three of the point charge models did not explicitly fit the molecular multipole moments and, not surprisingly, do not fit them well.[9–11] The final point charge model contains more fitting parameters than there are data.[12] These extra degrees of freedom allow the multipoles to be fit exactly but it is impossible to infer which of the infinite set of such models best represents the molecule. Our current work contains fewer fitting parameters than there are data points. Therefore the fit is imperfect but the values of the fitting parameters can be interpreted physically. The variance is the statistical quantity used to evaluate the quality of a fit to a set of data. By this measure, the distributed multipoles model developed here is by far the best fit to the data. It is also encouraging that the multipole model makes a reasonable estimate (within 25fit set of data. This suggests that the multipole model captures the physics of the actual electronic density distribution.

TABLE II Error Analysis

Source	n_p	n_d	Sum-of-Squares $\sum\left(\frac{q_i-q_i^{ab}}{q_i^{ab}}\right)^2$	Variance $\frac{SS}{n_d-n_p}$	Prediction q_{18}/q_{18}^{ab}
Distributed Multipoles	3	4	0.072	0.072	0.75
LLM Model[9]	0	4	220.1	55.0	$-2.3 * 10^{-5}$
SCK Model[10]	0	4	34.9	8.72	0.22
GG Model[11]	0	4	14.7	3.68	-0.11
YHE Model[12]	10	5	0.0	∞	

The superscript 'ab' refers to the *ab initio* values.[12] The prediction column is a test of the current model's ability to estimate multipoles that were not fit.

Our distributed dipole model contains 60 dipoles on the carbon centers and 90 dipoles on the bond centers. This makes it considerably more complicated than the point charge models.[9–12] This model has the advantage, however, of being having relatively few free parameters which can all be explained in terms of polarization of atomic orbitals. The other models put positive charges in unphysical locations,[9,11,12] do not match calculated molecular multipole moments,[9–11] and/or contain more free parameters than data values.[12] This model could be improved by calculating the distributed multipoles from *ab initio* calculations rather than fitting them, as Stone intended.[13]

7.8 References

[1]W. I. F. David, R. M. Ibberson, T. J. S. Dennis, J. P. Hare, and K. Prassides, Europhys. Lett. **18**, 219 (1992).

[2]K. H. Michel, J. Chem. Phys. **97**, 5155 (1992).

[3]K. H. Michel, J. R. D. Copley, and D. A. Neumann, Phys. Rev. Lett. **68**, 2929 (1992).

[4]K. H. Michel, Z. Phys. B **88**, 71 (1992).

[5]A. B. Harris, Physica A **205**, 154 (1994).

[6]P. Schiebel, K. Wulf, W. Prandl, G. Heger, R. Papoular, and W. Paulus, Acta Cryst. **A52**, 176 (1996).

[7]J. N. Sherwood, (ed.) *The Plastically Crystalline State* (Wiley-Interscience, New York, 1979).

[8]H. M. James and T. A. Keenan, J. Chem. Phys. **31**, 12 (1959).

[9]J. P. Lu, X.-P. Li, and R. M. Martin, Phys. Rev. Lett. **68**, 1551 (1992).

[10]M. Sprik, A. Cheng, and M. L. Klein, J. Phys. Chem. **96**, 2027 (1992).

[11]Y. Guo and W. A. Goddard, unpublished results. In this point charge model, there is +0.142e on the single bonds, −0.106e on the double bonds, and −0.089e on the carbon centers.

[12]T. Yildirim, A. B. Harris, and S. C. Erwin, Phys. Rev. B **48**, 1888 (1993).

[13]A. J. Stone, Chem. Phys. Lett. **83**, 233 (1981).

[14]N. V. Cohan, Proc. Cambridge Phil. Soc. **54**, 28 (1958).

[15]A. G. McLellan, J. Chem. Phys. **34**, 1350 (1961).

[16]J. Reynal, J. Math Phys. **26**, 2441 (1985).

[17]L. Elcoro, J. M. Perez-Mato, and G. Madariaga, Acta Cryst. A **50**, 182 (1994).

[18]W. Prandl, P. Schiebel, and K. Wulf, Acta Cryst. A **52**, 171 (1996).

[19]K. Shirai, J. Phys. Soc. Japan **61**, 2735 (1992). Table III contains several typographical errors, all of which can be found by testing the orthogonality and normality of the basis functions.

[20]S. L. Altmann, *Rotations, Quaternions, and Double Groups* (Clarendon Press, Oxford, 1986) pp. 73-76.

[21]W. I. F. David, R. M. Ibberson, J. C. Matthewman, K. Prassides, T. J. S. Dennis, J. P. Hare, H. W. Kroto, R. Taylor, and D. R. M. Walton, Nature **353**, 147 (1991).

Chapter 8 Concluding Remarks

Nucleation theory has been a rich field of inquiry for over a century and I suspect that it will continue to be for the foreseeable future. If progress in our understanding is to be made, then it will likely be a result of both theory and experiment. In this thesis, I have presented pieces of the foundation needed to extend current nucleation theory to cover experimentally accessible systems. Without this common ground of inquiry, theorists will lack the observations needed to guide their models and experimentalists will lack a framework for understanding and critiquing their results.

It is my contention that the plastically crystalline substances will provide the needed common ground. These molecular systems have high point symmetries, which make them tractable for theorists, and at least some of them have moderate boiling points, which make them accessible to experimentalists. Even so, calculating nucleation rates for these substances from molecular models will take considerable effort. The more desirable physical properties come at the expense of the complexity inherent in their orientational disorder. This thesis, particularly Chapters 6 and 7, is intended to begin to propose the techniques needed to handle this complexity.

Clearly, more work is needed. The hindered rotor partition function for multidimensional rotors will need to be estimated in an efficient manner. Improved methods for estimating the hindering potential in a variety of geometries are needed. Once these problems are addressed, we will be in a position to make predictions of the nucleation rates for these molecular systems and to learn through direct comparison with experiments. This will be a major step toward the day when accurate nucleation rate calculations become routine.

Appendix A Icosahedra

A.1 Properties

Since the icosahedron plays an important role in several chapters of this thesis, this Appendix is included as a reference to some of the properties of the icosahedron and its relationship to a cube. Both the cube and icosahedron are Platonic solids.[1] Platonic solids are three-dimensional figures such that all of the vertices, edges, and faces are equivalent to one another. By equivalent, we mean that a rotation and/or inversion can map the parts of the object onto each other, leaving the solid in an indistinguishable orientation. The five Platonic solids are the tetrahedron, cube, octahedron, dodecahedron, and icosahedron.

We will use the standard orientations as described by David.[2] Consider a cube with vertices at cartesian coordinates $(\pm L, \pm L, \pm L)$. Next, bisect each face parallel to two of its edges such that no two bisectors meet at an edge. There are two ways to do this. Once the first face is bisected, however, the orientations of the other bisectors is fixed. A cube decorated with these bisectors has T_h symmetry.[1] The 24 symmetry elements of the T_h point group are a subgroup of the cubic (O_h) and the icosahedral (I_h) groups. An icosahedron can be inscribed in this cube such that its twelve vertices lie on the bisectors of the faces. This is illustrated in Fig. 1. Since there were two choices as to how to bisect the faces, there is an equivalent, but distinguishable way to inscribe an icosahedron in a cube as illustrated in Fig. 2. The two orientations are related by a rotation of $\pi/2$ radians about any of the $(1, 0, 0)$ axes. Table I gives the coordinates of the vertices for both standard orientations.

TABLE I Coordinates

Orientation	Coordinates
A	$(\pm L,\ \pm L\tau,\ 0)$
	$(0,\ \pm L,\ \pm L\tau)$
	$(\pm L\tau,\ 0,\ \pm L)$
B	$(\pm L,\ 0,\ \pm L\tau)$
	$(\pm L\tau,\ \pm L,\ 0)$
	$(0,\ \pm L\tau,\ \pm L)$

$\tau = (\sqrt{5} - 1)/2$ is the golden mean.

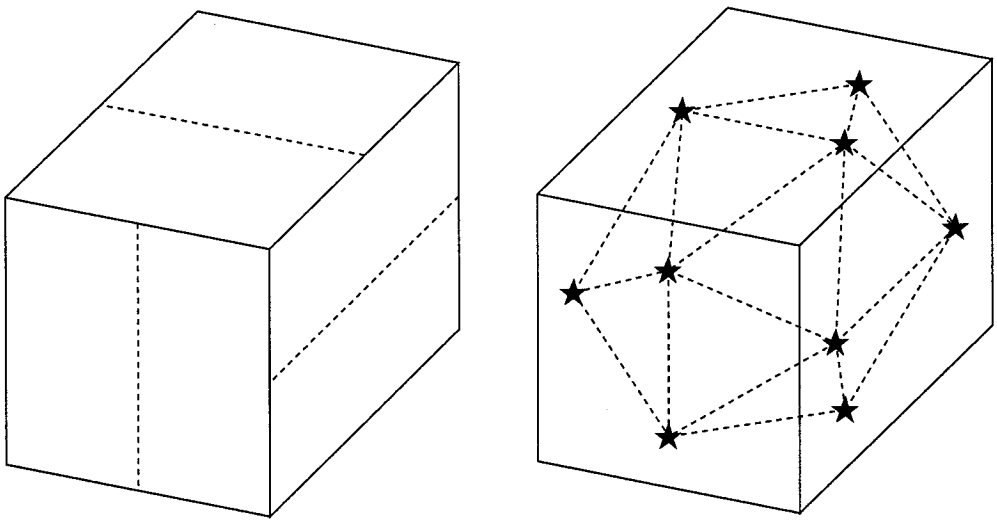

FIGURE 1 Standard Orientation A. An icosahedron can be inscribed in a cube such that its twelve vertices (black stars) lie on the bisectors of the cube faces. The $(1, 1, 1)$ directions are shared 3-fold axes and the $(1, 0, 0)$ directions are shared 2-fold axes.

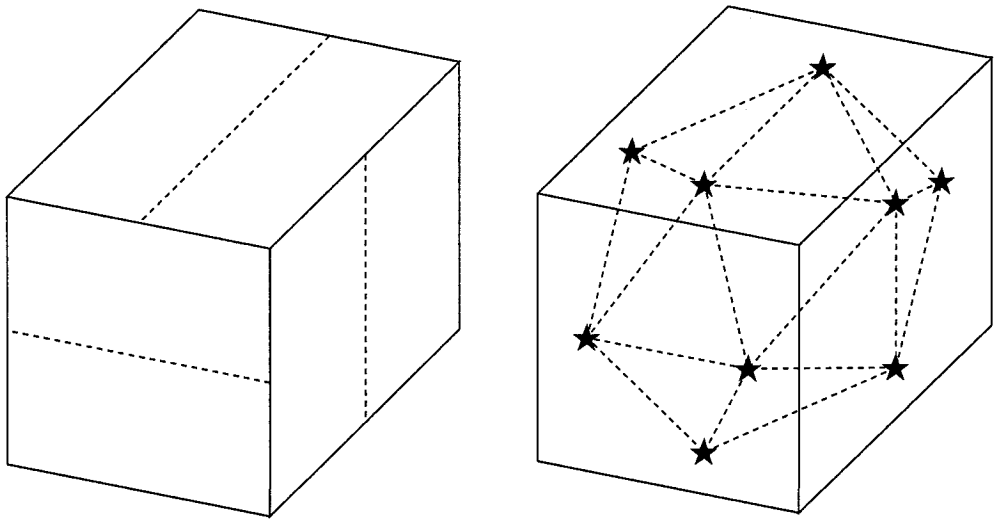

FIGURE 2 Standard Orientation B. Alternative way to inscribe an icosahedron in a cube.

TABLE II Icosahedron Properties

Property	Value
Point Group	I_h
Number of 5-fold (S_{10}) Axes	6
Number of 3-fold (S_6) Axes	15
Number of 2-fold (C_2) Axes	10
Number of Mirror Planes	10
Number of Inversion Centers	1
Number of Vertices	12
Number of Edges	30
Number of Faces	20
Edge Length	$2L\tau$
Total Area	$L^2(30\sqrt{3} - 10\sqrt{15})$
Volume	$L^3 4.1202$

$\tau = (\sqrt{5} - 1)/2$ is the golden mean.

Table II lists some useful properties of the icosahedron. They are simple to derive given the coordinates in Table I and the point group of the icosahedron (I_h).[1]

A.2 References

[1]F. A. Cotton, *Chemical Applications of Group Theory* (Wiley, New York, 1990), pp45-50, 54-56, and 426-436.

[2]W. I. F. David, R. M. Ibberson, J. C. Matthewman, *et al.*, Nature **353**, 147 (1991).

Appendix B Mackay Icosahedra

B.1 Properties

The Mackay icosahedra are collections of spheres arranged in icosahedral shells. Due to the symmetry of the underlying icosahedron, it is sufficient to specify the locations of the spheres in a given face. Figure 1 shows the lattice points for the first four Mackay icosahedra relative to a representative face.

The number of spheres in a Mackay icosahedron with N shells can be determined by summing over the number of spheres (n) in each of the shells. The central sphere is a special case.

$$n_0 = 1 \tag{1}$$

The N^{th} shell has spheres located at the twelve vertices, along the thirty edges, and in the twenty faces. As shown in Fig. 1, in each representative face, the spheres are arranged in a hexagonal lattice with $N+1$ sites from point to point along one edge. It follows directly that there is one sphere at each vertex and $N-1$ spheres along the edges. The number of spheres in the faces can be calculated using the well-known formula for the sum of consecutive integers,[2]

$$\sum_{i=1}^{N} i = N(N+1)/2. \tag{2}$$

Using these relationships leads to the following relationship for the number of spheres in the i^{th} shell of a Mackay icosahedron:

$$n_i = 12 + 30(i-1) + 20(i-1)(i-2)/2 = 10i^2 + 2. \tag{3}$$

Summing the contributions from the first N shells gives the number of spheres in the N^{th} Mackay icosahedron.

$$n = \sum_{i=0}^{N} n_i \tag{4}$$

Again, the requisite sums are tabulated.[2] Substituting algebraic relationships for the summations gives

$$n = (10N^3 + 15N^2 + 11N + 3)/3. \tag{5}$$

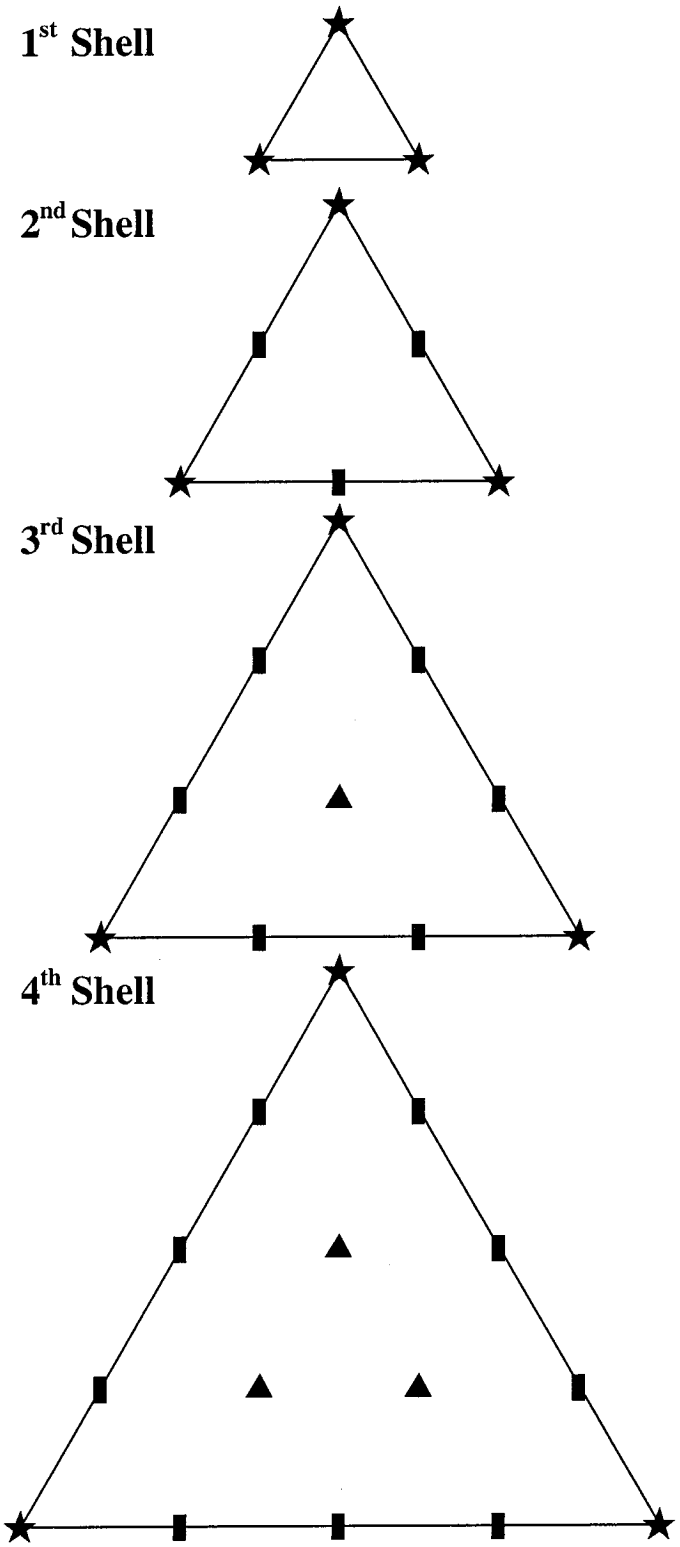

FIGURE 1 Representative faces for the first four Mackay icosahedra. Spheres at vertices (stars) are shared among five faces, spheres along edges (rectangles) are shared between two faces, and spheres in the faces (triangles) are unshared.

TABLE I Enumeration of Spheres in a Mackay Icosahedron

Group	Subgroup	Spheres
Shell 0	Center	1
Shell N	Each Vertex	1
	Each Edge	$N-1$
	Each Face	$(N-1)(N-2)/2$
	Total	$10N^2+2$
Shells 0,1,...,N	Total	$(10N^3+15N^2+11N+3)/3$

This relationship was originally given by Mackay.[1]

It is occasionally useful to calculate the number of shells (N) needed to construct a Mackay icosahedron with n spheres. This can be calculated by inverting Eq. 5 using standard techniques for cubic equations.[3]

$$N = \sqrt[3]{\frac{3n}{20}}\left[\sqrt[3]{1+\sqrt{1+\frac{343}{4860n^2}}} - \sqrt[3]{-1+\sqrt{1+\frac{343}{4860n^2}}}\right] - \frac{1}{2} \tag{6}$$

The following asymptotic approximation to Eq. 6 is quite accurate for $n \geq 13$ and is much easier to use.

$$N = \sqrt[3]{\frac{3n}{10}} - \frac{1}{2} + O(1/n^{1/3}) \tag{7}$$

B.2 References

[1]A. L. Mackay, Acta Cryst. **15**, 916 (1962).

[2]I. S. Gradshteyn and I. M. Ryzhik, *Tables of Integrals, Series, and Products, 5th ed.* (Academic Press, San Diego, 1994), p2.

[3]S. I. Heisler, *The Wiley Engineer's Desk Reference* (Wiley, New York, 1984) pp4-5.

Appendix C Code to Produce Mackay Icosahedral Structures

C.1 Description

The following FORTRAN code produces BIOGRAF[1] format input files for arbitrarily large Mackay icosahedral clusters of argon atoms. The clusters produced are near a local minimum, but a few iterations with a congugate-gradient or similar minimization routine are needed to locate the local minimum structure under a given interaction potential. These are the structures used in Chapter 3.

C.2 References

[1]BIOGRAF is a trademark of Molecular Simulations Inc. (Burlington, Mass).

C.3 Code

```
      PROGRAM MAC
C
C This program produces BIOGRAF-format input files for Mackay
C icosahedral clusters of argon atoms.
C
      INTEGER NSHELL,CNT,CNT2
      REAL B, Y(3,0:11), N, PI, De
      COMMON /EF/ E(3,100), F(3,5000)

C Write coordinates of atoms.
      OPEN (11, FILE = 'TRIPLETS.DAT')
      WRITE (11, *) 0.0, 0.0, 0.0
      PRINT *, 'Enter the number of Mackay icosahedrons to consider.'
      READ *, NSHELL
      PRINT *, 'Enter the characteristic distance in Angstoms.'
      READ *, De
```

```
      CNT = 1.
      B = ACOS(1./(5.0**0.5))
      PI = ACOS(-1.0)
      SA = SIN(B)
      CA = COS(B)
      B = 2.*PI/5.
      DO 10, N = 1,NSHELL
C Vertices
           Y(1,0) = 0.0
           Y(2,0) = 0.0
           Y(3,0) = N
           DO 3, R = 1.,5.
                Y(1,R) = N*SA*COS(R*B)
                Y(2,R) = N*SA*SIN(R*B)
                Y(3,R) = N*CA
3          CONTINUE
           DO 4, I = 6.,10.
                Y(1,I) = -Y(1,I-5)
                Y(2,I) = -Y(2,I-5)
                Y(3,I) = -Y(3,I-5)
4          CONTINUE
           Y(1,11) = 0.0
           Y(2,11) = 0.0
           Y(3,11) = -Y(3,0)
C Edges
           DO 6, J = 1,15
                IF (J.EQ.1) THEN
                     CALL NSECT( Y(1,0),Y(2,0),Y(3,0) ,
     +                           Y(1,1),Y(2,1),Y(3,1) , N )
                ELSE IF (J.EQ.2) THEN
```

```
            CALL NSECT( Y(1,0),Y(2,0),Y(3,0) ,
     +                  Y(1,2),Y(2,2),Y(3,2) , N )
          ELSE IF (J.EQ.3) THEN
            CALL NSECT( Y(1,0),Y(2,0),Y(3,0) ,
     +                  Y(1,3),Y(2,3),Y(3,3) , N )
          ELSE IF (J.EQ.4) THEN
            CALL NSECT( Y(1,0),Y(2,0),Y(3,0) ,
     +                  Y(1,4),Y(2,4),Y(3,4) , N )
          ELSE IF (J.EQ.5) THEN
            CALL NSECT( Y(1,0),Y(2,0),Y(3,0) ,
     +                  Y(1,5),Y(2,5),Y(3,5) , N )
          ELSE IF (J.EQ.6) THEN
            CALL NSECT( Y(1,1),Y(2,1),Y(3,1) ,
     +                  Y(1,2),Y(2,2),Y(3,2) , N )
          ELSE IF (J.EQ.7) THEN
            CALL NSECT( Y(1,2),Y(2,2),Y(3,2) ,
     +                  Y(1,3),Y(2,3),Y(3,3) , N )
          ELSE IF (J.EQ.8) THEN
            CALL NSECT( Y(1,3),Y(2,3),Y(3,3) ,
     +                  Y(1,4),Y(2,4),Y(3,4) , N )
          ELSE IF (J.EQ.9) THEN
            CALL NSECT( Y(1,4),Y(2,4),Y(3,4) ,
     +                  Y(1,5),Y(2,5),Y(3,5) , N )
          ELSE IF (J.EQ.10) THEN
            CALL NSECT( Y(1,5),Y(2,5),Y(3,5) ,
     +                  Y(1,1),Y(2,1),Y(3,1) , N )
          ELSE IF (J.EQ.11) THEN
            CALL NSECT( Y(1,1),Y(2,1),Y(3,1) ,
     +                  Y(1,9),Y(2,9),Y(3,9) , N )
          ELSE IF (J.EQ.12) THEN
```

```
                CALL NSECT( Y(1,9),Y(2,9),Y(3,9) ,
     +                      Y(1,2),Y(2,2),Y(3,2) , N )
            ELSE IF (J.EQ.13) THEN
                CALL NSECT( Y(1,2),Y(2,2),Y(3,2) ,
     +                      Y(1,10),Y(2,10),Y(3,10) , N )
            ELSE IF (J.EQ.14) THEN
                CALL NSECT( Y(1,10),Y(2,10),Y(3,10) ,
     +                      Y(1,3),Y(2,3),Y(3,3) , N )
            ELSE IF (J.EQ.15) THEN
                CALL NSECT( Y(1,3),Y(2,3),Y(3,3) ,
     +                      Y(1,6),Y(2,6),Y(3,6) , N )
            END IF
            DO 5, I = 1.,N-0.5
                CNT = CNT + 2
                WRITE (11,*) E(1,I), E(2,I), E(3,I)
                WRITE (11,*) -E(1,I), -E(2,I), -E(3,I)
5           CONTINUE
6       CONTINUE
C Faces
        DO 8, J = 1,10
            IF (J.EQ.1) THEN
                CALL FACE( Y(1,0),Y(2,0),Y(3,0) ,
     +                     Y(1,1),Y(2,1),Y(3,1) ,
     +                     Y(1,2),Y(2,2),Y(3,2) , N , CNT2)
            ELSE IF (J.EQ.2) THEN
                CALL FACE( Y(1,0),Y(2,0),Y(3,0) ,
     +                     Y(1,2),Y(2,2),Y(3,2) ,
     +                     Y(1,3),Y(2,3),Y(3,3) , N , CNT2)
            ELSE IF (J.EQ.3) THEN
                CALL FACE( Y(1,0),Y(2,0),Y(3,0) ,
```

```
+                    Y(1,3),Y(2,3),Y(3,3) ,
+                    Y(1,4),Y(2,4),Y(3,4) , N , CNT2)
          ELSE IF (J.EQ.4) THEN
               CALL FACE( Y(1,0),Y(2,0),Y(3,0) ,
+                    Y(1,4),Y(2,4),Y(3,4) ,
+                    Y(1,5),Y(2,5),Y(3,5) , N , CNT2)
          ELSE IF (J.EQ.5) THEN
               CALL FACE( Y(1,0),Y(2,0),Y(3,0) ,
+                    Y(1,5),Y(2,5),Y(3,5) ,
+                    Y(1,1),Y(2,1),Y(3,1) , N , CNT2)
          ELSE IF (J.EQ.6) THEN
               CALL FACE( Y(1,1),Y(2,1),Y(3,1) ,
+                    Y(1,9),Y(2,9),Y(3,9) ,
+                    Y(1,2),Y(2,2),Y(3,2) , N , CNT2)
          ELSE IF (J.EQ.7) THEN
               CALL FACE( Y(1,2),Y(2,2),Y(3,2) ,
+                    Y(1,10),Y(2,10),Y(3,10) ,
+                    Y(1,3),Y(2,3),Y(3,3) , N , CNT2)
          ELSE IF (J.EQ.8) THEN
               CALL FACE( Y(1,3),Y(2,3),Y(3,3) ,
+                    Y(1,6),Y(2,6),Y(3,6) ,
+                    Y(1,4),Y(2,4),Y(3,4) , N , CNT2)
          ELSE IF (J.EQ.9) THEN
               CALL FACE( Y(1,4),Y(2,4),Y(3,4) ,
+                    Y(1,7),Y(2,7),Y(3,7) ,
+                    Y(1,5),Y(2,5),Y(3,5) , N , CNT2)
          ELSE IF (J.EQ.10) THEN
               CALL FACE( Y(1,5),Y(2,5),Y(3,5) ,
+                    Y(1,8),Y(2,8),Y(3,8) ,
+                    Y(1,1),Y(2,1),Y(3,1) , N , CNT2)
```

```
                END IF

                DO 7, I = 1, CNT2
                     CNT = CNT + 2
                     WRITE (11,*) F(1,I), F(2,I), F(3,I)
                     WRITE (11,*) -F(1,I), -F(2,I), -F(3,I)
7               CONTINUE
8          CONTINUE
C Vertices
           DO 9, I = 0,11
                CNT = CNT + 1
                WRITE (11,*) Y(1,I), Y(2,I), Y(3,I)
9          CONTINUE
10    CONTINUE
      CLOSE (11)

C Write BIOGRAF file.
      DO 14, I = 1, CNT
           NM = 1
           DO 13, J = 1, NSHELL
                NM = NM + J**2*10+2
                IF (I.EQ.NM) THEN
                     CALL Ecl(I,J,De)
                END IF
13         CONTINUE
14    CONTINUE

      END
**********************
      SUBROUTINE Ecl(I,N,De)
```

```
      CHARACTER*8 NAME
      CHARACTER*5 NC
      REAL X1, X2, X3

      NAME = 'MAC' // NC(N)
      PRINT *, 'Writing Biograf file for ',NAME
      PRINT *, '     (n =',I,' atoms)'
      OPEN (16, FILE = 'TRIPLETS.DAT')
      OPEN (18, FILE = NAME)
      WRITE (18,2)
      WRITE (18,3)
      WRITE (18,4) NC(N)
      WRITE (18,5)
      WRITE (18,6)
      WRITE (18,7)
      WRITE (18,8)
      DO 1, J = 1, I
           READ (16,*) X1, X2, X3
           WRITE (18,9) J, De*X1, De*X2, De*X3
1     CONTINUE
      WRITE (18,10)
      WRITE (18,11)

      CLOSE (16)
      CLOSE (18)

2     FORMAT ('BIOGRF  325')
3     FORMAT ('DESCRP Cluster')
4     FORMAT ('REMARK of ', A5, 'shells of argon atoms')
5     FORMAT ('REMARK arranged in a Mackay icosahedron')
```

```
6     FORMAT ('REMARK Created by rbm @ home.')
7     FORMAT ('FORCEFIELD DREIDING')
8     FORMAT ('FORMAT ATOM   ',
     +'(a6,1x,i5,1x,a5,1x,a3,1x,a1,1x,a5,3f10.5,',
     +'1x,a5,i3,i2,1x,f8.5,i2,i4,f10.5)')
9     FORMAT ('HETATM', I6, ' Ar    ORG A    1 ', 3F10.5,
     +        ' Ar     4 0  0.00000 0   0')
10    FORMAT ('FORMAT CONECT (a6,14i6)')
11    FORMAT ('END')
      END
**********************
      FUNCTION NC(I)
      CHARACTER*5 NC
      INTEGER I, J, K, N, D(5), E

      K = I
      N = LOG10(I)
      DO 1, J = 0,N
           E = 10**(N-J)
           D(J+1) = K / E
           K = K - D(J+1)*E
1     CONTINUE
      DO 2, J = N+2,5
           D(J) = 32-48
2     CONTINUE
      NC = CHAR(D(1)+48) // CHAR(D(2)+48) //
     +     CHAR(D(3)+48) // CHAR(D(4)+48) // CHAR(D(5)+48)

      END
**********************
```

```
      SUBROUTINE NSECT( X1, Y1, Z1, X2, Y2, Z2, N )
      REAL X1, Y1, Z1, X2, Y2, Z2, N, R, E
      COMMON /EF/ E(3,100), F(3,5000)

      DO 1, R = 1, N-1
           E(1,R) = R/N*X1 + (N-R)/N*X2
           E(2,R) = R/N*Y1 + (N-R)/N*Y2
           E(3,R) = R/N*Z1 + (N-R)/N*Z2
1     CONTINUE

      END
**********************
      SUBROUTINE FACE ( X1, Y1, Z1, X2, Y2, Z2, X3, Y3, Z3, N, CNT2)
      INTEGER CNT2
      REAL X1, Y1, Z1, X2, Y2, Z2, X3, Y3, Z3, N, F, A, B, C
      COMMON /EF/ E(3,100), F(3,5000)

      CNT2 = 0
      IF (N.LT.3) GOTO 3
      DO 2, A = 1,N-2
           DO 1, B = 1,N-1-A
                C = N-A-B
                IF (C.GT.0) THEN
                     CNT2 = CNT2 + 1
                     F(1,CNT2) = ( A*X1 + B*X2 + C*X3 ) / N
                     F(2,CNT2) = ( A*Y1 + B*Y2 + C*Y3 ) / N
                     F(3,CNT2) = ( A*Z1 + B*Z2 + C*Z3 ) / N
                END IF
1          CONTINUE
2     CONTINUE
```

```
3       CONTINUE

        END
```